Analysis Note

Measurement of charged particle production in diffractive proton-proton collisions at $\sqrt{s} = 200$ GeV with tagging of the forward scattered proton

Leszek Adamczyk[1], Łukasz Fulek[1], Włodek Guryn[2], Bogdan Pawlik[3], Mariusz Przybycień[1], and Rafał Sikora[1]

[1] *AGH University of Science and Technology, FPACS, Kraków, Poland*
[2] *Brookhaven National Laboratory, Upton, NY, USA*
[3] *Institute of Nuclear Physics PAN, Kraków, Poland*

4th January 2020

In this note we present the analysis of the Single Diffractive Dissociation process with the STAR Roman Pot detectors at RHIC. The measurement is focused on the charged particle multiplicity, its dependence on the transverse momentum and pseudorapidity in three regions of ξ: $0.02 < \xi < 0.05$, $0.05 < \xi < 0.1$ and $0.1 < \xi < 02$. The identified particle to antiparticle (pion, kaon, proton and their antiparticle) multiplicity ratios as a function of transverse momentum in above three ξ regions are also measured. The data come from proton-proton collisions collected in 2015. The forward proton was tagged in the STAR Roman Pot system while the charged particle tracks were reconstructed in the STAR Time Projection Chamber (TPC). We describe all stages of the analysis involving comparison of the data with MC simulations and systematic uncertainty studies. More technical parts of the analysis are described in a supplementary analysis note [1].

List of contributions

Leszek Adamczyk	Analysis coordination/supervision, production of picoDST, production of embedded MC samples
Łukasz Fulek*	Main analyzer, write-up author
Mariusz Przybycień	Analysis supervision
Rafał Sikora	Analysis support

* - contact editor

Change log

30 May 2019	ver. 1.0	Initial revision

Contents

1. Introduction

Inclusive measurements of charged-particle distributions in proton–proton (*pp*) collisions probe the strong interaction in the low-momentum transfer, non-perturbative regime of Quantum Chromodynamics (QCD). In this kinematic region interactions are usually described by phenomenological models implemented in Monte Carlo (MC) event generators. Measurements can be used to constrain the free parameters of these models. An accurate description of low-energy strong interaction processes is essential for understanding and precise simulation of different types of *pp* processes and the effects of multiple *pp* collisions in the same bunch crossing at high instantaneous luminosity at hadron colliders. Measurements with tagging of the forward-scattered proton are of special interest. They give direct access to specific but still significant part of *pp* processes called diffraction. In addition precise modelling of forward particle production is essential for better understanding of the longitudinal development of air showers observed in experiments studying cosmic radiation.

We present a measurement of charged particle production in Single Diffractive Dissociation (SD: $p + p \rightarrow p + \mathrm{X}$). The following observables are studied:

$$\frac{1}{N_{\mathrm{ev}}}\frac{dN_{\mathrm{ev}}}{dn_{\mathrm{ch}}}, \qquad \frac{1}{N_{\mathrm{ev}}}\frac{1}{2\pi p_{\mathrm{T}}}\frac{d^2N}{d\bar{\eta}dp_{\mathrm{T}}}, \qquad \frac{1}{N_{\mathrm{ev}}}\frac{dN}{d\bar{\eta}} \tag{1.1}$$

where n_{ch} is the number of primary charged particles within kinematic range given by $p_{\mathrm{T}} >$ 200 MeV and $|\eta| < 0.7$, N_{ev} is the total number of events with $2 \leq n_{\mathrm{ch}} \leq 8$, N is the total number of charged particles within the above kinematic acceptance and $\bar{\eta}$ is the pseudorapidity of the charged particle with longitudinal momentum taken with respect to direction of the forward scattered proton. To suppress non-SD events the trigger system required no signal in BBC-small in the direction of forward scattered proton and signal in BBC-small in opposite direction. The measurements are performed in a fiducial phase space of the forward scattered protons of $0.04 < -t < 0.16$ GeV^2/c^2 and $0.02 < \xi < 0.2$, where ξ is the fractional energy loss of the scattered proton. In case of SD process $\xi = M_{\mathrm{X}}^2/s$, where M_{X} is the mass of the state X into which one of the incoming proton dissociates and s is the center of mass energy squared of the *pp* system. The above mentioned observables are presented in three ξ regions: $0.02 < \xi < 0.05$, $0.05 < \xi < 0.1$ and $0.1 < \xi < 0.2$. In addition their average values in an event are presented as a function of ξ.

We have also studied an identified particle to antiparticle (pion, kaon, proton and their antiparticle) multiplicity ratios as a function of p_{T} also in the above mentioned three regions of ξ. The system X into which proton diffractively dissociates has net charge and baryon number +1. It is believed that initial charge and barion number should appear in the very forward direction leading to the equal amount of particles and antiparticles in the central region created by fragmentation and hadronization processes. However other scenarios are also possible where extra baryon is uniformly distributed over rapidity [2] or even appear close to the gap edge [3]. It is natural to expect that possible charge and baryon number transfer to central region will be better visible at small ξ where amount of particle-antiparticle creation is smaller due to the generally smaller particle multiplicity or due to the fact that gap edge is inside our fiducial region of $|\eta| < 0.7$.

2. Monte Carlo Samples

MC samples used to correct data for detector effects were obtained by the embedding MC technique [4], in which simulated particles are mixed with the real Zerobias events at the raw data level. Zerobias data events used in the embedding were sampled over the entire data-taking period in order to properly describe the data set used in the analysis. Two samples of embedding MC were produced:

1. Single particle MC, in which particles are generated from flat distributions in η and p_{T}, in order to have similar statistics in all bins.

2. The Schuler and Sjöstrand (SaS) model implemented in PYTHIA8 with 4C tune.

The particles were propagated through the full simulation of the STAR-TPC and RP system detectors using GEANT3 [5] and GEANT4 [6], respectively. Obtained information for the simulated particles was embedded into the existing information of the real data. These events were next processed through the full reconstruction chain.

It is preferred to get the detector corrections from a MC, which is dedicated to simulate the studied physics process. However, for this purpose, the statistics in the MC should be several times greater than we have in the data for analysis. Since this is not possible with low efficiency of TPC and TOF, the basic method of corrections used in the analysis is a method of factorization of global efficiency into the product of single-particle efficiencies. In this way, statistically precise multidimensional corrections on TPC and TOF are obtained from the single particle MC.

Additionally, several pure MC samples were generated. The simulated particles were propagated through full simulation and reconstruction chain but were not embedded into Zerobias events. Systematic effect related to hadronization of the diffractive system was determined by using an alternative hadronization model implemented in HERWIG. The comparison to the corrected data distribution was done for PYTHIA 8 4C (SaS) and HERWIG, in addition all results were compared to the EPOS and alternative PYTHIA 8 model Minimum Bias Rockefeller (MBR) with A2 tune. EPOS predicts very large contribution of forward protons, which originate from non-diffractive events and are well separated in rapidity from other final state particles. This is the result of low mass excitation of the proton remnant ($<$ 1 GeV) leading to hadronization of the beam remnant back to the proton. Therefore for the comparison with uncorrected data EPOS predictions were separated in two classes: diffractive (EPOS-SD) modelled by Pomeron exchange and non-diffractive modelled by low mass excitation of the proton remnant (EPOS-SD$'$). In all PYTHIA 8 models diffractive cross sections are arbitrary suppressed at relatively large values of ξ ($>$0.05). This arbitrary suppression significantly changes predicted distribution of ξ and fractions of different processes in our fiducial phase space. Therefore data was also compared with expectations obtained without suppression of the diffractive cross sections (MBR-tuned).

3. Data Sample and Signal Selection

The data sample used in this analysis was collected in proton-proton collisions at centre-of-mass energy of $\sqrt{s} = 200$ GeV during RHIC Run 15, i.e. in year 2015.

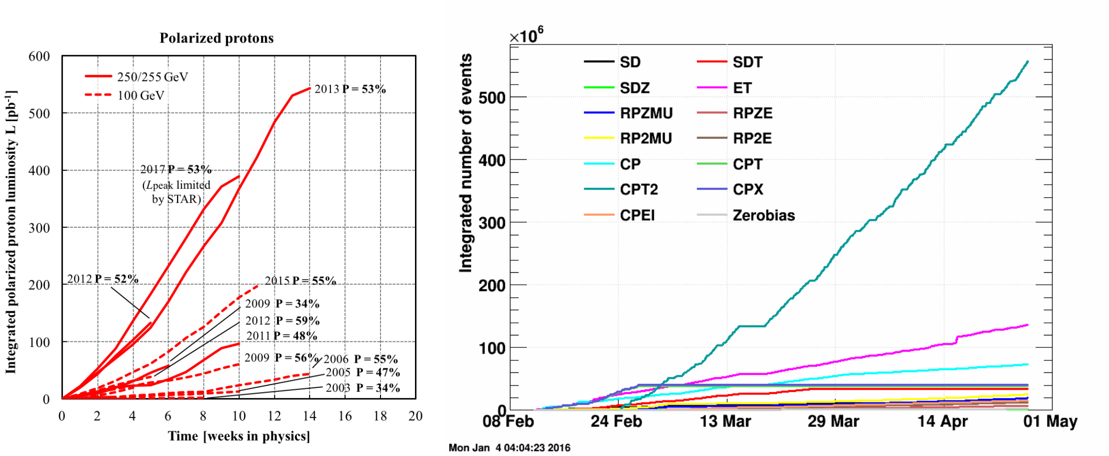

Figure 3.1: (left) Integrated lumonosity delivered by the collider over the seventeen years of operation of RHIC [7]. Dashed lines are for 100 GeV/c proton momentum mailnly for transverse spin physics programs, while continuous lines are for 250/255 GeV/c proton beams aimed predominantly at the W-physics program. The percentage polarization reached in each run is indicated next to the curves. (right) Integrated number of events collected for each trigger in the RP data stream during Run 15.

All of the studies in this work use data from only the SDT trigger condition, which was the main trigger designed for SDD studies in Run 15 and used in this analysis. It was formed by the following conditions combined with the logical AND:

1. RP_EOR || RP_WOR - signal in at least one RP on one side of the STAR central detector.
2. Veto on any signal in small BBC tiles or ZDC on the triggered RP side of the STAR central detector.
3. At least two TOF hits.

Above requirements were imposed in accordance with the diffractive events topology. Veto on any signal in small BBC tiles and ZDC allows to accept only events with rapidity gap and reject diffractive events with parallel pile-up event. The requirement of at least two TOF hits was to ensure activity in the mid-rapidity.

Integrated luminosity delivered by the RHIC to the STAR detector in pp collisions during Run 15 amounts to 185.1 pb^{-1} [7], shown in Fig. 3.1, whereas about 34.4M SDT events were gathered by the STAR detector, which corresponds to 16 nb^{-1} of integrated luminosity.

3.1 Event Selection

Events were selected from those passing the SDT trigger condition. In order to remove events having poor quality the following conditions were required:

1. Signals in exactly two stations of one arm of RP system,
2. Any signal in small BBC tiles or ZDC on the opposite side of the STAR central detector to the triggered RP station,
3. Exactly one proton track in the above RP stations with $0.02 < \xi < 0.2$ and $0.04 < -t < 0.16$ GeV^2/c^2.
4. Exactly one primary vertex with TPC tracks matched with hits in TOF (later in the text such vertex is refered as a TOF vertex),
5. TPC vertex within $|V_z| < 80$ cm - events with vertices away from the IP have low acceptance for the central and forward tracks,
6. At least two but no more than eight primary TPC tracks, $2 \le n_{\rm sel} \le 8$, matched with hits in TOF and satisfying the selection criteria described in Sec. 3.2,
7. If there are exactly two primary tracks satisfying above criteria and exactly two global tracks used in vertex reconstruction (Sec. 5.1), the longitudinal distance between these global tracks should be smaller than 2 cm, $|\Delta z_0| < 2$ cm.

Figure 3.2 shows the multiplicity of TOF vertices (left) and the z-position of primary vertex in a single TOF vertex events (right).

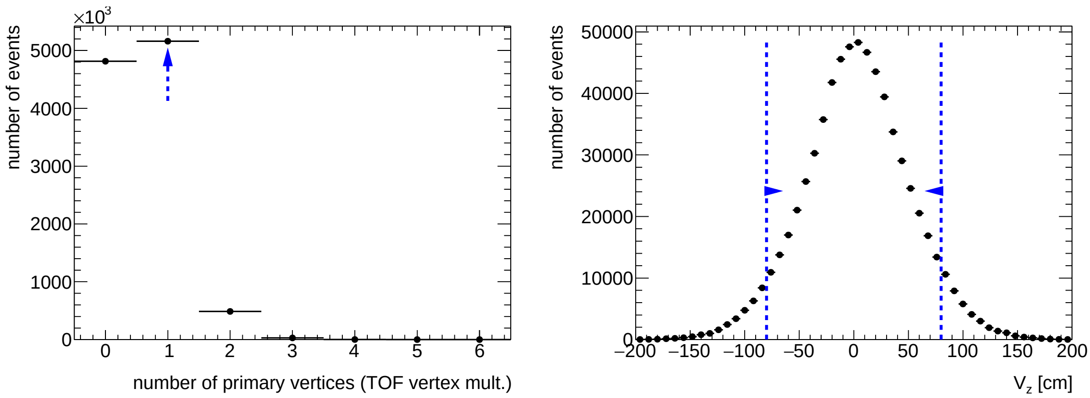

Figure 3.2: (left) Primary vertex multiplicity and (right) the z-position of primary vertex in a single TOF vertex events before applying the cut on the quantity shown. Blue lines indicate regions accepted in the analysis.

3.2 Track Selection

The following quality cuts had to be passed by the selected primary tracks in this analysis:

1. The tracks must be matched with hits reconstructed in TOF,
2. The number of the TPC hits used in the helix fit $N^{\rm fit}_{\rm hits}$ must be greater than 24,
3. The number of the TPC hits used to determine the dE/dx information $N^{\rm dE/dx}_{\rm hits}$ must be greater than 14,
4. The transverse impact parameter with respect to the beamline d_0 must be less than 1.5 cm,
5. The radial component of the distance of the closest approach between the global helix and the vertex DCA$_{xy}$ must be less than 1.5 cm (consistent with the d_0 limit),

6. The absolute magnitude of longitudinal component of the distance of the closest approach between the global helix and the vertex $|\mathrm{DCA}_z|$ must be less than 1 cm,

7. The track's transverse momentum p_{T} must be greater than 0.2 GeV/c,

8. The track's absolute value of pseudorapidity $|\eta|$ must be smaller than 0.7.

The $N_{\mathrm{hits}}^{\mathrm{fit}}$ cut is used to reject low quality TPC tracks and avoid track splitting effects. The d_0 and global DCA_{xy}, $|\mathrm{DCA}_z|$ cuts are used to select tracks that originate from the primary interaction vertex. The cut on $N_{\mathrm{hits}}^{\mathrm{dE/dx}}$ is used to ensure that selected tracks have sufficient energy loss information for particle identification purposes. In this analysis tracks without identification are required to have $p_{\mathrm{T}} > 0.2$ GeV/c and $|\eta| < 0.7$ due to high track reconstruction and TOF matching efficiencies in this region. For the identified particle-antiparticle ratio analysis, where in addition to charged pions, charged kaons and (anti)proton are measured, the p_T cut was increased

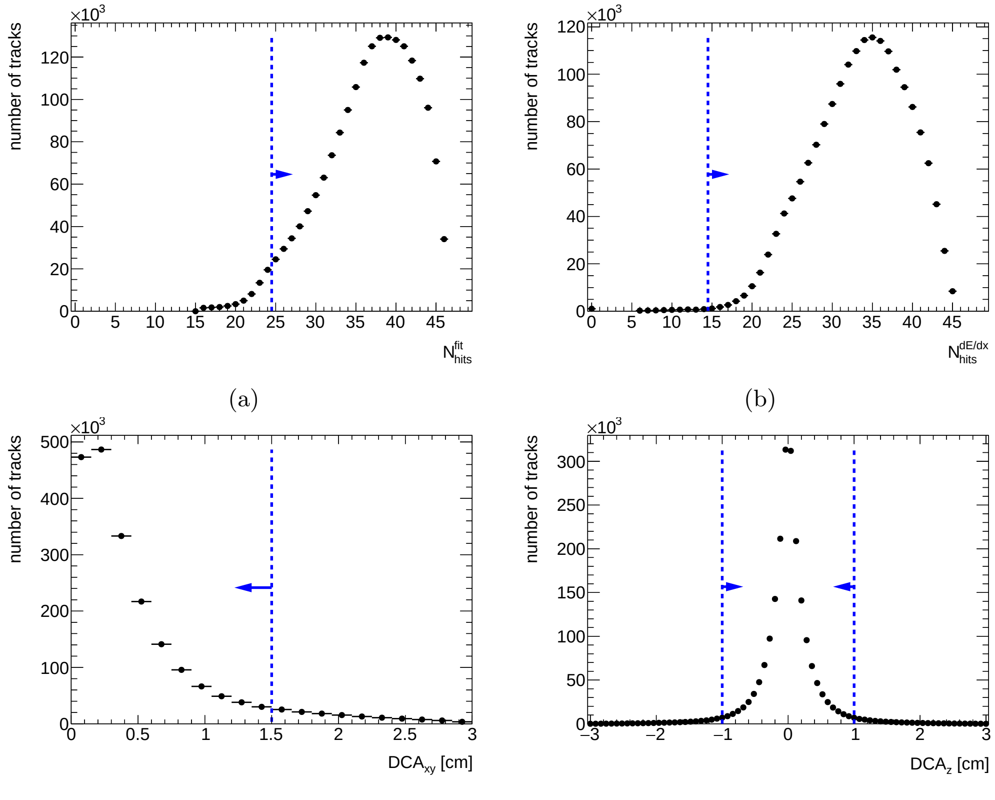

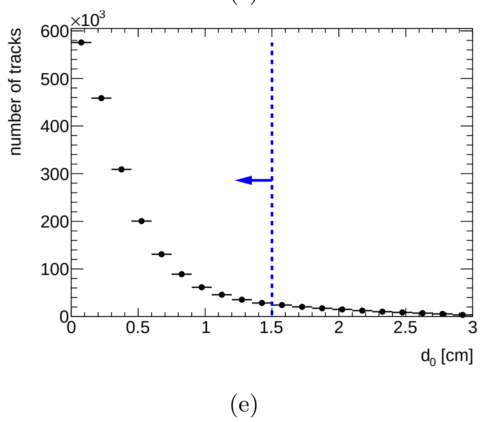

Figure 3.3: Number of the TPC hits used in the helix fit (a) and number of the TPC hits used to determine the dE/dx (b), the radial component (c) and the absolute magnitude of the longitudinal component (d) of the distance of the closest approach between the global helix and the vertex, transverse impact parameter w.r.t. beam-line (e). All distributions are shown before applying the corresponding cuts. Blue lines indicate regions accepted in the analysis.

to 0.3 and 0.4 GeV/c, respectively. The distributions of the DCA_{xy}, $|\mathrm{DCA}_z|$, d_0, $N_{\mathrm{hits}}^{\mathrm{fit}}$ and $N_{\mathrm{hits}}^{\mathrm{dE/dx}}$ quatities together with applied cuts are shown in Fig. 3.3.

3.3 Fiducial Region of the Measurement

A fiducial phase space of measurement is defined by the above selection criteria. Primary charged particles are defined as charged particles with a mean lifetime $\tau > 300$ ps, either directly produced in *pp* interaction or from subsequent decays of directly produced particles with $\tau < 30$ ps. In this analysis the total number of primary charged particles (without identification), n_{ch}, was required to be $2 \leq n_{\mathrm{ch}} \leq 8$. These primary charged particles had to be contained within the kinematic range of $p_{\mathrm{T}} > 0.2$ GeV/c and $|\eta| < 0.7$. In identified charged antiparticle to particle ratio measurement, the lower transverse momentum limit was changed for the analyzed particles as follows: 0.2 GeV/c (pions), 0.3 GeV/c (kaons), 0.4 GeV/c (protons and antiprotons)

The measurements were performed in a fiducial phase space of the forward scattered protons of $0.04 < -t < 0.16$ GeV^2/c^2 and $0.02 < \xi < 0.2$. All measured observables are presented in three ξ regions: $0.02 < \xi < 0.05$, $0.05 < \xi < 0.1$ and $0.1 < \xi < 0.2$.

4. Background Contribution

The total background contribution to the charged-particle distributions can be broken down into event-level and track-level backgrounds, which are described in detail in the following sections:

- Accidental background refers to events which do not originate from a single collision of two protons.
- Non-SD background comprise contibution of non-SD events which originate from a single *pp* collision.
- Track backgrounds from non-primary tracks consist of secondary tracks and fake tracks; the first come mostly from decays, the short-lived particles with mean life $30 < \tau < 300$ ps, or secondary interactions with the detector dead material, while the second comes from the track reconstruction algorithms and out-of-time pile-up with no corresponding true particles.

4.1 Accidental Background

The accidental backgrounds (same bunch pile-up background) are quantified using data-driven method and defined as a process where in one proton-proton bunch crossing there is coincidence of two interactions, where any single-side proton signal is collected in coincidence with a diffractive like signal in the TPC-TOF detector. This has the same signature as a signal process but would not come from a DD, a CD or a ND interaction. This type of background may come from the overlap of a signal in RP (proton from beamhalo, low mass SD process without activity in TOF, elastic or low mass CD processes with undetected proton on the other side) with a Single Diffraction (SD)-like signal in TPC+TOF (ND events without forward proton, which is a dominant contribution, beam-gas or beam-halo, which should be effectively reduced by the requirement of the reconstructed vertex).

The accidental background contribution was calculated analytically from Zerobias data, where two signatures of such background were investigated: the reconstructed proton in RP and the reconstruction of vertex in TPC. The analysis was done for each RP arm separately and thus the Zerobias data was firstly required to pass the following criteria:

1. no trigger in any RP or trigger in exactly one arm (two RPs) with exactly one reconstructed proton track in that arm,
2. veto on any signal in small BBC tiles or ZDC on the same side of the IP as RP under consideration,
3. no reconstructed vertex in TPC or exactly one vertex with at least two TOF-matched tracks passing the quality criteria. The latter includes also signal in BBC small tiles on the opposite side of the IP to the RP under study.

The sample of selected Zerobias data with total number of events N was divided into four classes:

$$N = N(P,S) + N(R,S) + N(P,T) + N(R,T) \tag{4.1}$$

where: $N(P,S)$ is the number of events with reconstructed proton in exactly one RP and reconstructed vertex in TPC, $N(R,S)$ is the number of events with no trigger in any RP and reconstructed vertex in TPC, $N(P,T)$ is the number of events with reconstructed proton in exactly one RP and no reconstructed vertex in TPC, $N(R,T)$ is the number of events with no trigger in any RP and no reconstructed vertex in TPC.

Since the signature of the signal is a reconstructed proton in exactly one RP and a reconstructed vertex in TPC, the number of such events can be expressed as:

$$N(P,S) = N\left(p_3 + p_1 p_2\right) \tag{4.2}$$

where: p_1 is the probability that there is a reconstructed proton in RP and there is no reconstructed vertex in TPC, p_2 is the probability that there is no reconstructed proton in RP and there is a reconstructed vertex in TPC, p_3 is the probability that there is a reconstructed proton in RP and there is a reconstructed vertex in TPC (not accidental).

The other classes of interaction given in Eq. (4.1) can be expressed in terms of the above probabilities as:

$$\begin{aligned} N(R,S) =& N(1-p_1)p_2(1-p_3) \\ N(P,T) =& N(1-p_2)p_1(1-p_3) \\ N(R,T) =& N(1-p_1)(1-p_2)(1-p_3) \end{aligned} \tag{4.3}$$

Finally, the accidental background contribution $A_{\mathrm{bkg}}^{\mathrm{accidental}}$ is given by:

$$A_{\mathrm{bkg}}^{\mathrm{accidental}} = \frac{p_1 p_2}{p_3 + p_1 p_2} = \frac{N(R,S)N(P,T)N}{N(R)N(T)N(P,S)} \tag{4.4}$$

where: $N(R) = N(R,S) + N(R,T)$ and $N(T) = N(P,T) + N(R,T)$.

The shapes of the accidental background to the TPC-related distributions come from the above Zerobias data events which pass all the analysis selection except having no trigger in any RP and thus fail the overall selection. On the other hand, the templates corresponding to RP distributions are from protons in the above data sets but with no reconstructed vertex in the TPC. The normalization is obtained from the data-driven probabilities.

The selection of Zerobias events may provide some bias to the normalization of the accidental background. As a systematic check, the criteria for Zerobias selection were changed to:

1. no trigger in any RP or trigger in exactly one arm (two RPs) with *no more* than one reconstructed proton track in that arm,

2. veto on any signal in small BBC tiles or ZDC on the same side of the IP as RP under study,

3. no reconstructed vertex in TPC or exactly one vertex (not necessarily with two TOF-matched tracks passing the quality criteria). The requirement of signal in BBC small tiles remains unchanged.

As a result of this change in the procedure, the accidental background normalization increases twice with respect to the nominal value. Therefore, the background changes by $\pm 50\%$ was taken as a systematic uncertainty related to the accidentals.

4.2 Non-SD Background

The background contributions coming from Non-Diffractive (ND), Double Diffraction (DD) and Central Diffraction (CD) events are estimated from MC simulations. Protons from elastic interactions and beam halo are not included in the simulation. SD background signatures which are modeled in th MC simulations are only coming from :

- forward protons produced in the SD, CD or DD diffractive systems or through non-diffractive QCD,

- reconstructed tracks coming from showering.

Figure 4.1 shows the uncorrected ξ and t distributions in data compared to various MC models: PYTHIA 8 A2 (MBR), PYTHIA 8 A2 (MBR-tuned) and EPOS. The MC distributions are split into SD, ND, DD and CD components. For EPOS low mass excitation of the proton remnant (SD') is separated from the ND events. Additionally, the accidental background is also shown. Without arbitrary suppression of diffractive cross sections at large ξ PYTHIA8 A2 (MBR-tuned) predictions agree much better with the data and result also in a suppression of non-SD events. EPOS describes data better than PYTHIA8 but shows a dominant contribution of SD' events. All MCs predict significant non-SD background at large ξ, thereby the analysis was limited to $\xi < 0.2$.

On the other hand, Figs. 4.2 to 4.4 show the uncorrected distributions of variables used in the later analysis: n_{sel}, p_{T} an $\bar{\eta}$. The background contributions from non-SD interactions differ a bit between each other, i.e. EPOS predicts significantly larger CD contribution, whereas DD and ND are suppressed in PYTHIA 8 A2 (MBR-tuned). As a result PYTHIA 8 A2 (MBR) is used as the default model of non-SD with systematic uncertainty ±50%, which covers all differences between the models.

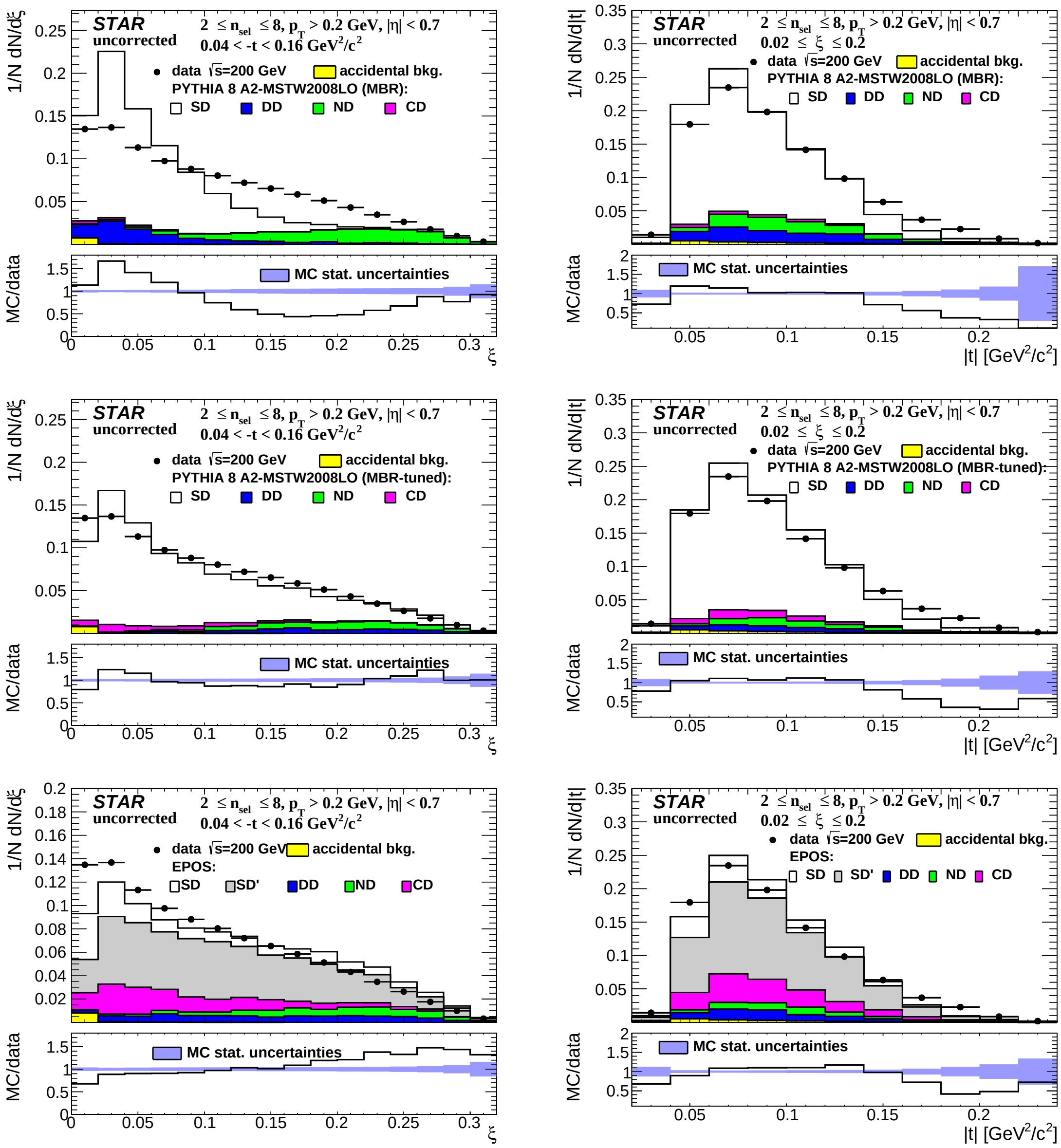

Figure 4.1: Uncorrected distributions of data compared to various MC models: (top) PYTHIA8 A2 (MBR), (middle) PYTHIA8 A2 (MBR-tuned) and (bottom) EPOS, as a function of (left column) ξ and (right column) $|t|$.

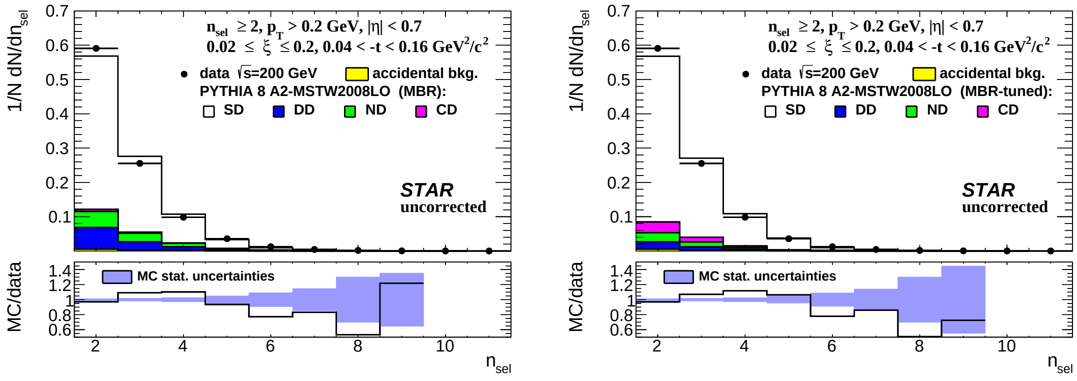

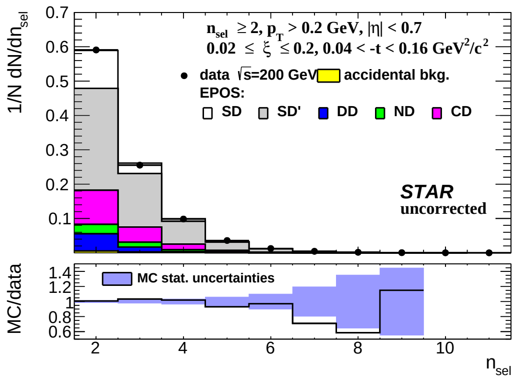

Figure 4.2: Uncorrected distributions of data compared to various MC models: (top left) PYTHIA8 A2 (MBR), (top right) PYTHIA8 A2 (MBR-tuned) and (bottom) EPOS, as a function of n_{sel}.

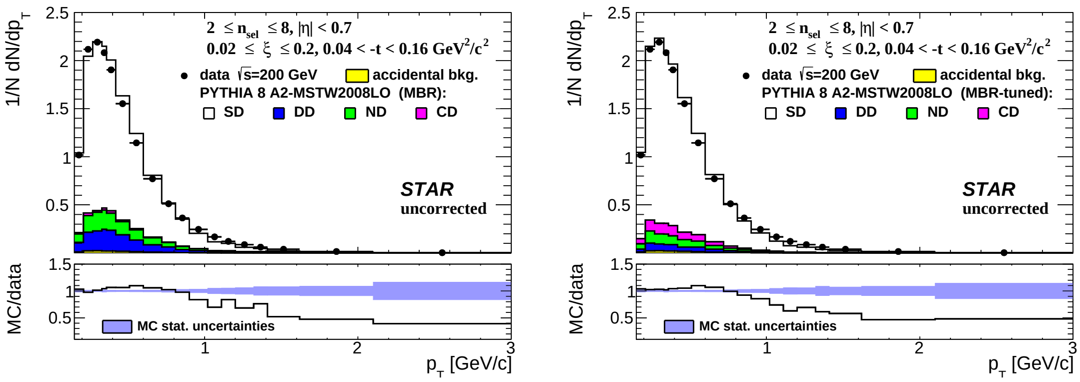

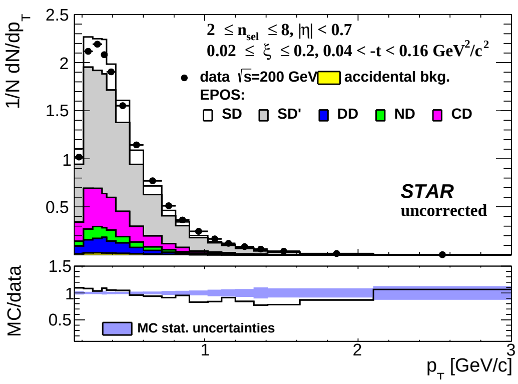

Figure 4.3: Uncorrected distributions of data compared to various MC models: (top left) PYTHIA8 A2 (MBR), (top right) PYTHIA8 A2 (MBR-tuned) and (bottom) EPOS, as a function of p_{T}.

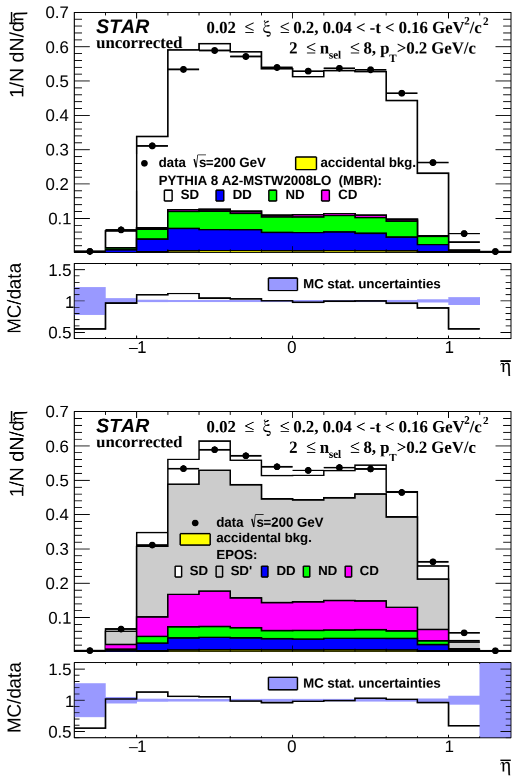

Figure 4.4: Uncorrected distributions of data compared to various MC models: (top left) PYTHIA8 A2 (MBR), (top right) PYTHIA8 A2 (MBR-tuned) and (bottom) EPOS, as a function of $\bar{\eta}$.

4.3 Background from Non-Primary Tracks

Reconstructed tracks matched to a non-primary particle originate mainly from the following sources:

- decays of short-lived primary particles with strange quark content (mostly K^0, Λ^0),
- photons from π^0 and η decays which are converting to e^+e^-,
- hadronic interactions of particles with the beam-pipe or detector dead material.

Figure 4.5 shows the background $f_{\mathrm{bkg}}(p_{\mathrm{T}}, \eta)$ and fake track $f_{\mathrm{fake}}(p_{\mathrm{T}}, \eta)$ contribution to reconstructed tracks as a function of p_{T} and η. There were no differences observed in the background contribution in different ξ ranges, hence, all three ξ ranges were merged for this study. The highest background fraction, which varies between $5 - 10\%$, was found to be at low p_{T}. There is also a contribution from fake tracks coming from out-of-time pile-up or formed by a random combination of TPC hits. The fake track contribution was calculated in each ξ range separately and its change by $\pm 50\%$ was taken as a systematic uncertainty.

Proton Background

Secondary particles can be created due to the interaction of particles with detector dead-material. The proton sample contains background from such protons knocked out from the detector materials [8]. Most of these protons have large DCA and are not reconstructed as primary particles. However, the rest with small DCA are included in the primary track sample. Antiprotons do not have knockout background, hence the flat DCA tail is almost absent from their DCA distributions.

In order to correct for the knock-out background protons, sample enriched in proton background was used for background normalization, where DCA_{xy}, DCA_z and d_0 cuts were abandoned. Additionally, at least one, instead of exactly one, reconstructed vertex was allowed in this

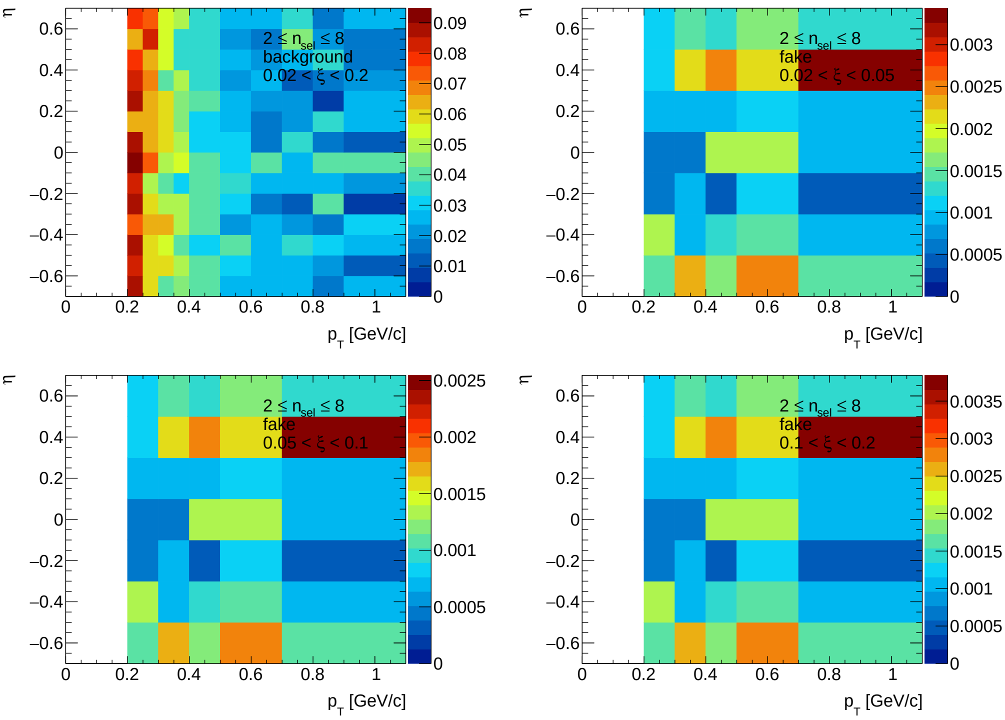

Figure 4.5: (top left) Distribution of fraction of selected tracks associated with non-primary particles in the range $0.02 < \xi < 0.2$ and distributions of fraction of tracks which are not associated with true-level particles for three ranges of ξ: (top right) $0.02 < \xi < 0.05$, (bottom left) $0.05 < \xi < 0.1$, (bottom right) $0.1 < \xi < 0.2$.

sample. Figures 4.6 and 4.7 show the DCA distributions of protons and antiprotons, respectively, for nominal (bottom) and background enriched (top) samples. The distributions for other p_{T} and ξ regions are shown in Appendix B. The protons and antiprotons are selected by a dE/dx cut of $-1 < n\sigma_{p,\bar{p}} < 3$ where $n\sigma_{p,\bar{p}}$ is given by Eq. (7.11). The fraction of knock-out protons within the selected sample is determined via a MC template normalization method. The templates of reconstructed tracks with dE/dx corresponding to the proton and antiproton are obtained from MC separately for:

- primary (anti)protons,
- knock-out background protons (labeled as dead-material),
- fake tracks,
- secondary particles with dE/dx of (anti)proton (labeled as wrong PID - sec.),
- tracks associated with primary (anti)protons, but with the reconstructed vertex not matched to true-level primary vertex (labeled as wrong vtx),
- reconstructed track is partially matched to true-level particle (labeled as wrong match, track to true-level particle matching is described in **??**), i.e. track and true-level particle have appropriate number of common hit points but the distance between true-level particle and track is too large, $\delta^2(\eta, \phi) > (0.15)^2$,
- primary particles with dE/dx of (anti)proton (labeled as wrong PID - prim.),
- (anti)proton as a product of short-lived decays, mainly Λ^0 (labeled as feed-down).

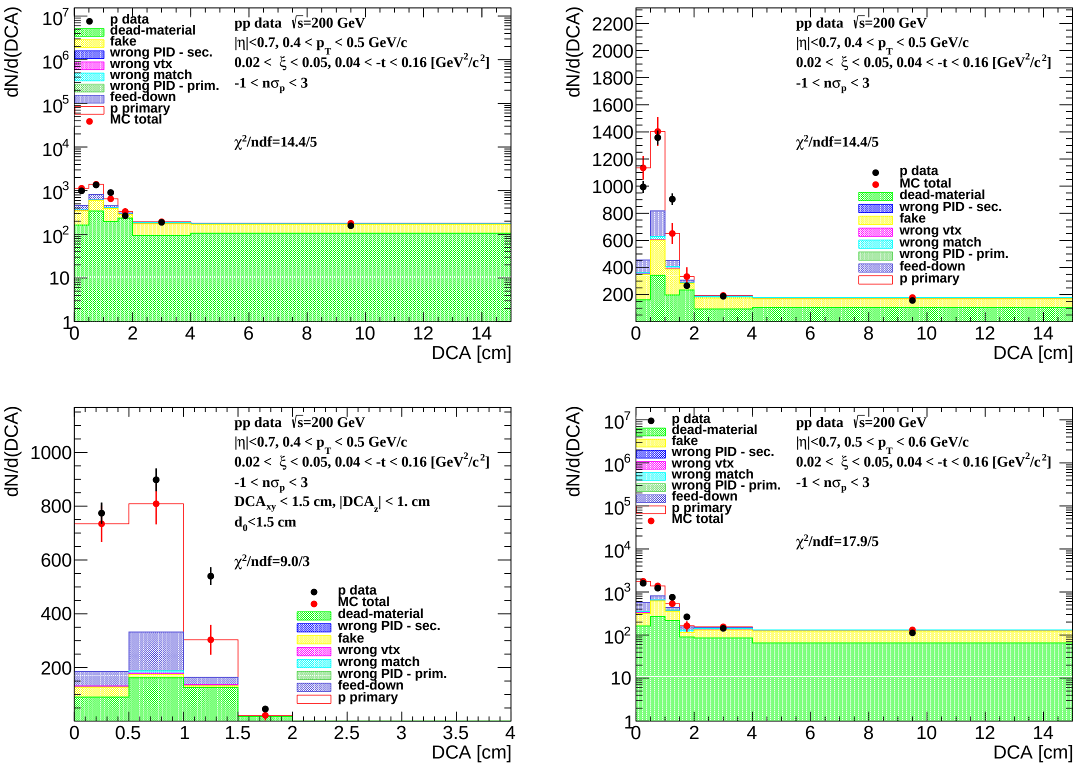

Figure 4.6: The DCA distributions of protons for $0.4 < p_T < 0.5$ GeV/c shown for single range of $0.02 < \xi < 0.05$ (shown in log and linear scale in left and right column, respectively). The MC constributions are shown after scaling the dead-material template to data. (top) Background enriched samples were used in the normalization procedure, whereas (bottom) the proton background was estimated from the nominal sample.

First, the background enriched sample was used (Fig. 4.6, top), where the template of knock-out background protons was normalized to the number of events in the fake-subtracted tail of the DCA distribution, $2 <$ DCA < 15 cm. Next the knock-out proton and fake background was subtracted from the DCA distribution and the sum of other templates was normalized to the number of events in the signal region, DCA < 1.5 cm.

The fraction of the knock-out proton background in the signal region, DCA < 1.5, was estimated from the nominal sample (Fig. 4.6, bottom), where DCA_{xy}, DCA_z and d_0 track cuts were applied and exactly one reconstructed vertex was required. The normalization of each MC contribution was kept the same as that estimated for the background enriched sample. Figure 4.8 shows the knock-out proton background as a function of p_T in three ranges of ξ. The following functional form was found to describe the background protons well:

$$f^{p}_{\mathrm{bkg}}\left(p_\mathrm{T}\right) = p_0 \exp\left(p_1 p_\mathrm{T}\right) \tag{4.5}$$

where p_0 and p_1 are free parameters obtained from a fit.

The obtained fraction of knock-out background protons is approximately 20% at $p_\mathrm{T} = 0.45$ GeV/c and less than 10% at $p_\mathrm{T} = 1.0$ GeV/c. The fraction of knock-out background protons depends on a number of factors, including the amount of detector material, analysis cuts and the ξ of diffractive proton.

Figure 4.7 shows the corresponding DCA distributions with MC templates for antiprotons, where the background form knock-out particles is not present. The MC templates fairly well describe the DCA distribution for both, protons and antiprotons. Additionally, there is a small

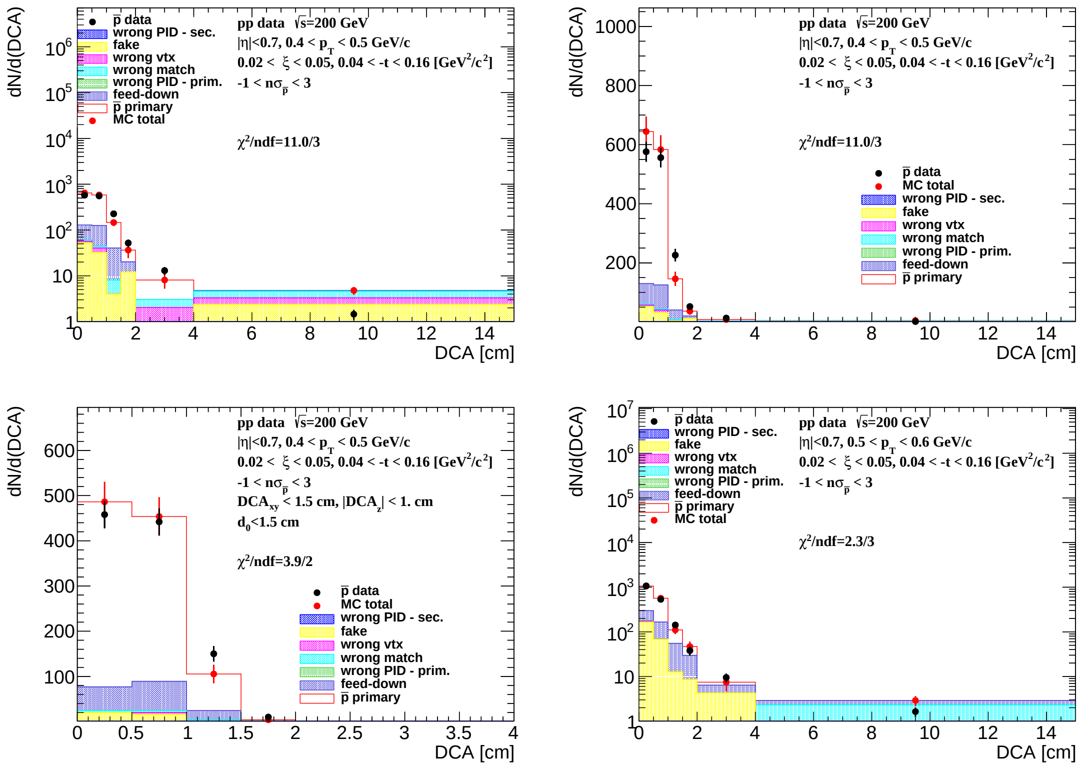

Figure 4.7: The DCA distributions of antiprotons for $0.4 < p_{\mathrm{T}} < 0.5$ GeV/c shown for one range of $0.02 < \xi < 0.05$ (log and linear scale in left and right column, respectively). The MC controbutions are shown as colour histograms. (top) Background enriched and (bottom) nominal samples were used.

($< 1\%$) background contribution, present for both particles, which also was taken into account and subtracted. It originates from reconstructed tracks which have the appropriate number of common hit points with true-level particle, but the distance between them is too large, i.e. $\delta^2(\eta,\phi) > (0.15)^2$.

Systematic Uncertainty Related to Proton Background

The method of knock-out proton background estimation introduces independent systematic uncertainties which are added in quadrature.

First, the normalization interval of the knock-out proton background template in the background enriched sample was changed to $4 < \mathrm{DCA} < 15$ cm. This introduced a relative systematic uncertainty of up to 30% for $p_{\mathrm{T}} \approx 1.0$ GeV/c.

The knock-out proton background contribution was parameterized as it is shown in Eq. (4.5). The systematic uncertainty related to the fit procedure was estimated by varying the parameters, p_0 and p_1, by their statistical uncertainties ($\pm 1\sigma$). As a result, a relative systematic uncertainties of about 10% were obtained.

Figure 4.9 (top left) shows the data to MC ratio of the number of events in the background dominated region, $2 < \mathrm{DCA} < 15$ cm. The shape of the DCA distribution in data differs from that observed in simulation. Thus, the following functional form was used to estimate the slope between data and MC:

$$\frac{\mathrm{data}}{\mathrm{MC}}(\mathrm{DCA}) = A(\mathrm{DCA} - 8.5) + B \tag{4.6}$$

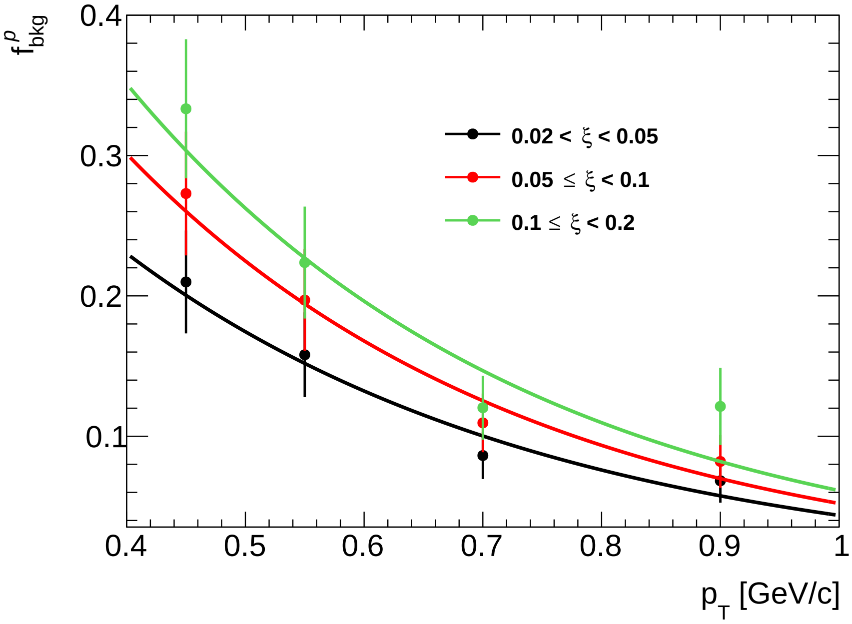

Figure 4.8: The fraction of knock-out proton background as a function of $p_{\rm T}$ in three ranges of ξ with fitted parametrizations.

where A (slope) and B are fit free parameters. An extrapolation of the slope was used to estimate how many more tail-like tracks would fit into the signal region and a systematic uncertainty, which varies up to 5% for $0.02 < \xi < 0.05$, was introduced.

All above components of the systematic uncertainty related to the knock-out proton background are shown in Fig. 4.9.

Pion Background

The pion spectra are corrected for weak decays (mainly of K^0_S and Λ^0), muon contribution and background from the detector dead-material interactions. The pion decay muons can be identified as pions due to the similar masses. These contributions are obtained from MC. Figure 4.10 shows the background contribution to the pion spectra as a function of $p_{\rm T}$ in three ranges of ξ, separately for π^- and π^+. Since there were negligible differences observed between these three ranges of ξ, the background contribution was averaged over ξ. The following parametrization was found to describe it:

$$f^{\pi}_{\rm bkg}\,(p_{\rm T}) = a_0 \exp(a_1 p_{\rm T}) + a_2 p_{\rm T}^2 + a_3 p_{\rm T} \tag{4.7}$$

where a_i, $i = 0, \ldots, 3$ are free paramaters of the fitted function.

The pion background contribution varies between 5% at low-$p_{\rm T}$ ($p_{\rm T} = 0.25$ GeV/c) and about 1% at $p_{\rm T} = 1.0$ GeV/c for both negatively and positively charged pions.

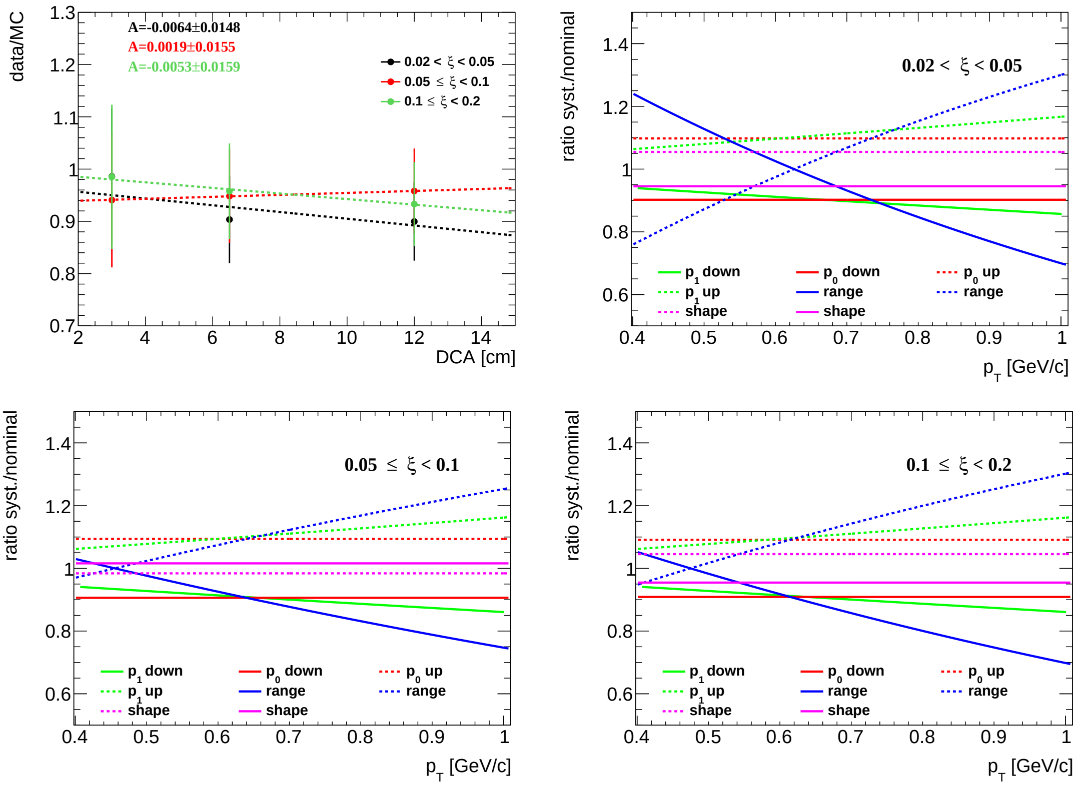

Figure 4.9: (top left) Data to MC ratio of the number of events in the background dominated region in three ranges of ξ with fitted functional form given by Eq. (4.6). (top right and bottom) Components of the systematic uncertainty related to the knock-out background protons contribution in three ξ ranges.

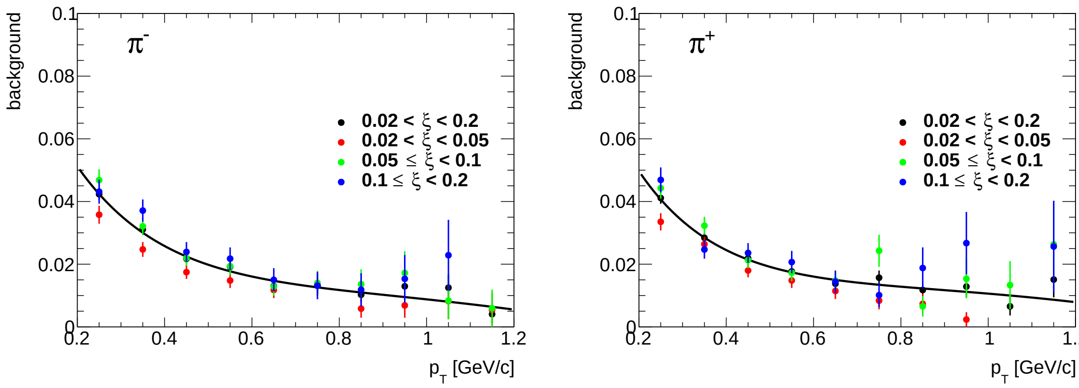

Figure 4.10: Pion background fraction as a function of p_{T} shown separately for (left) negatively and (right) positively charged pions in three ranges of ξ: (red) $0.02 < \xi < 0.05$, (green) $0.05 < \xi < 0.1$, (blue) $0.1 < \xi < 0.2$. (black) The pion background averaged over three ranges of ξ with fitted parametrization is also shown.

5. Selection Efficiencies

5.1 Vertex Reconstruction

In *pp* collisions, where the charged-particle multiplicity is low, the vertex finding algorithm sometimes fails to find the primary vertex. In addition, at high luminosity, vertex finder can fail due to the contribution of pile-up events and providing a wrong reconstructed vertex. In this study we required at least two reconstructed global tracks $n_{\mathrm{sel}}^{\mathrm{global}} \geq 2$ passing all the quality cuts listed in Sec 3.2 but without DCA_{xy} and DCA_{z} cuts. Additionally, MC events were accepted if the z-coordinate of the true-level primary vertex was between -80 and 80 cm. All corrections, described in this section, were calculated in three ranges of ξ separately.

The following quality cuts had to be passed by the global tracks used in the vertex reconstruction:

1. Tracks must be matched with hits reconstructed in TOF,
2. The number of the TPC hits used in the helix fit $N_{\mathrm{hits}}^{\mathrm{fit}}$ must be greater than 20,
3. The ratio of the number of TPC hits used in the helix fit to the number of possible TPC hits $N_{\mathrm{hits}}^{\mathrm{fit}}/N_{\mathrm{hits}}^{\mathrm{poss}}$ must be greater than 0.52,
4. The transverse impact parameter with respect to the beamline d_0 must be less than 2 cm,
5. The track's transverse momentum p_{T} must be greater than 0.2 GeV/c.

The above track selection criteria are different than those used in the analysis. Thus, primary vertex reconstruction efficiency and fake vertex rate were calculated as a function of the number of global tracks used in vertexing $n_{\mathrm{vrt}}^{\mathrm{global}}$ instead of $n_{\mathrm{sel}}^{\mathrm{global}}$.

In the analysis exactly one vertex with $n_{\mathrm{sel}} \geq 2$ is required. The reconstructed vertex with the label *best* is the one with the highest number of TOF-matched tracks. Since the fake vertices (not matched to the true-level primary vertex) are allowed in the analysis, the overall vertex-finding efficiency, $\epsilon_{\mathrm{vrt}}\left(n_{\mathrm{vrt}}^{\mathrm{global}}\right)$, is expressed as:

$$\epsilon_{\mathrm{vrt}}\left(n_{\mathrm{vrt}}^{\mathrm{global}}\right) = \epsilon_{\mathrm{vrt}}^{\mathrm{best}}\left(n_{\mathrm{vrt}}^{\mathrm{global}}\right) + \delta_{\mathrm{vrt}}^{\mathrm{fake}}\left(n_{\mathrm{vrt}}^{\mathrm{global}}\right) \tag{5.1}$$

where:

$\epsilon_{\mathrm{vrt}}^{\mathrm{best}}\left(n_{\mathrm{vrt}}^{\mathrm{global}}\right)$ is the primary vertex reconstruction efficiency, determined as the ratio of the number of good reconstructed events (reconstructed best primary vertex with $n_{\mathrm{sel}} \geq 2$) to the number of input MC events, where the reconstructed vertex is matched to the true-level primary vertex,

$\delta_{\mathrm{vrt}}^{\mathrm{fake}}\left(n_{\mathrm{vrt}}^{\mathrm{global}}\right)$ is the fake vertex rate, determined as the ratio of the number of good reconstructed events (reconstructed best primary vertex with $n_{\mathrm{sel}} \geq 2$) to the number of input MC events, where the reconstructed vertex is not matched to the true-level primary vertex.

The vertex-finding efficiency as a function of $n_{\mathrm{vrt}}^{\mathrm{global}}$ is shown in Fig. 5.1 (left). When there are exactly two global tracks used in the vertex reconstruction, $n_{\mathrm{vrt}}^{\mathrm{global}} = 2$, the longitudinal distance between these tracks $|\Delta z_0|$ is used by the vertex-finding algorithm. Therefore, the vertex finding efficiency for such events $\epsilon_{\mathrm{vrt}}\left(|\Delta z_0|\right)$ is given by:

$$\epsilon_{\mathrm{vrt}}\left(|\Delta z_0|\right) = \epsilon_{\mathrm{vrt}}^{\mathrm{best}}\left(|\Delta z_0|\right) + \delta_{\mathrm{vrt}}^{\mathrm{fake}}\left(|\Delta z_0|\right) \tag{5.2}$$

where: $\epsilon_{\mathrm{vrt}}^{\mathrm{best}}\left(|\Delta z_0|\right)$ is the primary vertex reconstruction efficiency, $\delta_{\mathrm{vrt}}^{\mathrm{fake}}\left(|\Delta z_0|\right)$ is the fake vertex rate.

Figure 5.1 (right) shows the vertex finding efficiency for events with $n^{\text{global}}_{\text{vrt}} = 2$. This efficiency is smaller than 20% for tracks with $|\Delta z_0| > 2$ cm, hence the analysis was limited to events with $|\Delta z_0| < 2$ cm, when $n^{\text{global}}_{\text{vrt}} = 2$.

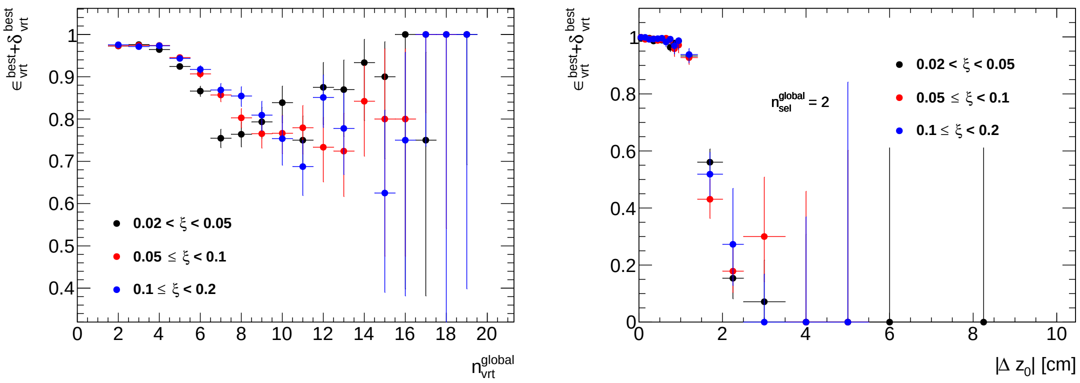

Figure 5.1: Vertex-finding efficiency in three ranges of ξ as a function of (left) $n^{\text{global}}_{\text{vrt}}$ and (right) with respect to the $|\Delta z_0|$ between reconstructed tracks in events with $n^{\text{global}}_{\text{vrt}} = 2$.

Events with reconstructed best vertex are rejected if there are:

a) more than one additional TOF vertices,

b) additional secondary TOF vertex from interactions with the detector dead-material,

c) additional fake TOF vertex,

d) additional primary TOF vertex (vertex splitting or background vertex reconstructed as best vertex),

e) additional decay TOF vertex.

The correction for vetoing such events, $\epsilon^{\text{veto}}_{\text{vrt}}\left(n^{\text{global}}_{\text{vrt}}\right)$, is given by:

$$\begin{aligned}\epsilon^{\text{veto}}_{\text{vrt}}\left(n^{\text{global}}_{\text{vrt}}\right) &= 1 - \frac{\text{number of events with more than one reconstructed TOF vertex}}{\text{number of events with at least one reconstructed TOF vertex}} \\ &= 1 - \epsilon_a - \epsilon_b - \epsilon_c - \epsilon_d - \epsilon_e\end{aligned} \tag{5.3}$$

where $\epsilon_a - \epsilon_e$ are the fractions of events with additional vertices, whose labels are listed above.

As before, the correction was calculated as a function of $|\Delta z_0|$ for events with $n^{\text{global}}_{\text{vrt}} = 2$. Figure 5.3 shows the fraction of multi-vertex events with respect to the $n^{\text{global}}_{\text{vrt}}$. There is a large fraction of events ($> 50\%$) with additional background vertices for $n^{\text{global}}_{\text{vrt}} \geq 9$, what would result in large correction factor. Hence, the analysis was limited to events with $n_{\text{sel}} \leq 8$. On the other hand, the total fraction of multi-vertex events, $\epsilon_a + \epsilon_b + \epsilon_c + \epsilon_d + \epsilon_e$, as a function of $|\Delta z_0|$, shown in Fig. 5.2, demonstrates that $\epsilon^{\text{veto}}_{\text{vrt}}(|\Delta z_0|)$ is very large ($> 98\%$) for events with $n^{\text{global}}_{\text{vrt}} = 2$.

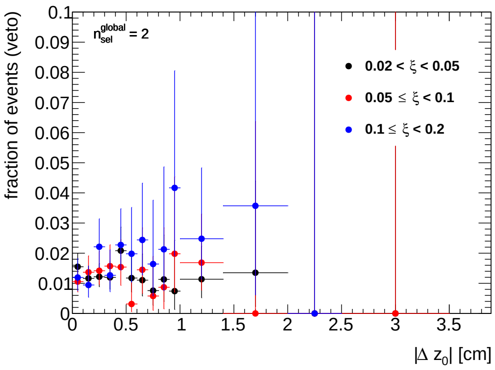

Figure 5.2: Total fraction of multi-vertex events as a function of $|\Delta z_0|$ for events with $n_{\mathrm{vrt}}^{\mathrm{global}} = 2$ in three ranges of ξ.

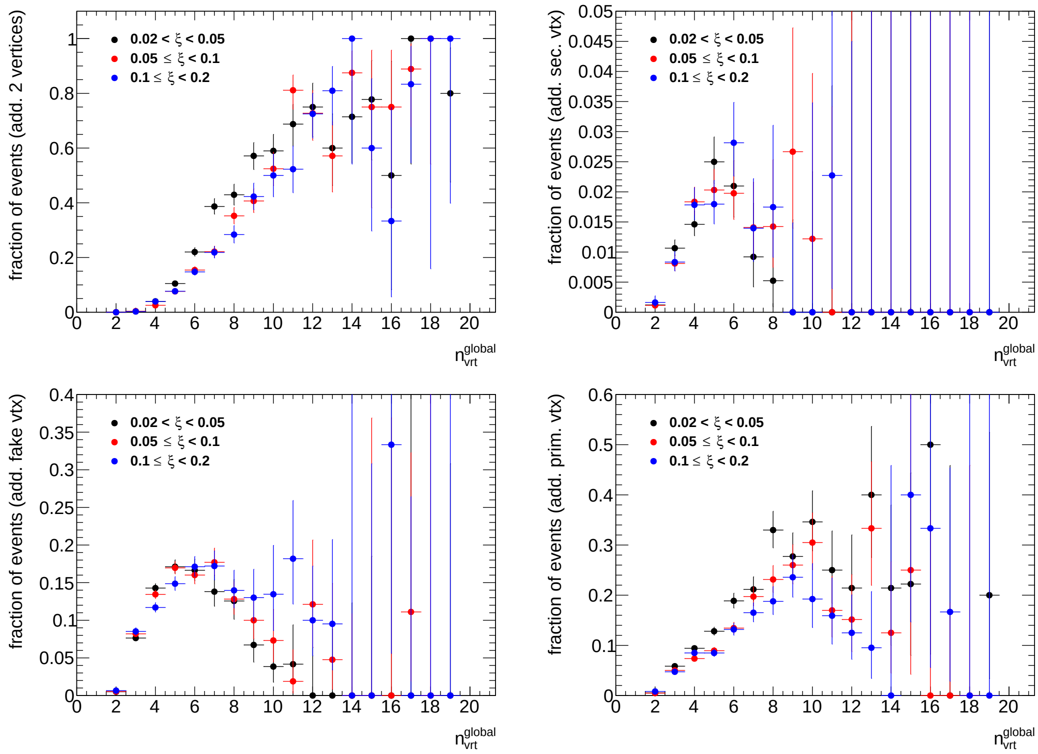

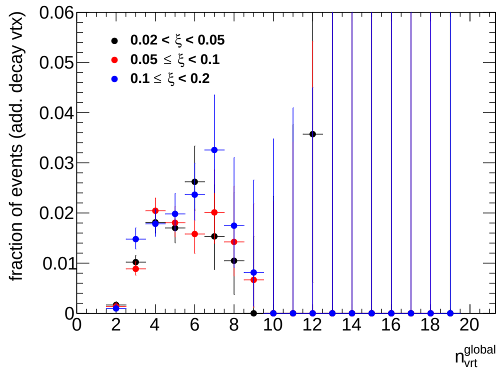

Figure 5.3: Fraction of multi-vertex events with respect to the $n_{\mathrm{vrt}}^{\mathrm{global}}$ in three ranges of ξ. Each contribution is shown separately: (top left) more than one additional vertices, (top right) additional secondary vertex from the interactions with the detector dead-material, (middle left) additional fake vertex, (middle right) additional primary vertex and (bottom) additional decay vertex.

5.2 Correction to BBC-Small

The SDT trigger conditions imposed signal in RPs and veto on any signal in the same-side small BBC tiles, whereas signal in the opposite-side BBC-small was required by the offline event selection. A common BBC-small efficiency, ϵ_{BBC}, was obtained as a function of each measured quantity using PYTHIA 8 4C (SaS) embedded into Zerobias data. The efficiency was calculated for events within fiducial region as follows:

$$\epsilon_{\mathrm{BBC}} = \frac{\text{number of MC events satysfying the BBC-small selection criteria}}{\text{number of MC events}} \tag{5.4}$$

Figures 5.4 to 5.6 show the fraction of generated true-level MC events, within the fiducial region of the measurement, in which the selection criteria on BBC-small signal and veto are fulfilled. The ϵ_{BBC} varies from about 90% for events with ξ within $0.02 - 0.05$ to about 65% for events with $0.1 < \xi < 0.2$.

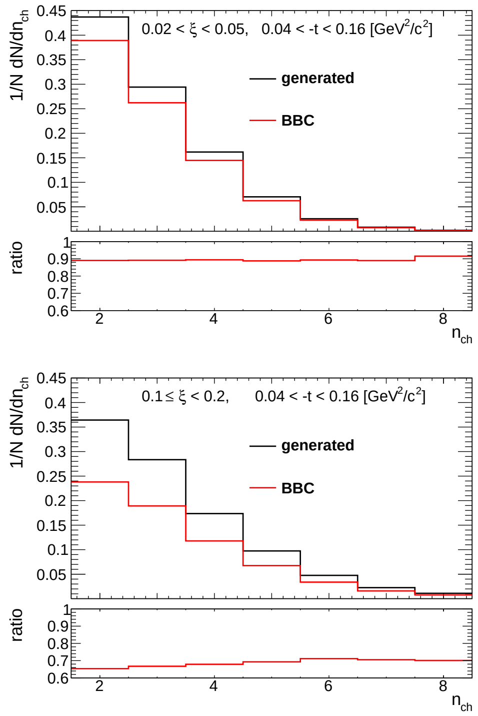

Figure 5.4: Number of true-level MC events which fulfill BBC-small selection criteria as a function of n_{ch} in three ranges of ξ. The fraction of such events is shown in the bottom pad.

When the data is corrected for BBC-small efficiency, there is an assumption that the MC used in the analysis, PYTHIA 8 4C (SaS), provides correct correlation between the true value of ξ and forward particles produced in the BBC acceptance region. The uncertainty related to this correction is estimated by using HERWIG MC sample, where the hadronisation model is different from that used in PYTHIA 8. Figure 5.7 shows the PYTHIA 8 prediction on BBC efficiency divided by the HERWIG prediction in three ranges of ξ. The deviations between these two models are of the order of 2% at $0.05 < \xi < 0.1$ and about 10% for other two ξ regions. The difference between these two hadronisation models is used as systematic uncertainty.

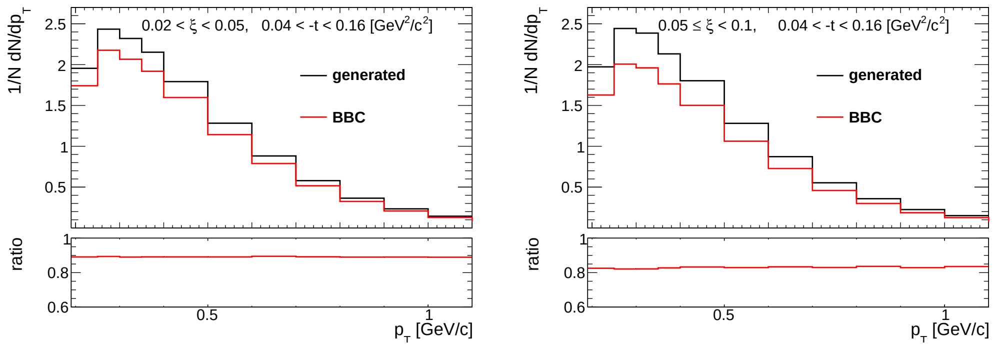

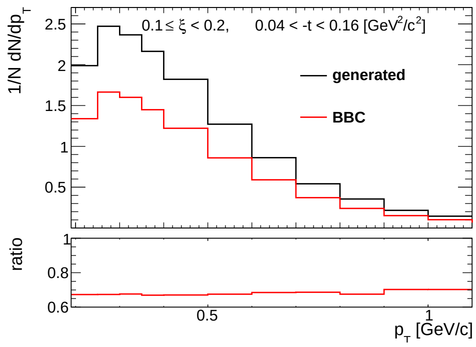

Figure 5.5: Number of true-level MC events which fulfill BBC-small selection criteria as a function of p_{T} in three ranges of ξ. The fraction of such events is shown in the bottom pad.

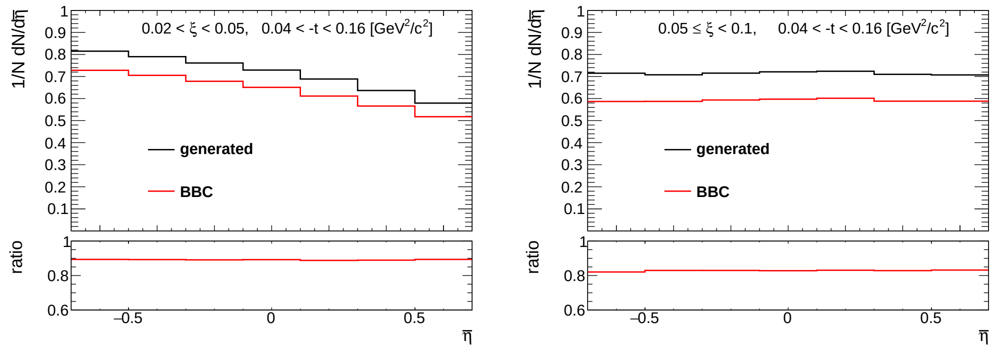

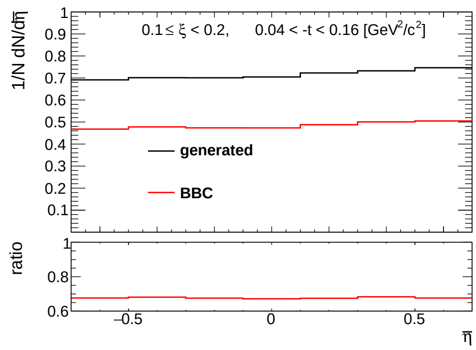

Figure 5.6: Number of true-level MC events which fulfill BBC-small selection criteria as a function of $\bar{\eta}$ in three ranges of ξ. The fraction of such events is shown in the bottom pad.

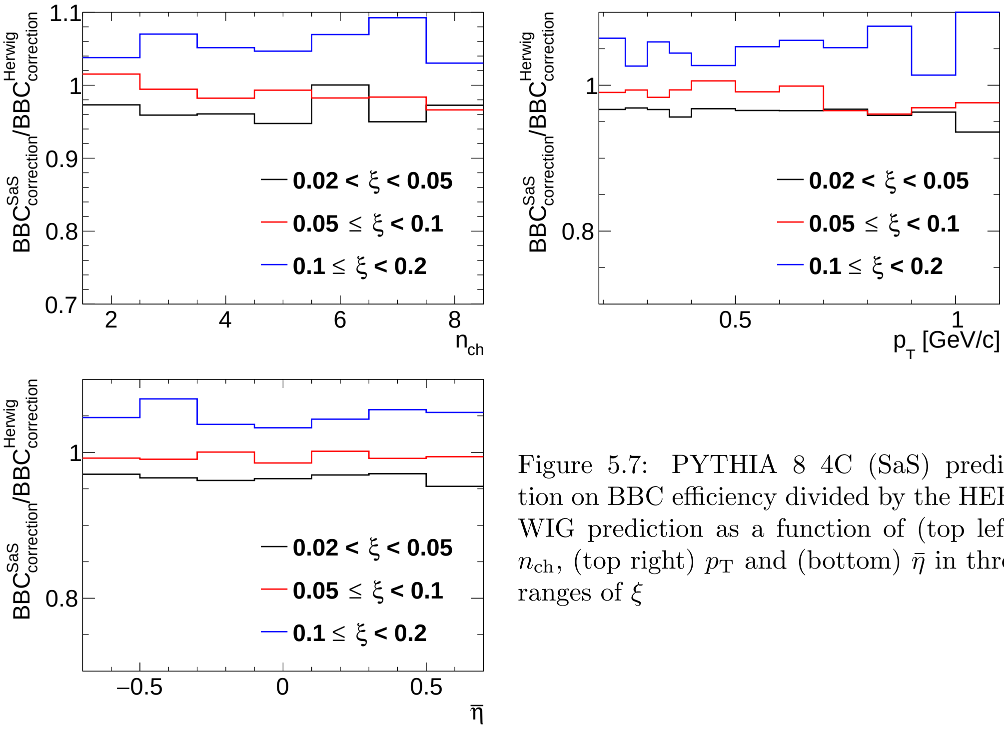

Figure 5.7: PYTHIA 8 4C (SaS) prediction on BBC efficiency divided by the HERWIG prediction as a function of (top left) $n_{\rm ch}$, (top right) $p_{\rm T}$ and (bottom) $\bar{\eta}$ in three ranges of ξ

6. Migrations into and out of the Fiducial Region

In this section the corrections due to the migrations of tracks and forward proton into and out of the fiducial region are described.

6.1 Migrations of Tracks into and out of the Fiducial Region

The procedure, described in this section, accounts for migrations of tracks into and out of the fiducial region, which originate from TPC resolution effects. The correction factor for such tracks, $f_{\mathrm{okr}}(p_T, \eta)$ is defined as follows:

$$f_{\mathrm{okr}}(p_{\mathrm{T}}, \eta) = \frac{1 - f^{-}_{\mathrm{okr}}(p_{\mathrm{T}}, \eta)}{1 - f^{+}_{okr}(p_{\mathrm{T}}, \eta)} \tag{6.1}$$

where:

$f^{-}_{\mathrm{okr}}(p_{\mathrm{T}}, \eta)$ is the fraction of reconstructed tracks for which the corresponding primary particle is outside of the kinematic range of the measurement,

$f^{+}_{\mathrm{okr}}(p_{\mathrm{T}}, \eta)$ is the fraction of primary particles for which the corresponding reconstructed track is outside of the kinematic range of the measurement.

The resulting residual migrations, shown in Fig. 6.1, were estimated using MC. The main effect was observed at $|\eta| \sim 0.7$, where about $2 - 6\%$ reconstructed tracks were associated to primary particle outside the fiducial region.

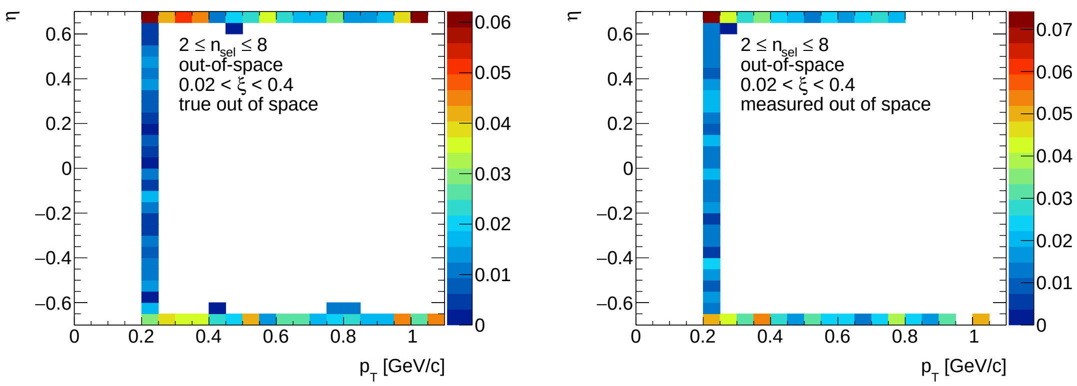

Figure 6.1: (left) Fraction of selected tracks migrating from outside of the kinematic range to the signal region and (right) fraction of particles for which the corresponding reconstructed track is outside the kinematic range of the measurement.

6.2 Migrations in ξ

The analysis was performed in three ranges of ξ. Thus, there are migrations into and out of these ξ regions. They mainly originate from the resolution of ξ, which is measured with the RPs. Figure 6.2 shows the resolution of measured ξ (denoted as ξ_{reco}) as a function of the true-level ξ

(denoted as ξ_{true}) with fitted zeroth order polynomial. The resolution of ξ_{reco} is fairly constant and equals to about 0.4%.

The corrections due to migrations into and out of ξ regions was defined as:

$$f_\xi = \frac{1 - f_\xi^-}{1 - f_\xi^+} \tag{6.2}$$

where:

- f_ξ^- is the fraction of events for which the corresponding true-level ξ_{true}, is outside of the ξ region,
- f_ξ^+ is the fraction of events for which the corresponding reconstructed ξ_{reco} is outside of the ξ region.

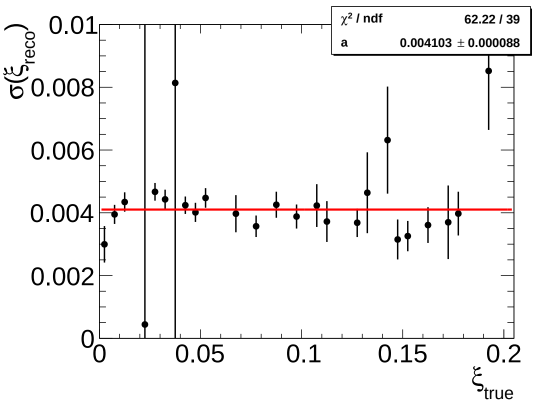

Figure 6.2: The resolution of ξ_{reco} as a function of ξ_{true}. The zeroth order polynomial, shown as red line, was fitted.

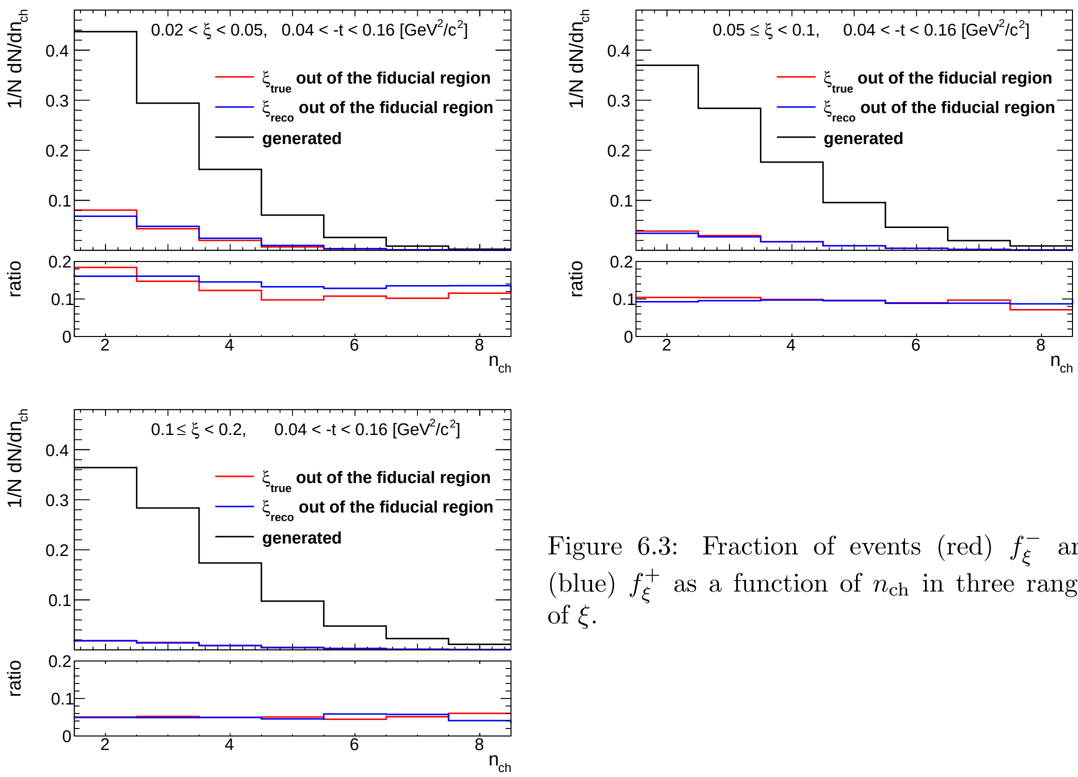

Figure 6.3: Fraction of events (red) f_ξ^- and (blue) f_ξ^+ as a function of n_{ch} in three ranges of ξ.

The f_ξ was calculated for each measured variable separately. Figures 6.3 to 6.5 show the fraction of events f_ξ^- and f_ξ^+ as a function of n_{ch}, p_{T} and $\bar{\eta}$. The largest differences between migrations into and out of the ξ regions were observed at $0.02 < \xi < 0.05$, where they are of the order of $2-3\%$. In the other ξ regions, the difference between f_ξ^- and f_ξ^+ is smaller than 1%.

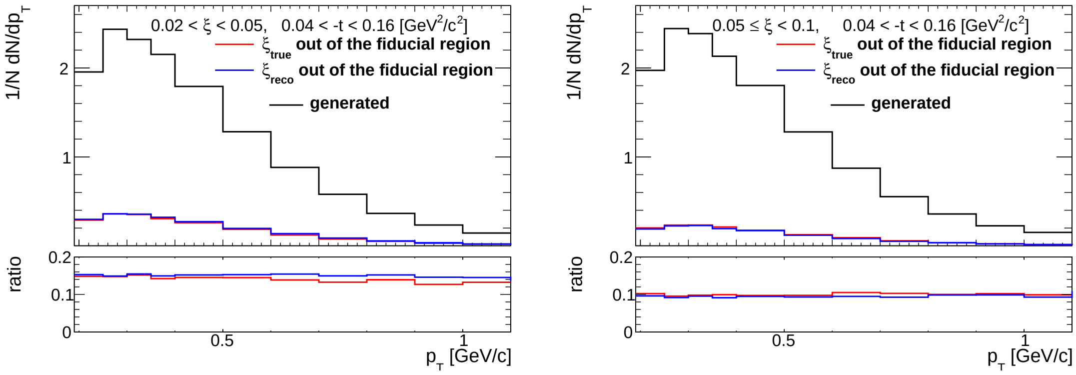

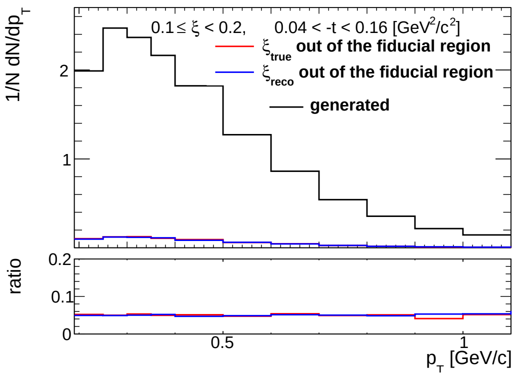

Figure 6.4: (red) Fraction of events f_ξ^- and (blue) f_ξ^+ as a function of p_{T} in three ranges of ξ.

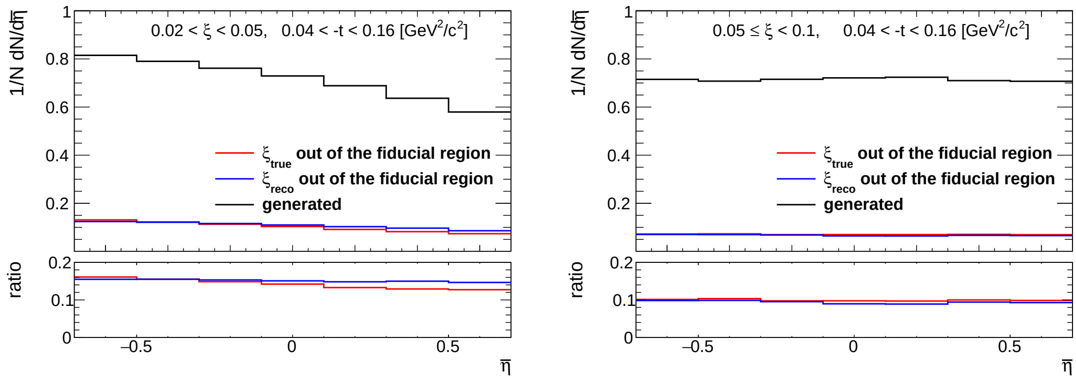

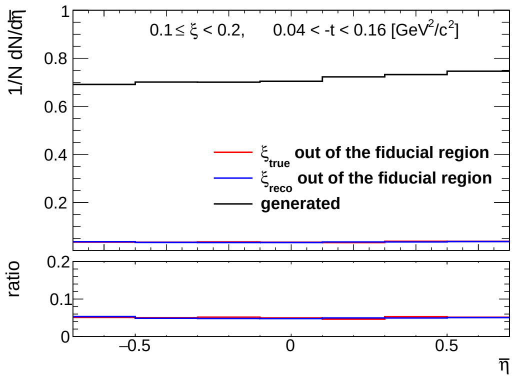

Figure 6.5: (red) Fraction of events f_ξ^- and (blue) f_ξ^+ as a function of $\bar{\eta}$ in three ranges of ξ.

7. Corrections and Unfolding Procedure

After subtraction of accidental and non-SD backgrounds, the data was corrected for detector inefficiencies to obtain the inclusive distributions of charged particles and particle to antiparticle (pion, kaon, proton and their antiparticle) multiplicity ratios. These corrections include:

- event-by-event weights due to vertex reconstruction efficiency:

$$w_{\mathrm{ev}}^{\mathrm{vrt}}\left(n_{\mathrm{vrt}}^{\mathrm{global}}, |\Delta z_0|\right) = \frac{1}{\epsilon_{\mathrm{vrt}}\left(n_{\mathrm{vrt}}^{\mathrm{global}}, |\Delta z_0|\right)} \cdot \frac{1}{\epsilon_{\mathrm{vrt}}^{\mathrm{veto}}\left(n_{\mathrm{vrt}}^{\mathrm{global}}, |\Delta z_0|\right)} \tag{7.1}$$

  where the $|\Delta z_0|$ dependence is only applicable for events with $n_{\mathrm{vrt}}^{\mathrm{global}}$ as described in Sec. 5.1.

- track-by-track weights due to track reconstruction efficiency, track backgrounds from non-primary tracks, migrations of tracks into and out of the fiducial region:

$$w_{\mathrm{trk}}\left(p_{\mathrm{T}}, \eta, V_z\right) = \frac{1 - f_{\mathrm{bkg}}\left(p_{\mathrm{T}}, \eta\right) - f_{\mathrm{fake}}\left(p_{\mathrm{T}}, \eta\right)}{\epsilon_{\mathrm{TPC}}\left(p_{\mathrm{T}}, \eta, V_z\right)\epsilon_{\mathrm{TOF}}\left(p_{\mathrm{T}}, \eta, V_z\right)} f_{\mathrm{okr}}\left(p_{\mathrm{T}}, \eta\right) \tag{7.2}$$

  where: $\epsilon_{\mathrm{TPC}}\left(p_{\mathrm{T}}, \eta, V_z\right)$ is TPC track reconstruction efficiency [1], $\epsilon_{\mathrm{TOF}}\left(p_{\mathrm{T}}, \eta, V_z\right)$ is TOF matching efficiency [1], $f_{\mathrm{okr}}\left(p_{\mathrm{T}}, \eta\right)$ is a factor accounting for migrations of tracks into and out of the fiducial region, $f_{\mathrm{bkg}}\left(p_{\mathrm{T}}, \eta\right)$ is a fraction of background tracks, and $f_{\mathrm{fake}}\left(p_{\mathrm{T}}, \eta\right)$ is a fraction of fake tracks.

- event-by-event (for n_{ch} distribution) or track-by-track (for p_{T}, $\bar{\eta}$ distributions) weights, f_{ξ}, due to migrations of events between three ξ regions.

Additionally, the obtained distributions were corrected for BBC-small efficiency, ϵ_{BBC}, using the following weight:

$$w_{\mathrm{BBC}} = \frac{1}{\epsilon_{\mathrm{BBC}}} \tag{7.3}$$

In the following sections, the correction procedure for each of the measured distributions is presented separately. The uncorrected distributions in a wider range are shown in Figs. 4.2 to 4.4.

7.1 Correction to $\mathrm{dN/dn_{ch}}$

In order to express the multiplicity distribution in terms of the number of charged particles, n_{ch}, instead of the number of selected tracks, n_{sel}, the observed n_{sel} distribution was corrected for detector effects after subtraction of accidental and non-SD backgrounds. The following procedure based on the Bayesian unfolding [9, 10] was used. First, the n_{sel} distribution was corrected for vertex reconstruction effects by applying event-by-event weights, $w_{\mathrm{ev}}^{\mathrm{vrt}}(n_{\mathrm{vrt}}^{\mathrm{global}}, |\Delta z_0|)$. The number of events in which n_{ch} are produced, $N_{\mathrm{ev}}(n_{\mathrm{ch}})$, can be associated with the number of events in which n_{sel} are reconstructed, $N_{\mathrm{ev}}(n_{\mathrm{sel}})$:

$$N_{\mathrm{ev}}\left(n_{\mathrm{ch}}\right) = N_{\mathrm{ev}}\left(n_{\mathrm{sel}}\right) \cdot P\left(n_{\mathrm{ch}} | n_{\mathrm{sel}}\right) \tag{7.4}$$

where $P(n_{\mathrm{ch}}|n_{\mathrm{sel}})$ is the conditional probability of having n_{ch} charged particles in an event in which n_{sel} tracks were found.
When there are several possible n_{sel} the number of events in which n_{ch} are produced is given by:

$$\begin{aligned} N_{\mathrm{ev}}(n_{\mathrm{ch}}) &= \sum_{n_{\mathrm{sel}} \geq 0} P(n_{\mathrm{ch}}|n_{\mathrm{sel}}) \cdot N_{\mathrm{ev}}(n_{\mathrm{sel}}) \\ &= \frac{1}{\epsilon^{m}(n_{\mathrm{ch}})\epsilon^{r}(n_{\mathrm{ch}})} \sum_{n_{\mathrm{sel}} \geq 2} P(n_{\mathrm{ch}}|n_{\mathrm{sel}}) \cdot N_{\mathrm{ev}}(n_{\mathrm{sel}}) \end{aligned} \tag{7.5}$$

where:

$\epsilon^m(n_{\rm ch})$ is a factor, which recovers events that are lost due to TPC track reconstuction and TOF matching inefficiencies, i.e. those with $n_{\rm ch} \geq 2$ but $n_{\rm sel} < 2$,

$\epsilon^r(n_{\rm ch})$ is a factor, which recovers events which are lost due to fake tracks, i.e. those with $n_{\rm ch} \leq 8$ but $n_{\rm sel} > 8$.

Figure 7.1 shows $\epsilon^m(n_{\rm ch})$ and $\epsilon^r(n_{\rm ch})$ in three ranges of ξ. Both corrections were derived from MC. The former varies from about 25% for $n_{\rm ch} = 2$ to 95% for $n_{\rm ch} = 8$, the latter is significantly smaller and varies up to 2% for $n_{\rm ch} = 8$.

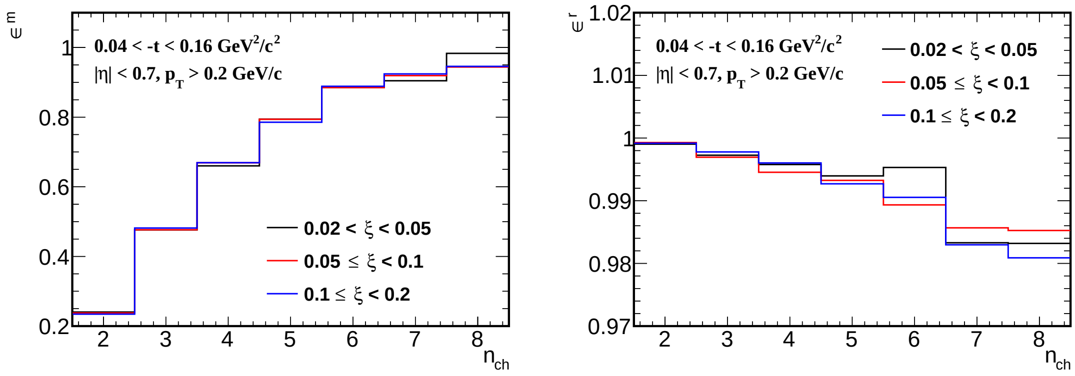

Figure 7.1: (left) $\epsilon^m(n_{\rm ch})$ and (right) $\epsilon^r(n_{\rm ch})$ calculated separately in three ranges of ξ.

The unknown probability $P(n_{\rm ch}|n_{\rm sel})$ can be derived using Bayes' theorem, which can be stated mathematically in terms of charged particle and charged track multiplicities as:

$$P\left(n_{\rm ch}\right) \cdot P\left(n_{\rm sel}|n_{\rm ch}\right) = P\left(n_{\rm ch}|n_{\rm sel}\right) \cdot P\left(n_{\rm sel}\right) \tag{7.6}$$

where: $P(n_{\rm sel})$ and $P(n_{\rm ch})$ are probabilities of observing $n_{\rm sel}$ and $n_{\rm ch}$ independently, $P(n_{\rm ch}|n_{\rm sel})$ and $P(n_{\rm sel}|n_{\rm ch})$ are conditional probabilities.
The main idea behind this procedure is that the unfolding is done iteratively to improve the estimate of $P(n_{\rm ch}|n_{\rm sel})$:

- In the first iteration, it is assumed that:

$$P(n_{\rm ch}|n_{\rm sel}) = P = P(n_{\rm sel}|n_{\rm ch})\frac{P^{\rm MC}(n_{\rm ch})}{P^{\rm MC}(n_{\rm sel})} \tag{7.7}$$

$$N_{\rm ev}(n_{\rm ch}) = \frac{1}{\epsilon^m(n_{\rm ch})\epsilon^r(n_{\rm ch})} \sum_{n_{\rm sel}\geq 2} N_{\rm ev}(n_{\rm sel}) \cdot P \tag{7.8}$$

where $P(n_{\rm sel}|n_{\rm ch})$, $P^{\rm MC}(n_{\rm ch})$ and $P^{\rm MC}(n_{\rm sel})$ are obtained from MC. $P(n_{\rm sel}|n_{\rm ch})$ is the same for each iteration.

- In the $(i + 1)$th iteration we have:

$$P^{i+1} = P(n_{\rm sel}|n_{\rm ch})\frac{P^i(n_{\rm ch})}{P(n_{\rm sel})} \tag{7.9}$$

$$N_{\rm ev}^{i+1}(n_{\rm ch}) = \frac{1}{\epsilon^m(n_{\rm ch})\epsilon^r(n_{\rm ch})} \sum_{n_{\rm sel}\geq 2} N_{\rm ev}(n_{\rm sel}) \cdot P^{i+1} \tag{7.10}$$

where normalized to unity $N_{\rm ev}^i(n_{\rm ch})$, calculated in the previous iteration, and $N_{\rm ev}(n_{\rm sel})$, taken from data, serve as probability distributions $P^i(n_{\rm ch})$ and $P(n_{\rm sel})$.

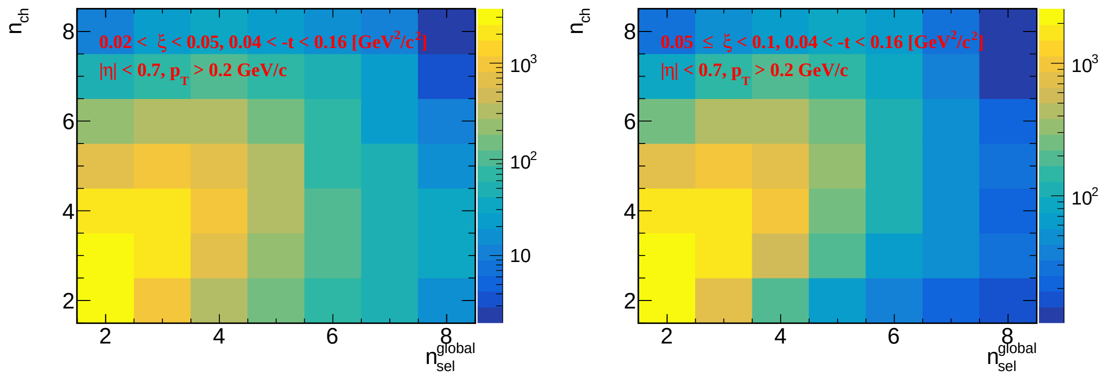

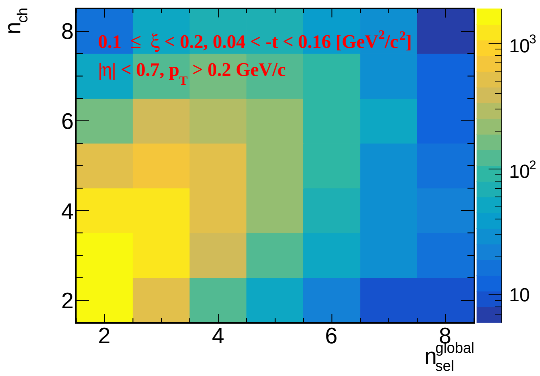

Figure 7.2: The unfolding matrices calculated from MC for three ranges of ξ separately.

The unfolding matrices $P(n_{\mathrm{ch}}|n_{\mathrm{sel}})$ for each ξ region, shown in Fig. 7.2, were obtained from MC and used in the first iteration of the above procedure.

The distribution dN/dn_{ch} obtained after the unfolding procedure was corrected for BBC-small efficiency, through $w_{\mathrm{BBC}}(n_{\mathrm{ch}})$ weights, and migrations of events between ξ ranges, through $f_\xi(n_{\mathrm{ch}})$ weights. Since the unfolding matrices contain track reconstruction efficiencies, non-primary track backgrounds, migrations of tracks into and out of the fiducial region, the weight $w_{\mathrm{trk}}\,(p_{\mathrm{T}}, \eta, V_z)$ was not used.

Finally, the dN/dn_{ch} distribution was normalized to the total number of events, $N_{\mathrm{ev}} = N$, which was calculated as the integral of the unfolded $N_{\mathrm{ev}}(n_{\mathrm{ch}})$ distribution.

7.2 Correction to Transverse Momentum and Pseudorapidity Distributions

First the accidental and non-SD backgrounds were subtrated from the p_{T} and $\bar{\eta}$ distributions. Next, the tracks were corrected for vertex reconstruction efficiency by applying $w_{\mathrm{ev}}^{\mathrm{vrt}}(n_{\mathrm{vrt}}^{\mathrm{global}}, |\Delta z_0|)$ weights. Then, the tracks were corrected for the track reconstruction efficiency, non-primary track background contribution, track and ξ migrations, BBC-small efficiency (the product of $w_{\mathrm{trk}}(p_{\mathrm{T}}, \eta, V_z)$, f_ξ and w_{BBC} weights was applied).

In order to obtain the charged particle multiplicity distributions, the p_{T} and $\bar{\eta}$ distributions were normalized to unity and scaled by the average charged particle multiplicity in an event $\langle n_{\mathrm{ch}} \rangle$. The latter was calculated from the corrected charged particle multiplicity distribution dN/dn_{ch} (Sec. 7.1).

In addition, the mean particle densities in an event, $\langle p_{\mathrm{T}} \rangle$ and $\langle \bar{\eta} \rangle$, were obtained from the measured distributions.

7.3 Particle Identification

The specific ionization energy loss, the dE/dx, is a function of magnitude of the particle momentum. However, at the midrapidity region of $|\eta| < 0.7$, p_{T} is approximately equal to $|p|$. In this section the particle identification by the dE/dx at low p_{T} is described. The particle identification at high p_{T} is possible by the TOF, but due to the low particle multiplicity and lack of signal in VPDs on the outgoing proton side (presence of the rapidity gap) in SD events, the time of collision is not defined precisely enough. Therefore, the analysis was limited to identification only by dE/dx.

The ionization energy loss of charged particles in material is given by the Bethe-Bloch formula and for the Solenoidal Tracker at RHIC (STAR) TPC by the more precise Bichsel formula [11]. The particle type can be determined by comparison of particle's dE/dx with the Bethe-Bloch (Bichsel) expectations. Figure 7.3 shows the dE/dx versus rigidity $q \times p$ for particles in $|\eta| < 0.7$. Various particles are separated at low $|q \times p|$, whereas at higher $|q \times p|$ the dE/dx of different particle species starts to overlap: $e^{\pm}$ and $K^{\pm}$ merge at $\sim$ 0.4 GeV/c, $K^{\pm}$ and $\pi^{\pm}$ merge at $\sim$ 0.7 GeV/c, and $p(\bar{p})$ and $\pi^{\pm}$ merge at $\sim$ 1 GeV/c. Since the dE/dx distribution for a fixed

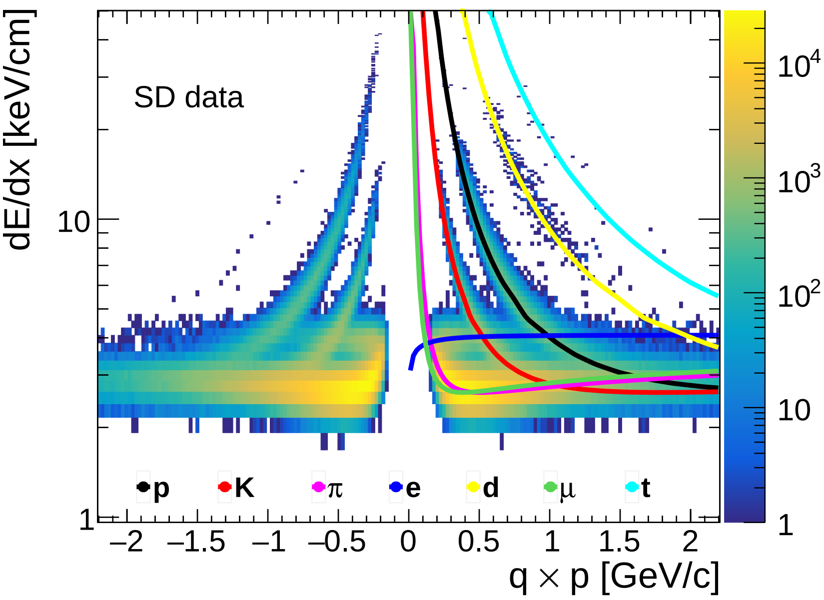

Figure 7.3: Specific ionization energy loss dE/dx as a function of rigidity $q \times p$ for particles in $|\eta| < 0.7$. The Bichsel predictions for each particle species are also shown.

particle type is not Gaussian, the following variable for each particle type was defined:

$$n\sigma^{i}_{dE/dx} = \ln\left(\frac{dE/dx}{(dE/dx)^{\mathrm{BB}}_{i}}\right)/\sigma \tag{7.11}$$

where $(dE/dx)^{\mathrm{BB}}_{i}$ is the Bethe-Bloch (Bichsel) expectation of dE/dx for the given particle type i ($i = \pi, K, p$), σ - the dE/dx resolution. The expected value of $n\sigma^{i}_{dE/dx}$ for the particle under consideration is around 0 and the width equals to 1. The sample $n\sigma^{i}_{dE/dx}$ distribution for $\pi^{\pm}$, $K^{\pm}$ and $p(\bar{p})$ in one ξ range, $0.02 < \xi < 0.05$, is shown in Fig. ??.
Figure 7.5 shows the $n\sigma^{\pi^{\pm}}_{dE/dx}$,$n\sigma^{K^{\pm}}_{dE/dx}$ and $n\sigma^{p(\bar{p})}_{dE/dx}$ distributions for a single p_{T} bin in the single ξ range, $0.02 < \xi < 0.05$, each corrected for the energy loss (mass of i-particle was assumed) [1] and vertexing (other p_{T} bins are shown in Appendix C). To extract the particle yield for a given particle type, a multi-Gaussian fit is applied to the $n\sigma^{i}_{dE/dx}$ distribution in each p_{T} bin and ξ

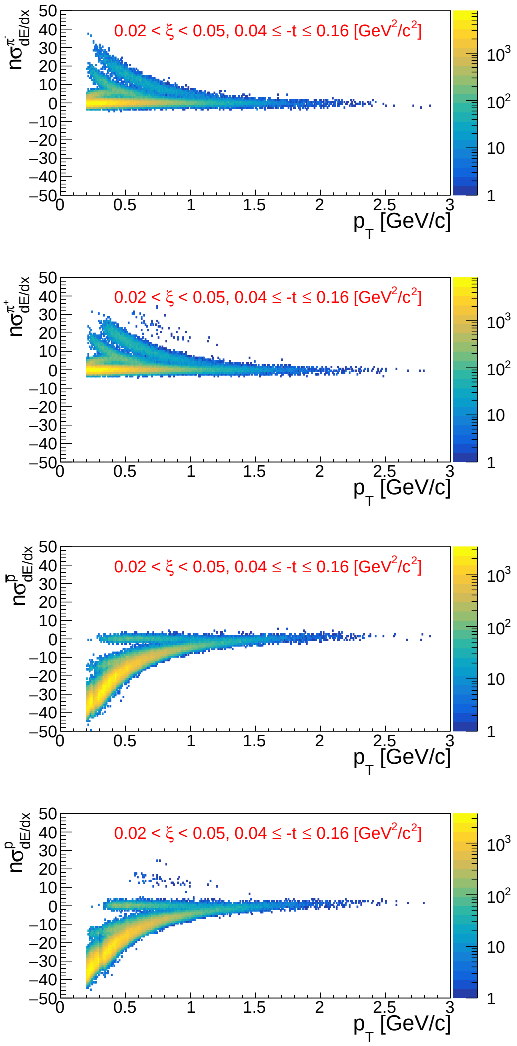

The $n\sigma^{i}_{dE/dx}$ variable for particle $i^{\pm}$ versus p_{T}. Particles are restricted in $|\eta| < 0.7$ and corrected for the energy loss (mass of $i^{\pm}$-particle was taken) [1] and vertexing.

range. The parameters of the multi-Gaussian fit are the centroids μ_{i^-/i^+}, widths σ_{i^-/i^+}, sum and ratios of amplitudes C_{i^-/i^+}, r_{i^-/i^+} for negative i^- and positive i^+ particles ($\pi^{\pm}$, $e^{\pm}$, $K^{\pm}$, p and $\bar{p}$). The positive and negative particle $n\sigma^{i}_{dE/dx}$-distributions are fit simultaneously, where the particle and antiparticle centroids and widths are kept the same. Additionally, multiple steps of fitting in the first ξ range are performed to reduce the number of free parameters in the final fit, where almost all centroids and widths are constrained by an arbitrary function with free parameters p_k, where $k \in \mathbb{N}$. The values of these parameters, obtained for events with $0.02 < \xi < 0.05$ are kept the same for other ξ ranges. Also electron contributions are fixed, but separately for each ξ range. The procedure slightly differs for different particle types:

1. $\pi^{\pm}$:
    - Step 1 (Fig. 7.6):
        - Analyze data with $0.2 < p_{\mathrm{T}} < 0.65$ GeV/c
        - Fit μ_{π^-/π^+} and σ_{π^-/π^+} as a function of p_{T} with a polynomial $p_0 p_{\mathrm{T}}^3 + p_1 p_{\mathrm{T}}^2 + p_2 p_{\mathrm{T}} + p_3$
        - Fit r_{e^-/e^+} as a function of p_{T} with a polynomial $p_0 p_{\mathrm{T}}^2 + p_1 p_{\mathrm{T}} + p_2$
        - Fit C_{e^-/e^+}, μ_{K^-/K^+} as a functions of p_{T} with $p_0 \exp(p_1 p_{\mathrm{T}}) + p_2$
        - Fit μ_{e^-/e^+} as a function of p_{T} with $p_0 \exp\left[-\left(p_1 p_{\mathrm{T}}\right)^{p_2}\right]$

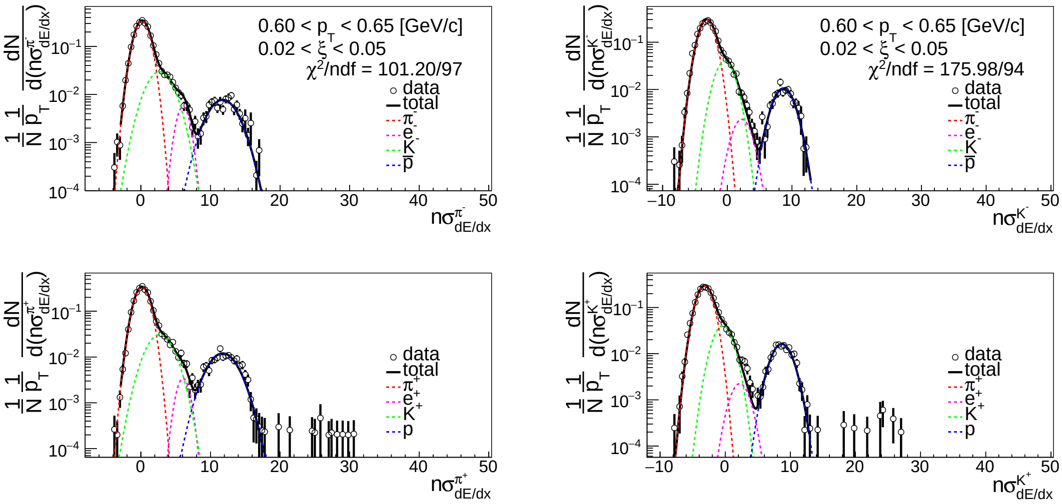

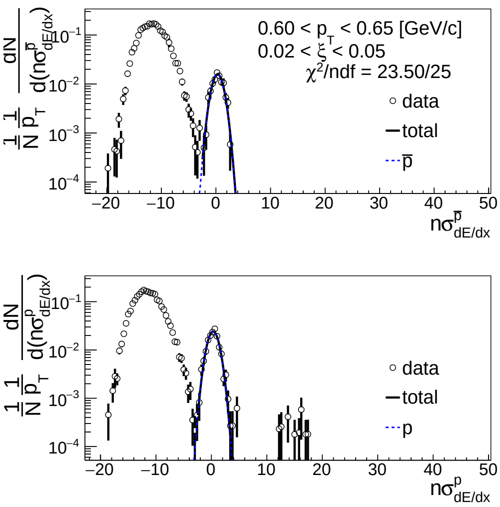

Figure 7.5: Distributions of (top left) $n\sigma^{\pi^{\pm}}_{dE/dx}$ for $\pi^{\pm}$, (top right) $n\sigma^{K^{\pm}}_{dE/dx}$ for $K^{\pm}$ and (bottom left) $n\sigma^{\bar{p}/p}_{dE/dx}$ for $\bar{p}/p$ in sample p_{T} bin and sample ξ range shown for each particle species. Particles are corrected for energy loss [1] and vertexing. The curves represent the Gaussian fits to the $n\sigma^{i}_{dE/dx}$ distributions.

  - Fit σ_{K^-/K^+} as a function of p_{T}, where $0.3 < p_{\mathrm{T}} < 0.5$ GeV/c, with constant p_0
  - Fit $\mu_{\bar{p}/p}$ and $\sigma_{\bar{p}/p}$ as a function of p_{T} with $p_0 \exp(p_1 p_{\mathrm{T}})$
- Step 2:
  - σ_{e^-/e^+} fixed to 1.2 and 0.8 for $0.2 < p_{\mathrm{T}} < 0.4$ and $0.4 < p_{\mathrm{T}} < 0.7$, respectively
  - σ_{K^-/K^+} parametrized for $0.3 < p_{\mathrm{T}} < 0.7$
  - The rest parameters from Step 1 are fixed with obtained parametrization: μ_{π^-/π^+}, σ_{π^-/π^+}, , r_{e^-/e^+}, C_{e^-/e^+}, μ_{e^-/e^+} , μ_{K^-/K^+}, $\mu_{\bar{p}/p}$, $\sigma_{\bar{p}/p}$

2. $K^{\pm}$:

- Step 1 (Fig. 7.8):
  - Analyze data with $0.2 < p_{\mathrm{T}} < 0.6$ GeV/c
  - Fit μ_{π^-/π^+} as a function of p_{T} with $-\exp(p_0 + p_1 p_{\mathrm{T}})$
  - Fit σ_{π^-/π^+}, C_{e^-/e^+}, σ_{e^-/e^+}, σ_{K^-/K^+} as a function of p_{T} with $\exp(p_0 + p_1 p_{\mathrm{T}})$
  - Fit r_{e^-/e^+} as a function of p_{T} with constant p_0
  - Fit μ_{e^-/e^+} as a function of p_{T} with a polynomial $p_0 p_{\mathrm{T}}^3 + p_1 p_{\mathrm{T}}^2 + p_2 p_{\mathrm{T}} + p_3$
  - Fit μ_{K^-/K^+} as a function of p_{T} with a polynomial $p_0 + p_1 p_{\mathrm{T}}^2$

- Step 2:
  - All parameters from Step 1 except σ_{e^-/e^+} are fixed with obtained parametrization.
  - Fit σ_{e^-/e^+} as a function of p_{T}, where $0.45 < p_{\mathrm{T}} < 0.65$ GeV/c, with constant p_0
- Step 3:
  - σ_{e^-/e^+} fixed with obtained parametrization from Steps 1 and 2 for $0.3 < p_{\mathrm{T}} < 0.45$ and $0.45 < p_{\mathrm{T}} < 0.65$, respectively.
  - The rest parameters from Step 1 are fixed with obtained parametrization: μ_{π^-/π^+}, σ_{π^-/π^+}, , r_{e^-/e^+}, C_{e^-/e^+}, μ_{e^-/e^+} , μ_{K^-/K^+},σ_{K^-/K^+}

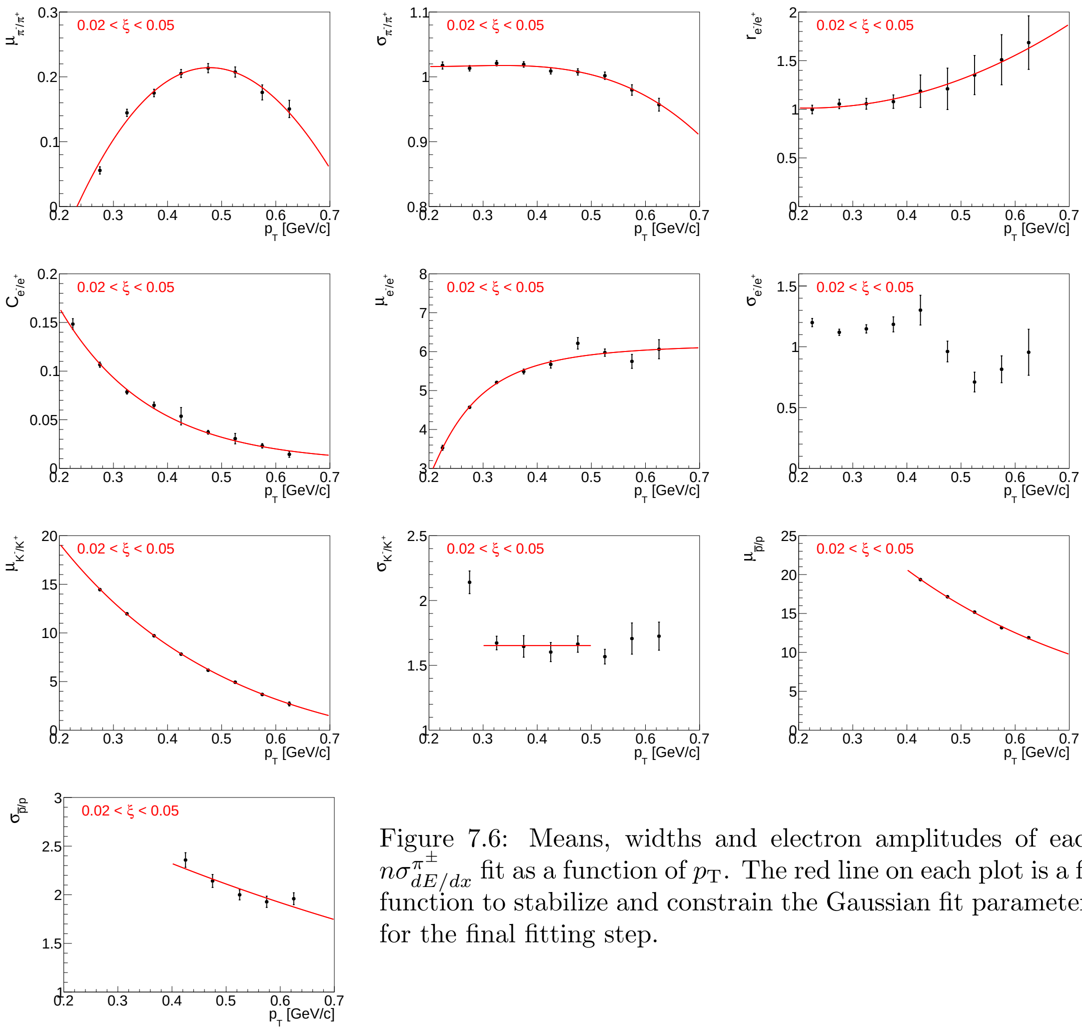

Figure 7.6: Means, widths and electron amplitudes of each $n\sigma^{\pi^\pm}_{dE/dx}$ fit as a function of p_{T}. The red line on each plot is a fit function to stabilize and constrain the Gaussian fit parameters for the final fitting step.

3. $\bar{p}, p$:
   - Step 1 (Fig. 7.7):
     - Analyze data with $0.4 < p_{\mathrm{T}} < 0.9$ GeV/c
     - Fit μ_{π^-/π^+}, μ_{K^-/K^+} as a function of p_{T} with a polynomial $p_0 p_{\mathrm{T}} + p_1$
     - Fit σ_{π^-/π^+} as a function of p_{T} with a polynomial $p_0 p_{\mathrm{T}}^2 + p_1 p_{\mathrm{T}} + p_2$
     - Fit σ_{K^-/K^+} as a function of p_{T} with $\exp(p_0 + p_1 p_{\mathrm{T}})$
   - Step 2:

– μ_{K^-/K^+} fixed with obtained parametrization from Step 1
– All the rest parameters from Step 1 are limited with obtained parametrization
– Fit μ_{π^-/π^+}, σ_{π^-/π^+}, σ_{K^-/K^+} as a function of p_T with a polynomial $p_0 p_\mathrm{T}^2 + p_1 p_\mathrm{T} + p_2$
– Fit $\mu_{\bar{p}/p}$ as a function of p_T, where $0.7 < p_\mathrm{T} < 1.0$ GeV/c, with constant p_0

- Step 3:
  – μ_{K^-/K^+} fixed with obtained parametrization from Step 1
  – $\mu_{\bar{p}/p}$ fixed with obtained parametrization from Step 2 for $0.7 < p_\mathrm{T} < 1.0$
  – The rest parameters from Step 2 are fixed with obtained parametrization: μ_{π^-/π^+}, σ_{π^-/π^+}, σ_{K^-/K^+}

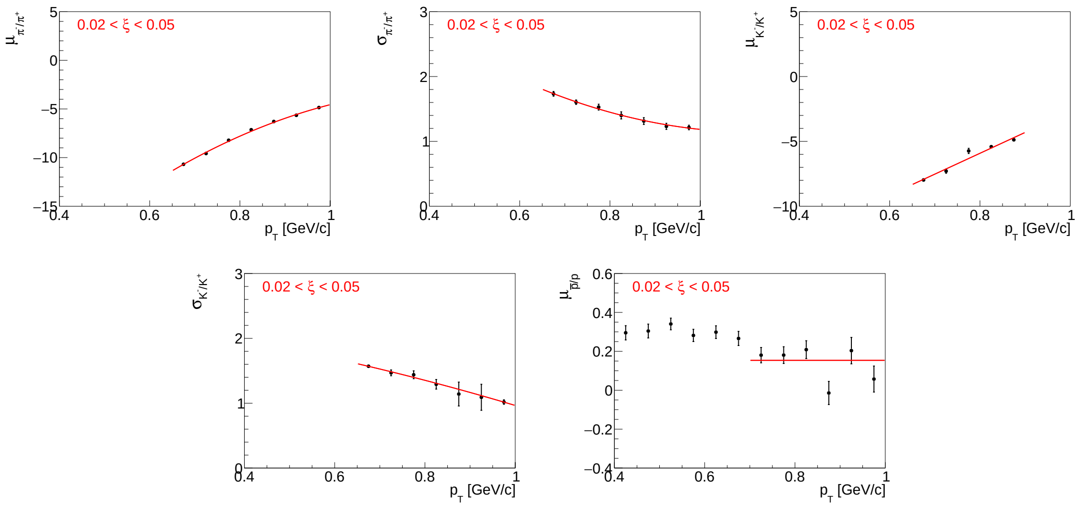

Figure 7.7: Means and widths of each $n\sigma^{\bar{p}/p}_{dE/dx}$ fit as a function of p_T. The red line on each plot is a fit function to stabilize and constrain the Gaussian fit parameters for the final fitting step.

The particle yield is extracted from the fit to the corresponding $n\sigma^{i}_{dE/dx}$ distribution (corrected only for the energy loss [1] and vertexing). As shown in Fig. **??**, the dE/dx of each particle type merge at large p_T. Hence, the particle identification is limited. Pions can be identified in the momentum range of $0.2 - 0.7$ GeV/c, kaons in $0.3 - 0.65$ GeV/c and (anti)protons in $0.4 - 1.0$ GeV/c.

7.4 Antiparticle-to-Particle Ratios

The following steps were taken to correct an identified antiparticle to particle (pion, kaon, proton and their antiparticle) multiplicity ratios as a function of p_T in three ranges of ξ:

- The raw identified particle yields were obtained through multi-Gaussian fits to the $n\sigma^{i}_{dE/dx}$ distributions (Sec. 7.3), where the vertex reconstruction and energy loss corrections [1] were applied. The latter depends on the particle type.
- The accidental and non-SD backgrounds were subtracted. It was assumed that the former does not depend on the particle type, i.e. the same contribution of accidental background was used as for charged particles without identification (Sec. 4.1).
- The particle yields were corrected for track reconstruction efficiencies [1], which depend on the particle type and charge.

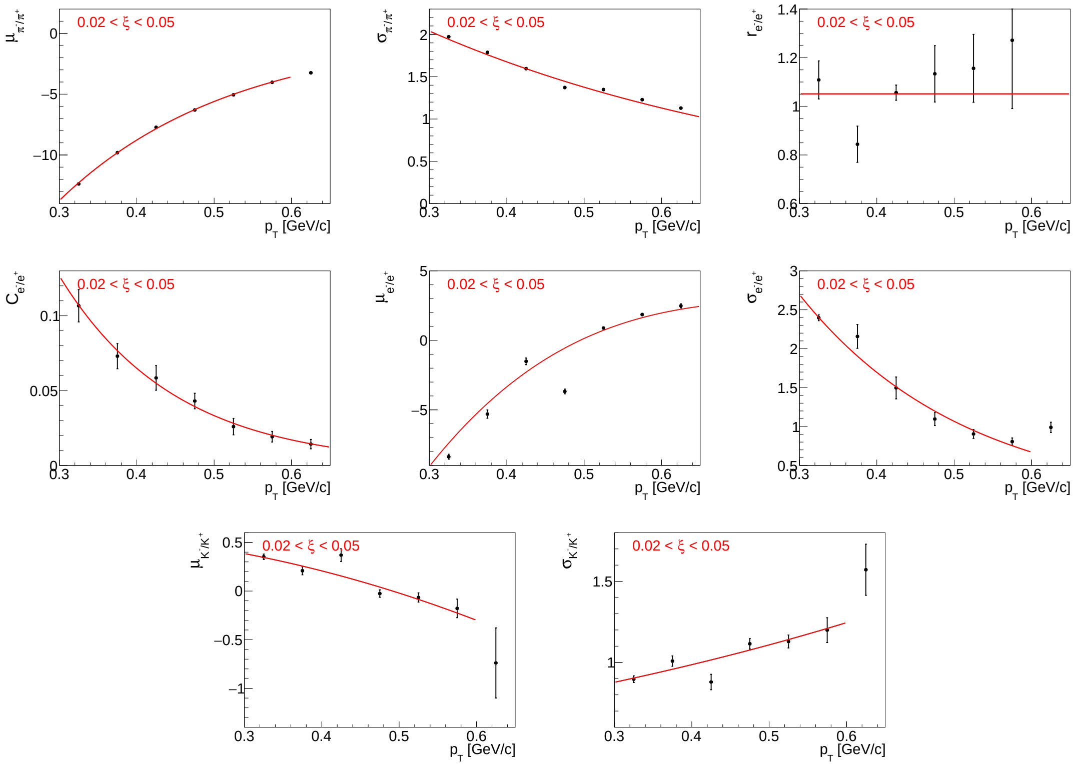

Figure 7.8: Means, widths and electron amplitudes of each $n\sigma^{K^{\pm}}_{dE/dx}$ fit as a function of p_{T}. The red line on each plot is a fit function to stabilize and constrain the Gaussian fit parameters for the final fitting step.

- The background from non-primary tracks was subtracted (Sec. 4.3):
  - $\pi^{\pm}$: weak decays pions, muon contribution and background from detector dead-material interactions,
  - p: background from detector dead-material interactions,
  - $p, \bar{p}$: reconstructed tracks which have the appropriate number of common hit points with true-level particle, but the distance between them is too large (this background is negligibly small for other particle types),
  - all: fake track contribution, the same for each particle type.
- Then the tracks were corrected for track and ξ migrations, and BBC-small efficiency, which do not depend on the particle type and charge.
- Finally, each antiparticle p_{T} distribution was divided by the corresponding particle p_{T} distribution to obtain fully corrected identified antiparticle to particle multiplicity ratios.
- Additionally, the average antiparticle to particle ratios in each ξ region were calculated.

8. Systematic Uncertainties

Apart from the statistical uncertainties there are also systematic uncertainties originating from inefficiencies and limitations of the measurement devices and techniques. Systematic uncertainties are obtained by using modified input distributions and calculating the difference between standard and changed settings for each bin of the distribution. The systematic uncertainties on $1/N\ dN/dn_{\mathrm{ch}}$ are propagated by randomly removing and adding tracks in the n_{sel} distribution before unfolding procedure.

The following sources of systematic uncertainties were considered:

- the effect of off-time pile-up on TPC track reconstruction efficiency [1],
- the uncertainty of TPC track reconstruction efficiency related to the description of dead-material in simulation [1],
- representation of data sample in embedding MC [1],
- fake track background contribution (Sec. 4.3),
- TOF system simulation accuracy [1],
- accidental background contribution (Sec. 4.1),
- the effect of alternative model of hadronisation on BBC-small efficiency (Sec. 5.2),
- non-SD background contribution (Sec. 4.2),
- non-closure: full correction procedure was applied to the MC detector-level distributions. The difference between true-level and corrected distributions was taken as a systematic uncertainties. Due to the method of factorization of the global efficiency into the product of single-particle efficiencies, a level of non-closure below 5% is typically considered to be sufficient for the validation of the procedure.
- non-closure of N_{ev}, applied only to p_{T} and $\bar{\eta}$ distributions,
- the $1/N_{\mathrm{ev}}\ dN/d\bar{\eta}$ distribution was calculated separately for events in which forward proton is on one and the other side of the IP (east-west).

Figures 8.1 to 8.3 show the components contributing to the total systematic uncertainty for charged particle distributions without the identification. The dominant systematic uncertainty for p_{T} and n_{ch} distributions is related to TOF system simulation accuracy. It affects mainly low-p_{T} particles, where it is about 6%, and large charged particle multiplicities, where it varies up to 25% for $n_{\mathrm{ch}} = 8$ and $0.02 < \xi < 0.05$. In case of $\bar{\eta}$ distribution, the systematic uncertainty on TOF mainly refers to charged particles produced at the edge of the fiducial region, for which it is about 2%. However, the largest (up to 6%) systematic uncertainty for $\bar{\eta}$, is related to the observed diffrence in the distributions calculated separately with respect to the forward proton direction. The rest of the components have smaller contributions to the total systematic uncertainty. The systematic uncertainty on non-closure is at the level of 2% which proves the accuracy of the correction procedure.

Figures 8.4 to 8.7 show breakdown of all different systematics for the antiparticle-to-particle multiplicity ratio distributions. An additional systematic contribution for $\bar{p}/p$ multiplicity ratio due to proton background estimation was introduced. Since most of the corrections are the same for particle and its antiparticle, nearly all systematic uncertainties cancel out in the antiparticle-to-particle ratios. The largest sources of systematics, which do not, are related to proton background estimation and dead-material effect on TPC track reconstruction efficiency. The former was found to be up to 5%, whereas the latter varies up to 2% for low-p_{T} $\bar{p}/p$ multiplicity ratio.

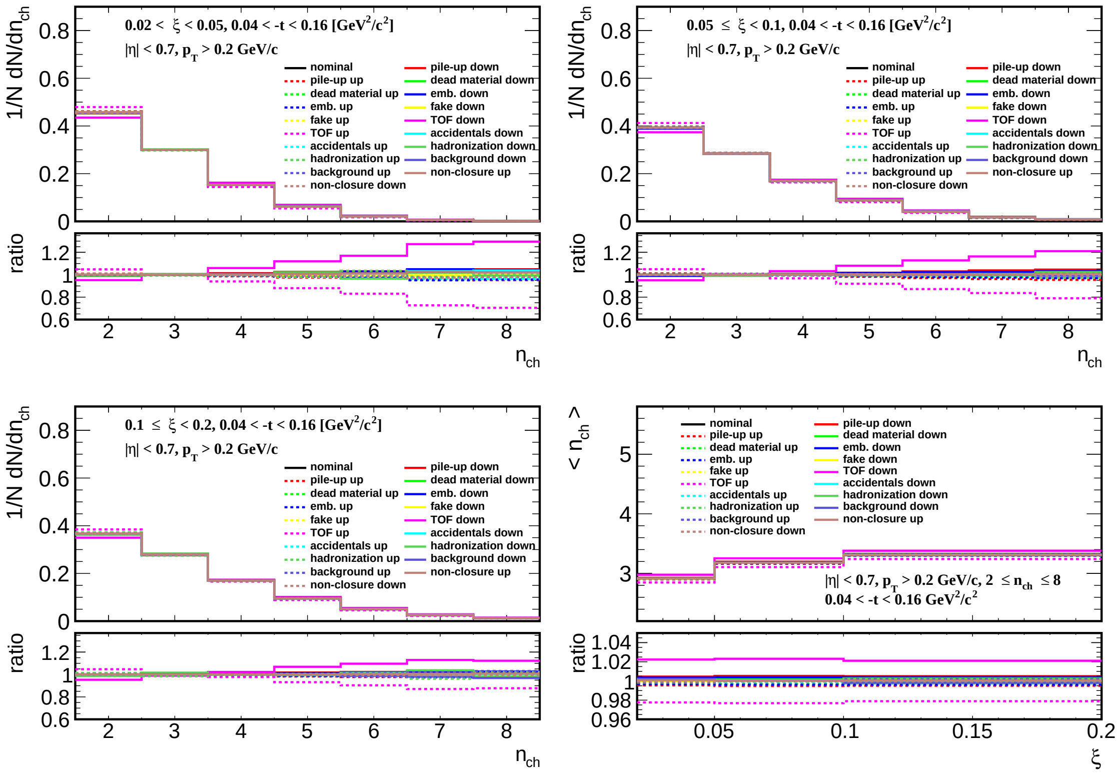

Figure 8.1: Components of the systematic uncertainties for the charged particle multiplicity in three ξ regions and for the average charged particle multiplicity.

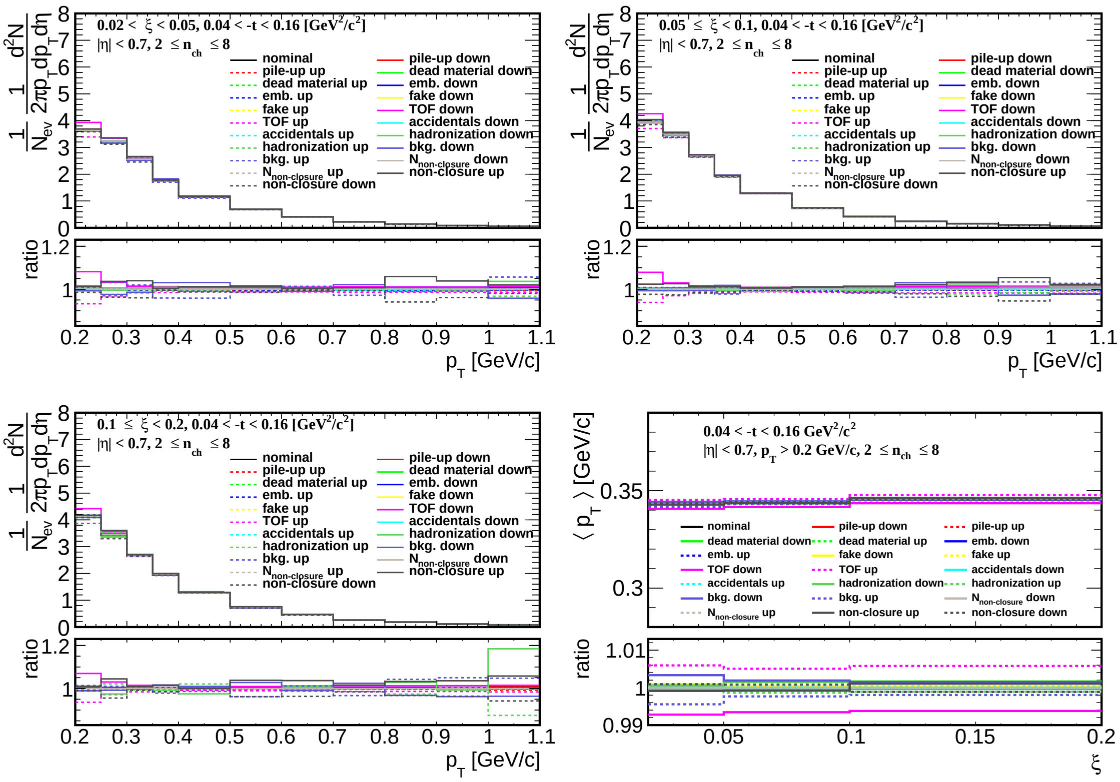

Figure 8.2: Components of the systematic uncertainties for p_{T} distributions in three ξ regions and for an average p_{T} distribution.

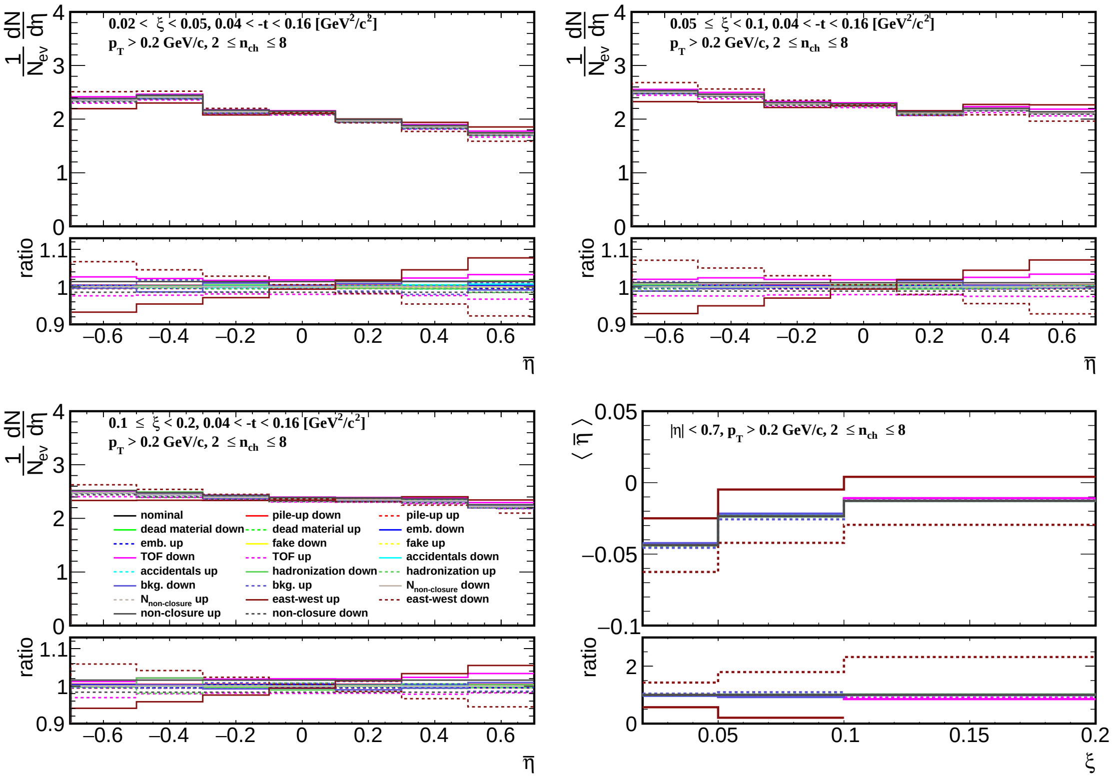

Figure 8.3: Components of the systematic uncertainties for $\bar{\eta}$ distributions in three ξ regions and for an average $\bar{\eta}$ distribution.

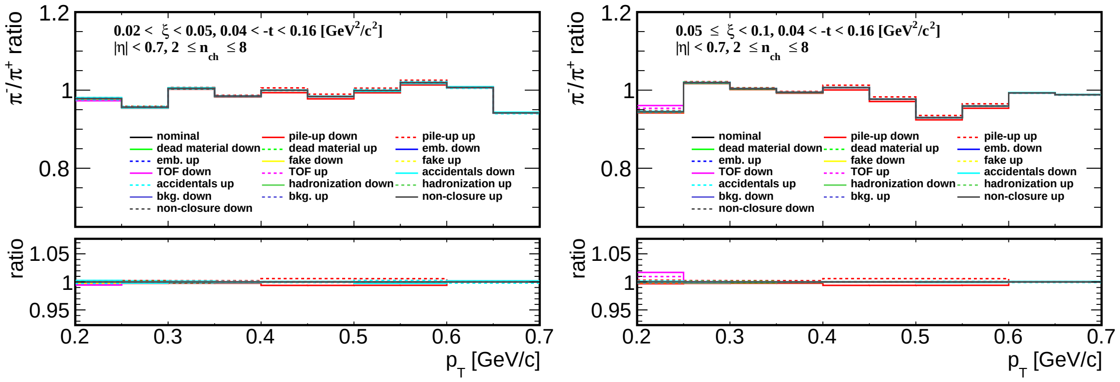

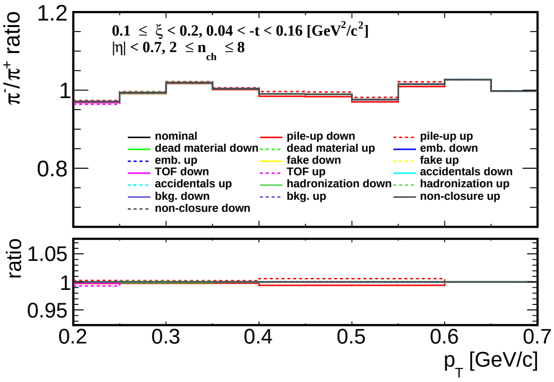

Figure 8.4: Components of the systematic uncertainties of π^-/π^+ multiplicity ratios in three ξ regions.

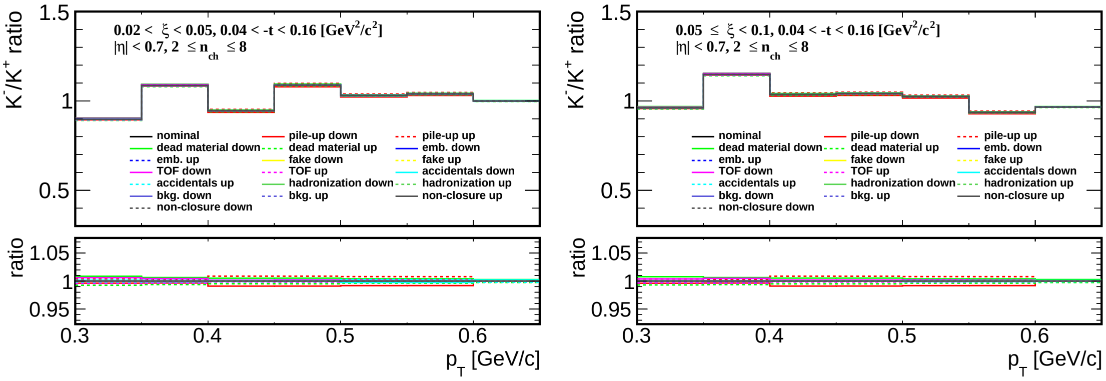

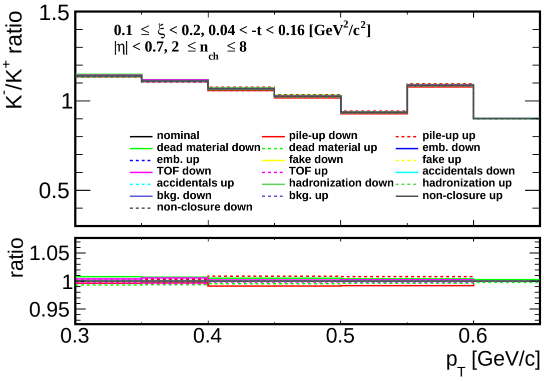

Figure 8.5: Components of the systematic uncertainties of K^-/K^+ multiplicity ratios in three ξ regions.

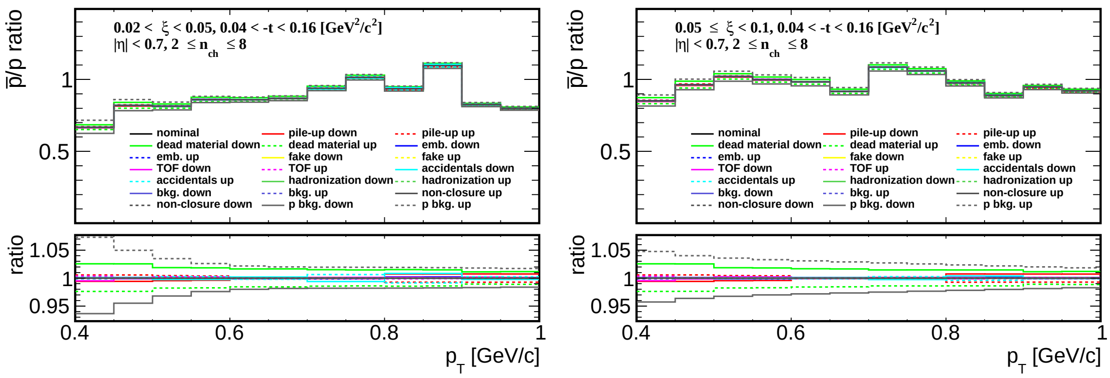

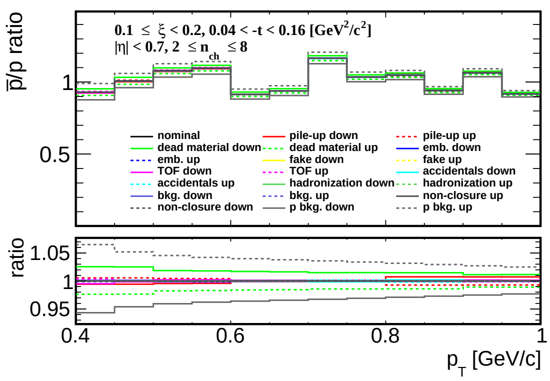

Figure 8.6: Components of the systematic uncertainties of $\bar{p}/p$ multiplicity ratios in three ξ regions.

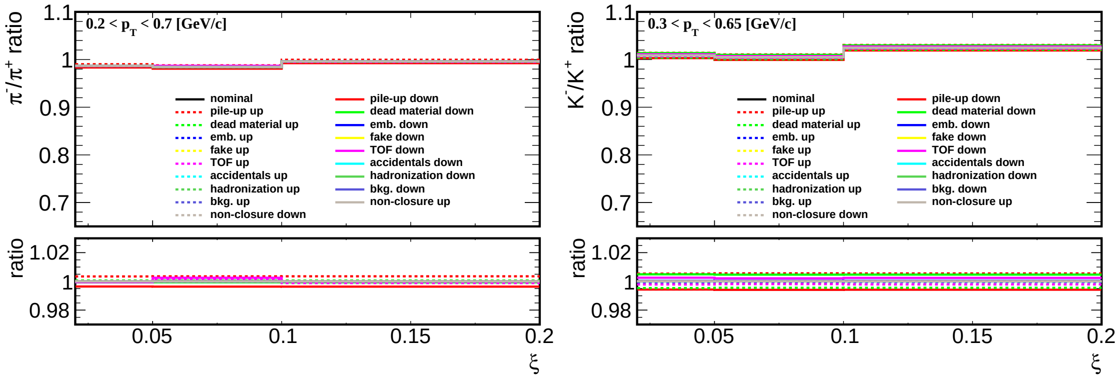

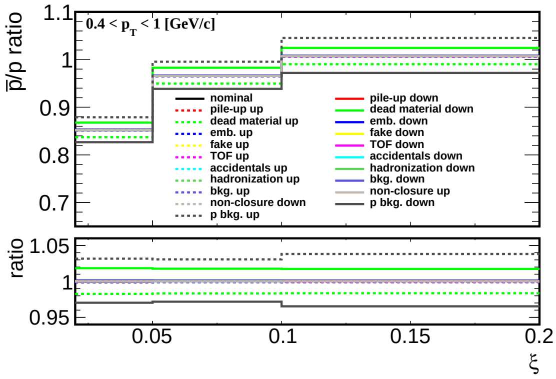

Figure 8.7: Components of the systematic uncertainties of average antiparticle-to-particle multiplicity ratios in three ξ regions.

9. Results

In the following section, the final-state charged particle distributions are compared with various SD MC predictions, i.e.

- PYTHIA 8 4C (SaS),
- PYTHIA 8 A2 (MBR),
- PYTHIA 8 A2 (MBR-tuned): expectations obtained without arbitrary suppression of diffractive cross sections at relatively large ξ,
- HERWIG 7,
- EPOS LHC with combined two classes of processes: diffractive (EPOS-SD) modelled by Pomeron exchange and non-diffractive modelled by low mass excitation of the proton remnant (EPOS-SD′).

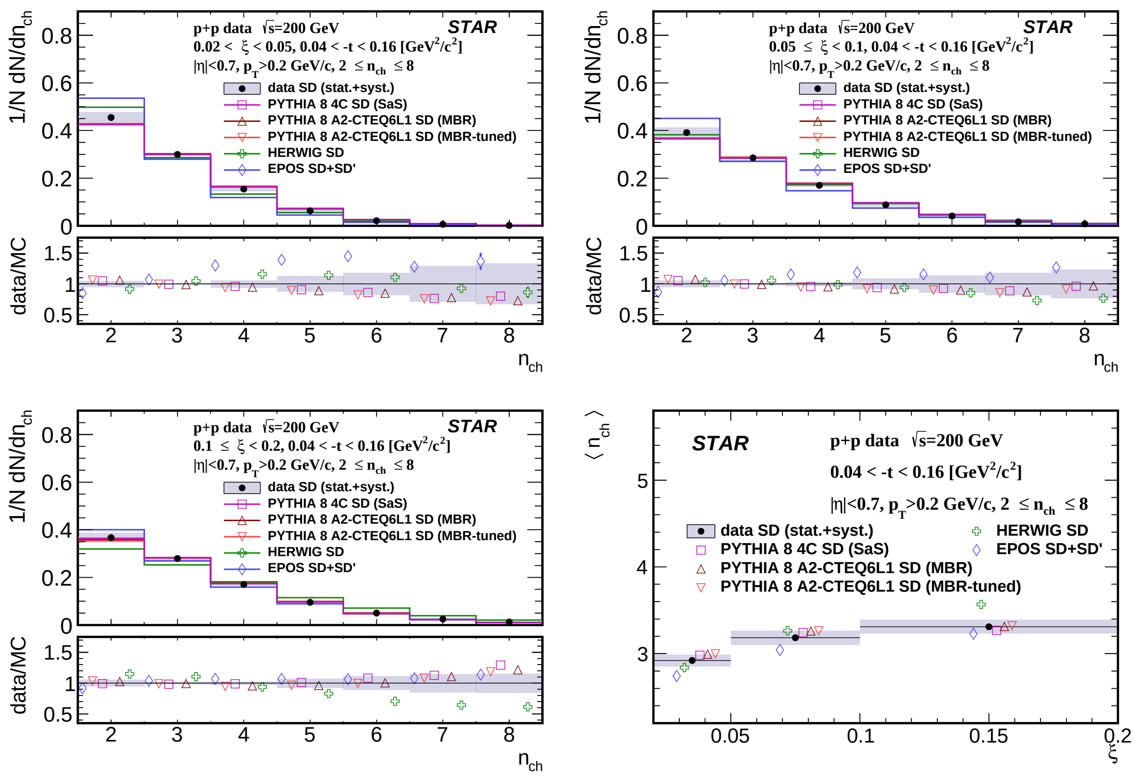

Figure 9.1: Primary charged-particle multiplicity shown separately for the three ranges of ξ: (top left) $0.02 < \xi < 0.05$, (top right) $0.05 < \xi < 0.1$, (bottom left) $0.1 < \xi < 0.2$ and (bottom right) the mean multiplicity $\langle n_{\mathrm{ch}} \rangle$ as a function of ξ.

In all figures, data are shown as solid points with error bars representing the statistical uncertainties. Gray boxes represent statistical and systematic uncertainties added in quadrature. Predictions from MC models are shown as colour histograms and markers. The lower panel in each figure shows the ratio of data to the models' predictions. All results are presented separately for three ranges of ξ: $0.02 < \xi < 0.05$, $0.05 < \xi < 0.1$, $0.1 < \xi < 0.2$.

Figure 9.1 shows primary charged-particle multiplicity separately for the three ranges of ξ and the mean multiplicity $\langle n_{\mathrm{ch}} \rangle$ as a function of ξ. Data follow the expected increase of $\langle n_{\mathrm{ch}} \rangle$ with ξ due to the larger diffractive masses probed by increasing ξ in SD process. The shapes of the measured distributions are reproduced reasonably well by all models except EPOS SD+SD$'$ which predicts smaller $\langle n_{\mathrm{ch}} \rangle$ for $0.02 < \xi < 0.1$ and HERWIG-SD which for $0.1 < \xi < 0.2$ predicts too large $\langle n_{\mathrm{ch}} \rangle$.

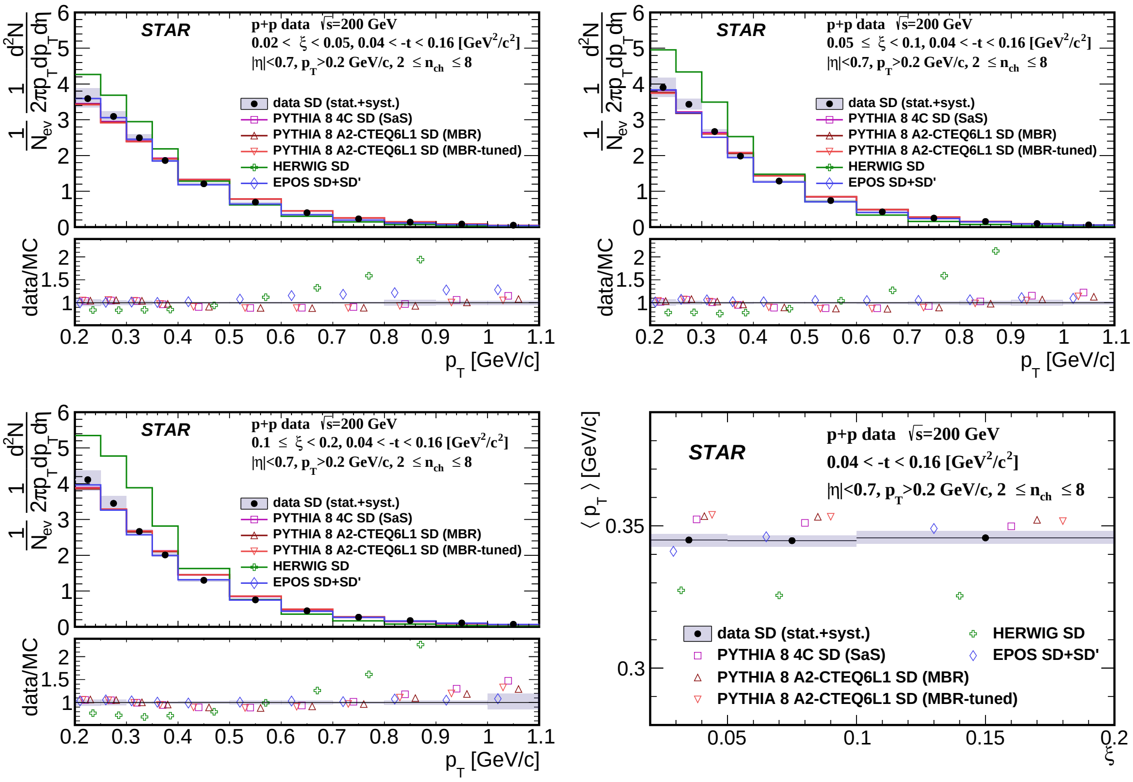

Figure 9.2: Primary charged-particle multiplicities as a function of p_{T} shown separately for the three ranges of ξ: (top left) $0.02 < \xi < 0.05$, (top right) $0.05 < \xi < 0.1$, (bottom left) $0.1 < \xi < 0.2$ and (bottom right) the mean transverse momentum $\langle p_{\mathrm{T}} \rangle$ as a function of ξ.

Figure 9.2 shows primary charged-particle multiplicities as a function of p_{T} separately for the three ranges of ξ and the mean transverse momentum $\langle p_{\mathrm{T}} \rangle$ as a function of ξ. Data show that $\langle p_{\mathrm{T}} \rangle$ depends very weakly on ξ. Models describe data fairly well except HERWIG-SD which predicts much steeper dependence of particle density with p_{T} in all three ξ ranges.

Figure 9.3 shows primary charged-particle multiplicity as a function of $\bar{\eta}$ (defined in Sec. **??**) separately for the three ranges of ξ and the mean pseudorapidity $\langle \bar{\eta} \rangle$ as a function of ξ. Data show expected flattening of the $\bar{\eta}$ distribution with increasing ξ which reflects SD event-asymmetry and fact that the gap-edge at large ξ is outside $|\bar{\eta}| < 0.7$ region leading to more flat distribution of particle density as a function of $\bar{\eta}$. Models describe data fairly well.

Figure 9.4 shows the ratio of production yields of π^-/π^+ as a function of p_{T} separately for the three ranges of ξ. Data in all three ξ ranges are consistent with equal amounts of π^+ and π^- with no significant p_{T} dependence. Models agree with data (except HERWIG) predicting on average small deviation from unity by $\sim 2\%$ what is smaller than data uncertainties. HERWIG in first two ξ ranges predicts too large asymmetry between π^+ and π^-.

Figure 9.5 shows the ratio of production yields of K^-/K^+ as a function of p_{T} separately for the three ranges of ξ . Data in all three ξ ranges are consistent with equal amounts of K^+ and K^- with no p_{T} dependence. Models agree with data except HERWIG in the first ξ range predicting

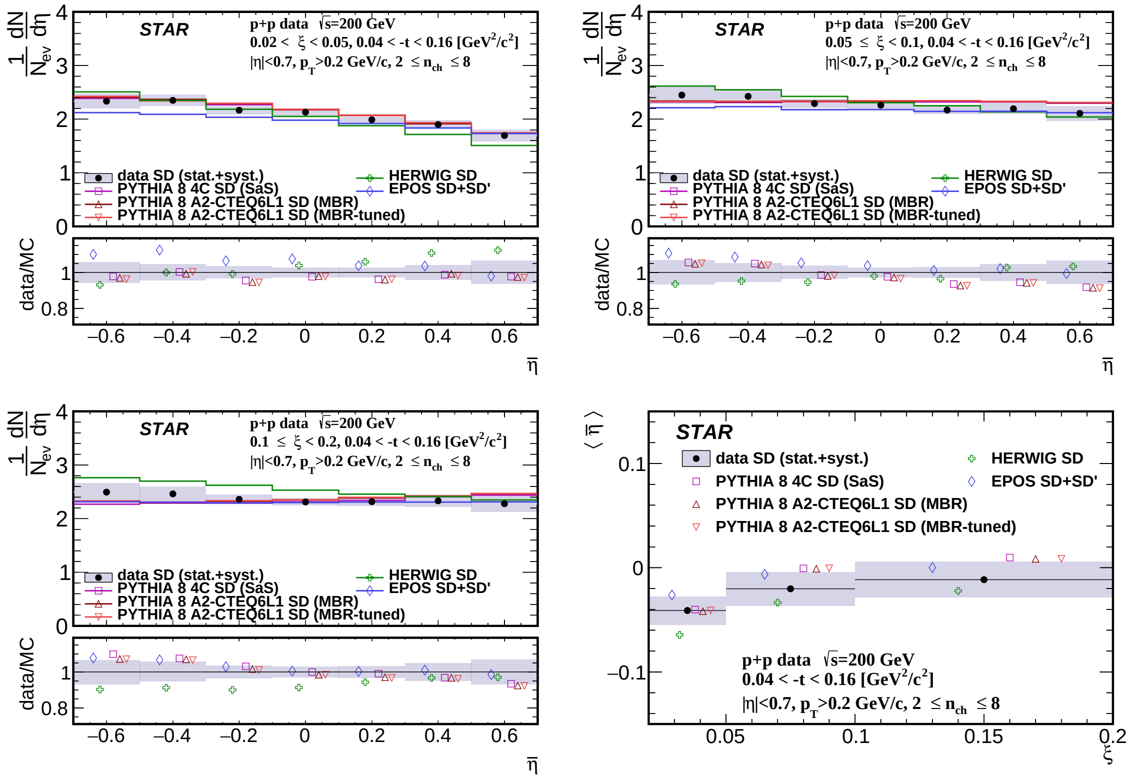

Figure 9.3: Primary charged-particle multiplicity as a function of $\bar{\eta}$ shown separately for the three ranges of ξ: (top left) $0.02 < \xi < 0.05$, (top right) $0.05 < \xi < 0.1$, (bottom left) $0.1 < \xi < 0.2$ and (bottom right) the mean pseudorapidity $\langle \bar{\eta} \rangle$ as a function of ξ.

too large ratio of K^- to K^+.

Figure 9.6 shows the ratio of production yields of $\bar{p}/p$ as a function of p_T separately for the three ranges of ξ. Data in the last two ξ ranges are consistent with equal amounts of p and $\bar{p}$ with no p_T dependence. However, in the first ξ range at $p_\mathrm{T} < 0.7$ GeV/c data shows significant deviation from unity indicating a significant transfer of the baryon number from the forward to the central region. PYTHIA8 and EPOS SD+SD′ agree with data in the last two ξ ranges. In first ξ range PYTHIA8 predicts small deviation from unity by $\sim 5\%$ which is smaller than observed in data, whereas EPOS SD+SD′ predicts an asymmetry between $\bar{p}$ and p of $\sim 30\%$ which is larger than observed in data except $p_\mathrm{T} < 0.5$ GeV/c. HERWIG predicts much larger baryon number transfer compared to data in first two ξ ranges and shows consistency with data in last ξ range.

Figure 9.7 shows mean ratio of production yields of π^-/π^+, K^-/K^+ and $\bar{p}/p$ as a function of ξ.

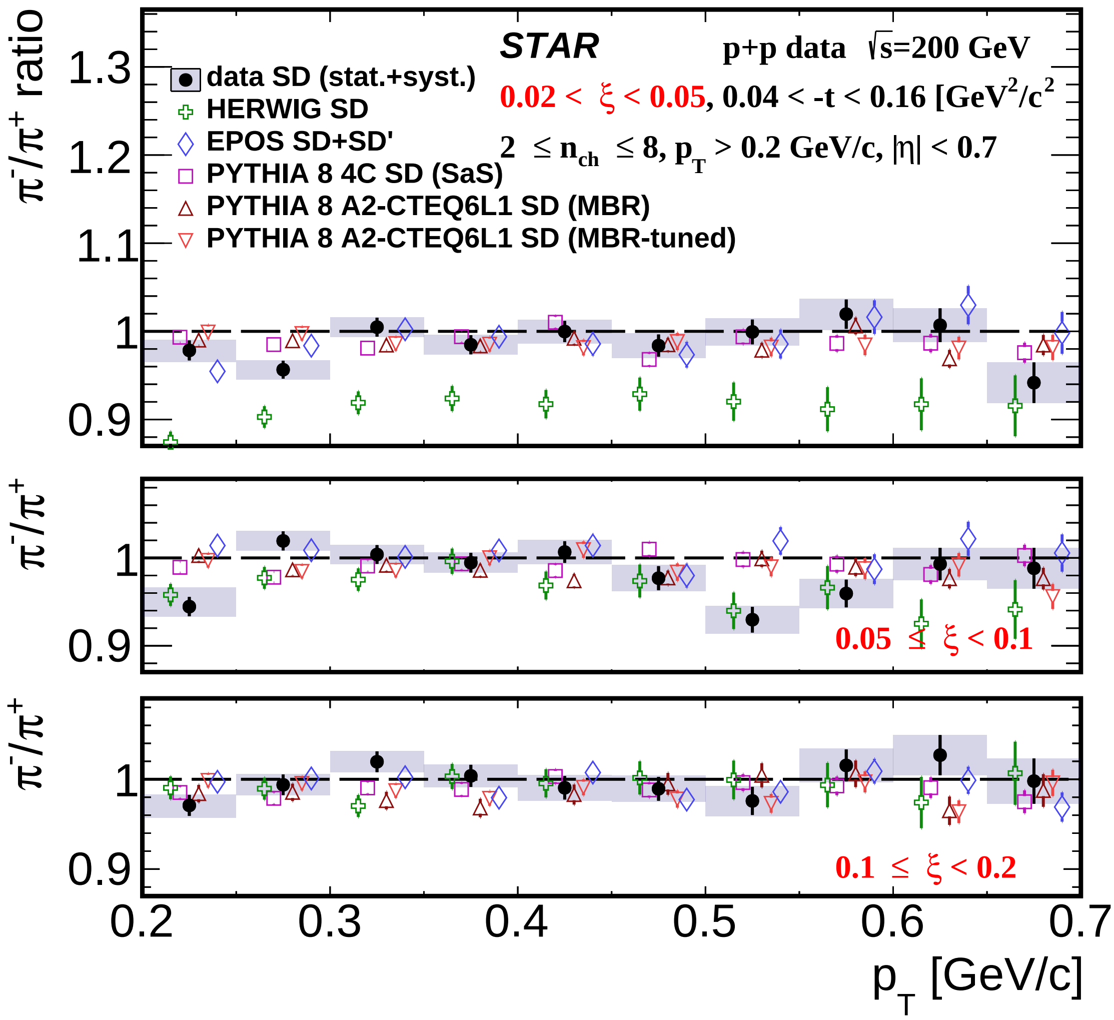

Figure 9.4: Ratio of production yields of π^-/π^+ as a function of p_T shown separately for the three ranges of ξ: (top) $0.02 < \xi < 0.05$, (middle) $0.05 < \xi < 0.1$, (bottom) $0.1 < \xi < 0.2$.

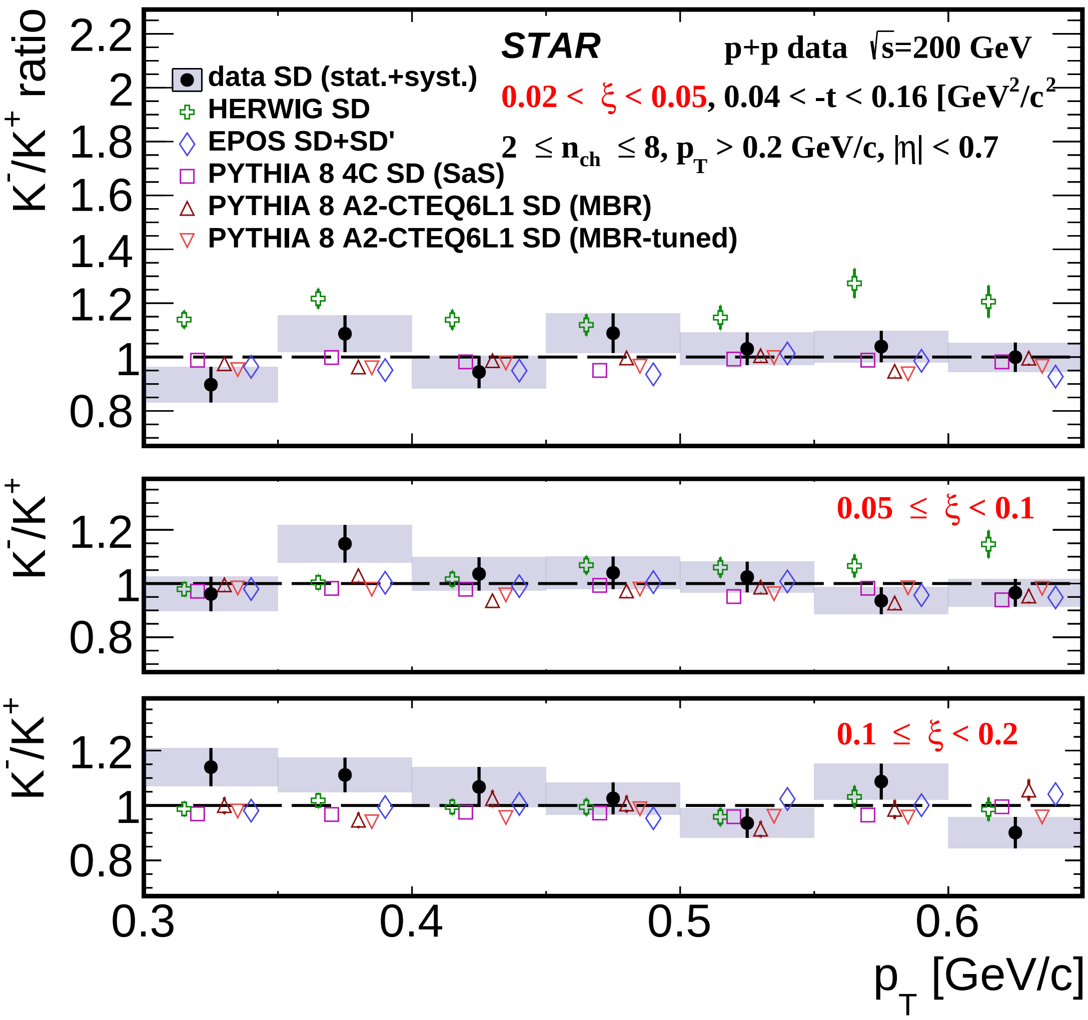

Figure 9.5: Ratio of production yields of K^-/K^+ as a function of p_T shown separately for the three ranges of ξ: (top) $0.02 < \xi < 0.05$, (middle) $0.05 < \xi < 0.1$, (bottom) $0.1 < \xi < 0.2$.

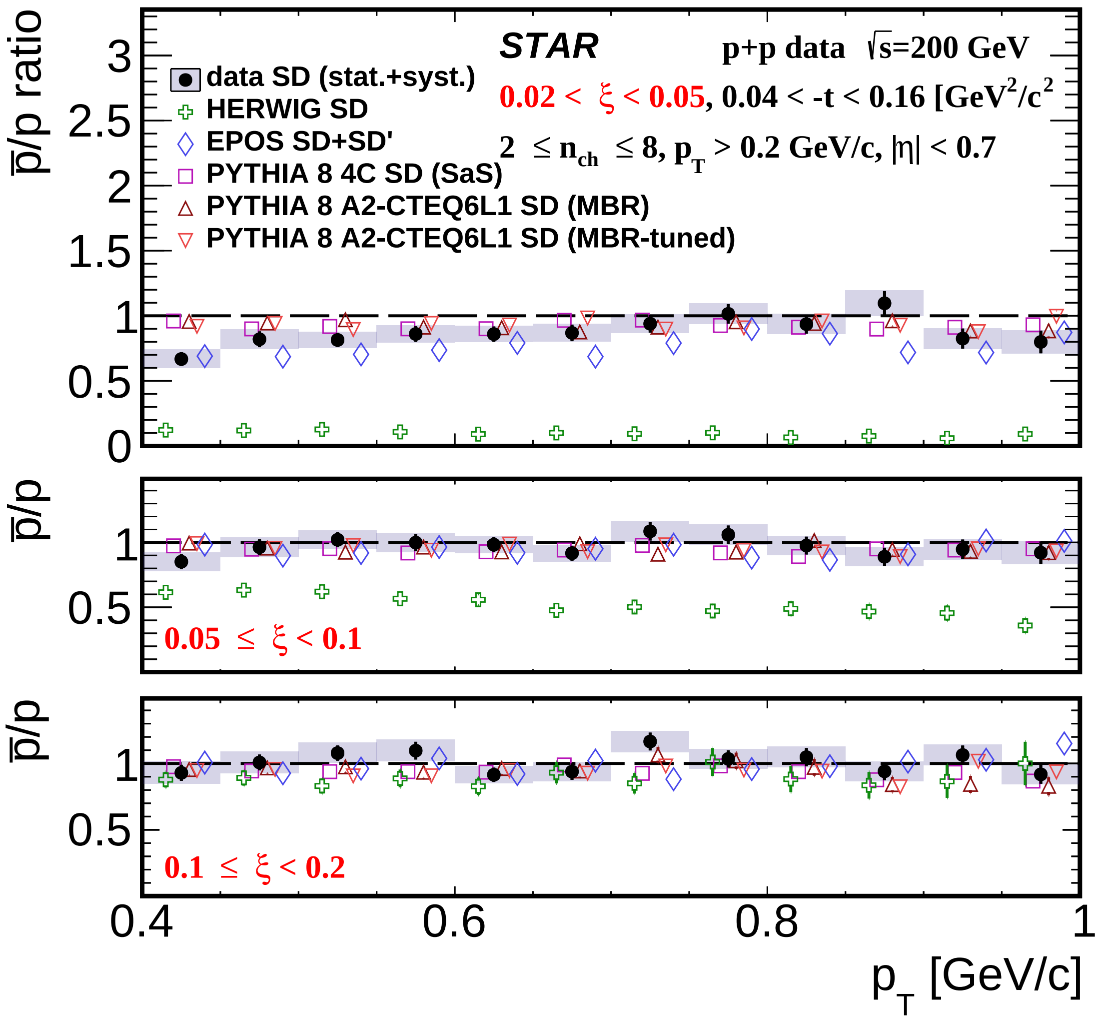

Figure 9.6: Ratio of production yields of $\bar{p}/p$ as a function of p_{T} shown separately for the three ranges of ξ: (top) $0.02 < \xi < 0.05$, (middle) $0.05 < \xi < 0.1$, (bottom) $0.1 < \xi < 0.2$.

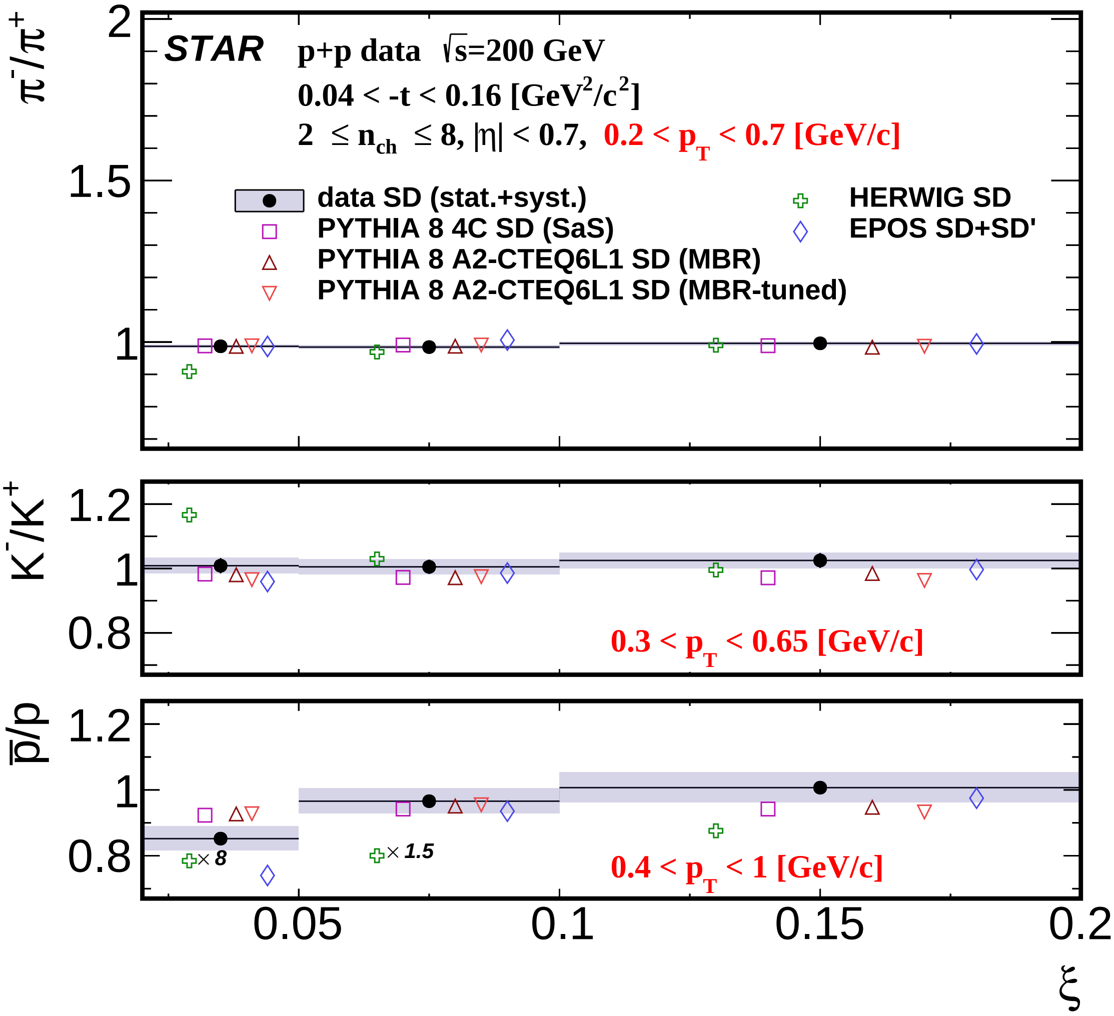

Figure 9.7: Ratio of production yields of π^-/π^+, K^-/K^+ and $\bar{p}/p$ as a function of ξ.

10. Summary and Conclusions

Inclusive and identified (pion, kaon, proton and their antiparticles) charged particle production in Single Diffractive Dissociation process has been measured in proton-proton collisions at $\sqrt{s} = 200$ GeV with the STAR detector at RHIC using data corresponding to an integrated luminosity of 15 nb^{-1}.

Significant differences are observed between the measured distributions of ξ and Monte Carlo model predictions. Amongst the models considered EPOS and PYTHIA8 (MBR) without suppression of diffractive cross sections at large ξ provide the best description of the data.

Primary-charged-particle multiplicity and its density as a function of pseudorapidity and transverse momentum are well described by PYTHIA8 and EPOS-SD$'$ models. EPOS-SD and HERWIG do not describe the data.

π^-/π^+ and K^-/K^+ production ratios are close to unity and consistent with most of model predictions except for EPOS-SD and HERWIG.

$\bar{p}/p$ production ratio shows a significant deviation from unity in the $0.02 < \xi < 0.05$ range indicating a non-negligible transfer of the baryon number from the forward to the central region. Equal amount of protons and antiprotons are observed in the $\xi > 0.05$ range. PYTHIA8 and EPOS-SD$'$ agree with data for $\xi > 0.05$. For $0.02 < \xi < 0.05$ they predict small deviations from unity (0.93) which is however higher than observed in data (0.86 ± 0.02). HERWIG and EPOS-SD predict much larger baryon number transfers compared to data for $\xi < 0.1$ and show consistency with data for $\xi > 0.1$.

Bibliography

[1] L. Adamczyk, L. Fulek, and R. Sikora, *Supplementary note on diffractive analyses of 2015 proton-proton data*, `https://drupal.star.bnl.gov/STAR/starnotes/private/psn0732`, July, 2019.

[2] B. Z. Kopeliovich and B. G. Zakharov, *Novel Mechanisms of Baryon Number Flow Over Large Rapidity Gap*, Z. Phys. **C43** (1989) 241.

[3] F. W. Bopp, *Baryon transport in dual models and the possibility of a backward peak in diffraction*, in *New trends in high-energy physics: Experiment, phenomenology, theory. Proceedings, International School-Conference, Crimea 2000, Yalta, Ukraine, May 27-June 4, 2000*. `arXiv:hep-ph/0007229 [hep-ph]`.

[4] M. Anderson et al., *The STAR Time Projection Chamber: A Unique tool for studying high multiplicity events at RHIC*, Nucl. Instrum. Meth. **A499** (2003) 659–678.

[5] R. Brun, F. Bruyant, M. Maire, A. C. McPherson, and P. Zanarini, *GEANT3*, CERN-DD-EE-84-1 (1987).

[6] GEANT4 Collaboration, S. Agostinelli et al., *GEANT4: A Simulation toolkit*, Nucl. Instrum. Meth. **A506** (2003) 250–303.

[7] W. Fischer, *Run Overview of the Relativistic Heavy Ion Collider*, `http://www.agsrhichome.bnl.gov/RHIC/Runs/`.

[8] STAR Collaboration, B. I. Abelev et al., *Systematic Measurements of Identified Particle Spectra in pp, d^+ Au and Au+Au Collisions from STAR*, Phys. Rev. **C79** (2009) 034909, `arXiv:0808.2041 [nucl-ex]`.

[9] ATLAS Collaboration, G. Aad et al., *Charged-particle distributions in $\sqrt{s}$ = 13 TeV pp interactions measured with the ATLAS detector at the LHC*, Phys. Lett. **B758** (2016) 67–88.

[10] G. D'Agostini, *A Multidimensional unfolding method based on Bayes' theorem*, Nucl. Instrum. Meth. **A362** (1995) 487–498.

[11] H. Bichsel, *A method to improve tracking and particle identification in TPCs and silicon detectors*, Nucl. Instrum. Meth. **A562** (2006) 154–197.

Appendices

A. Acronyms

AGS	Alternating Gradient Synchrotron
AFP	ATLAS Forward Proton
ALFA	Absolute Luminosity For ATLAS
ATLAS	A Toroidal LHC Apparatus
BBC	Beam Beam Counter
BCID	Bunch Crossing Identifier
BEMC	Barrel Electromagnetic Calorimeter
BNL	Brookhaven National Laboratory
CD	Central Diffraction
CEP	Central Exclusive Production
CERN	European Laboratory for Particle Physics
CR	Colour Reconnection
DAQ	Data Acquisition System
DD	Double Diffraction
DIS	Deep Inelastic Scattering
DL	Donnachie and Landshoff
DPDFs	Diffractive Parton Distribution Functions
EBIS	Electron Beam Ion Source
FCAL	Forward Calorimeters
FSR	Final State Radiation
HCAL	Hadronic Calorimeter
HEC	Hadronic End-Cap
ECR	Electron Cyclotron Resonance
EM	Electromagnetic
HFT	Heavy Flavor Tracker
HLT	High Level Trigger
IBL	Insertable B-Layer
ID	Inner Detector
IP	Interaction Point
ISR	Initial State Radiation
L1	Level-1

LAr	liquid argon
LEIR	Low-Energy Ion Ring
LEP	Large Electron Positron Collider
LHC	Large Hadron Collider
LION	Laser Ion Source
MAPMT	Multi Anode Photomultiplier Tube
MB	Minimum Bias
MBR	Minimum Bias Rockefeller
MBTS	Minimum Bias Trigger Scintillator
MPV	Most Probable Value
MC	Monte Carlo
MD	Main Detector
MPI	Multiple Parton Interactions
MRPC	Multi-gap Resistive Plate Chambers
MWPC	Multi Wire Proportional Chambers
ND	Non-Diffractive
OD	Overlap Detector
OPPIS	Optically Pumped Polarized Ion Source
PDFs	Parton Distribution Functions
PP0	Patch Panel 0
PP	Patch Panel
PS	Proton Synchrotron
PSB	Proton Synchrotron Booster
QCD	Quantum Chromodynamics
QED	Quantum Electrodynamics
QGP	Quark Gluon Plasma
QFT	Quantum Field Theory
RFQ	Radio Frequency Quadrupole
RHIC	Relativistic Heavy Ion Collider
ROI	Regions-of-Interest
RP	Roman Pot
SaS	Schuler and Sjöstrand
SCT	Semiconductor Tracker

SD	Single Diffraction
SM	Standard Model
SMD	Shower Maximum Detector
SPS	Super Proton Synchrotron
SSD	Silicon Strip Detectors
STAR	Solenoidal Tracker at RHIC
TDAQ	Trigger and Data Acquisition
TOF	Time of Flight
TPC	Time Projection Chamber
TRT	Transition Radiation Tracker
UE	Underlying Events
VPD	Vertex Position Detector
ZDC	Zero Degree Calorimeter

B. Proton and Antiproton DCA Distributions

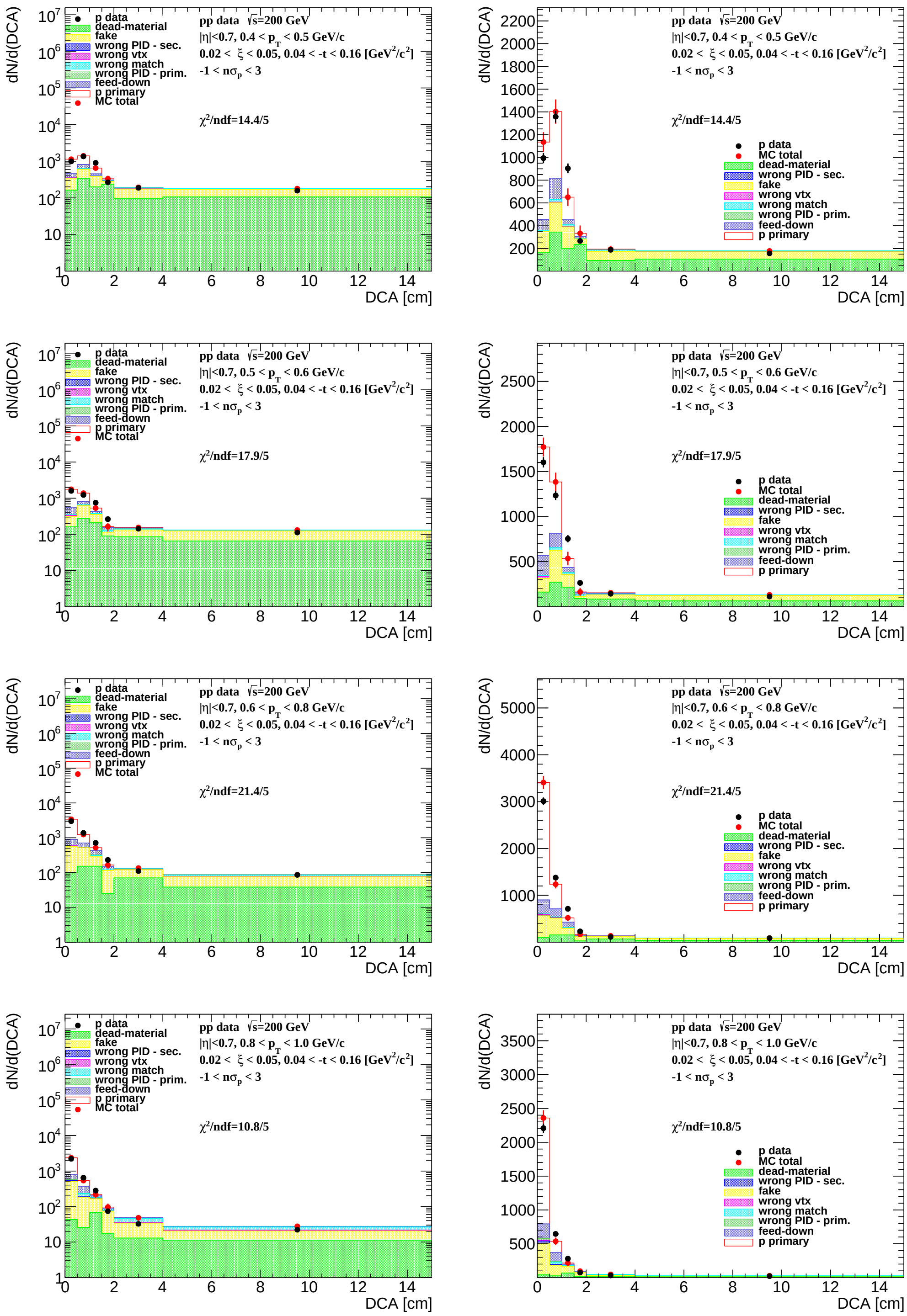

Figure B.1: Distributions of DCA for protons in SD interactions with $0.02 < \xi < 0.05$ and loose selection.

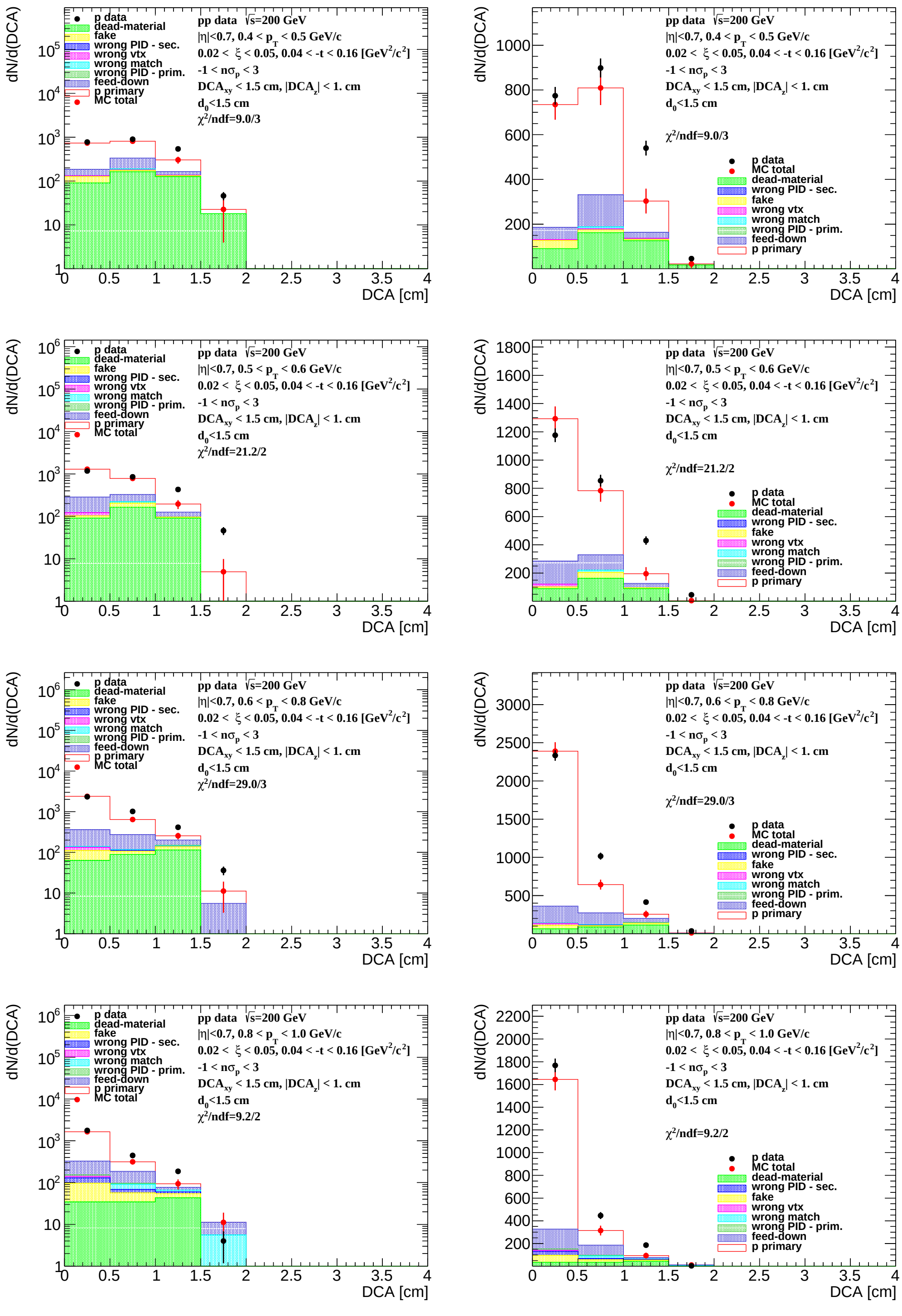

Figure B.2: Distributions of DCA for protons in SD interactions with $0.02 < \xi < 0.05$ and normal selection.

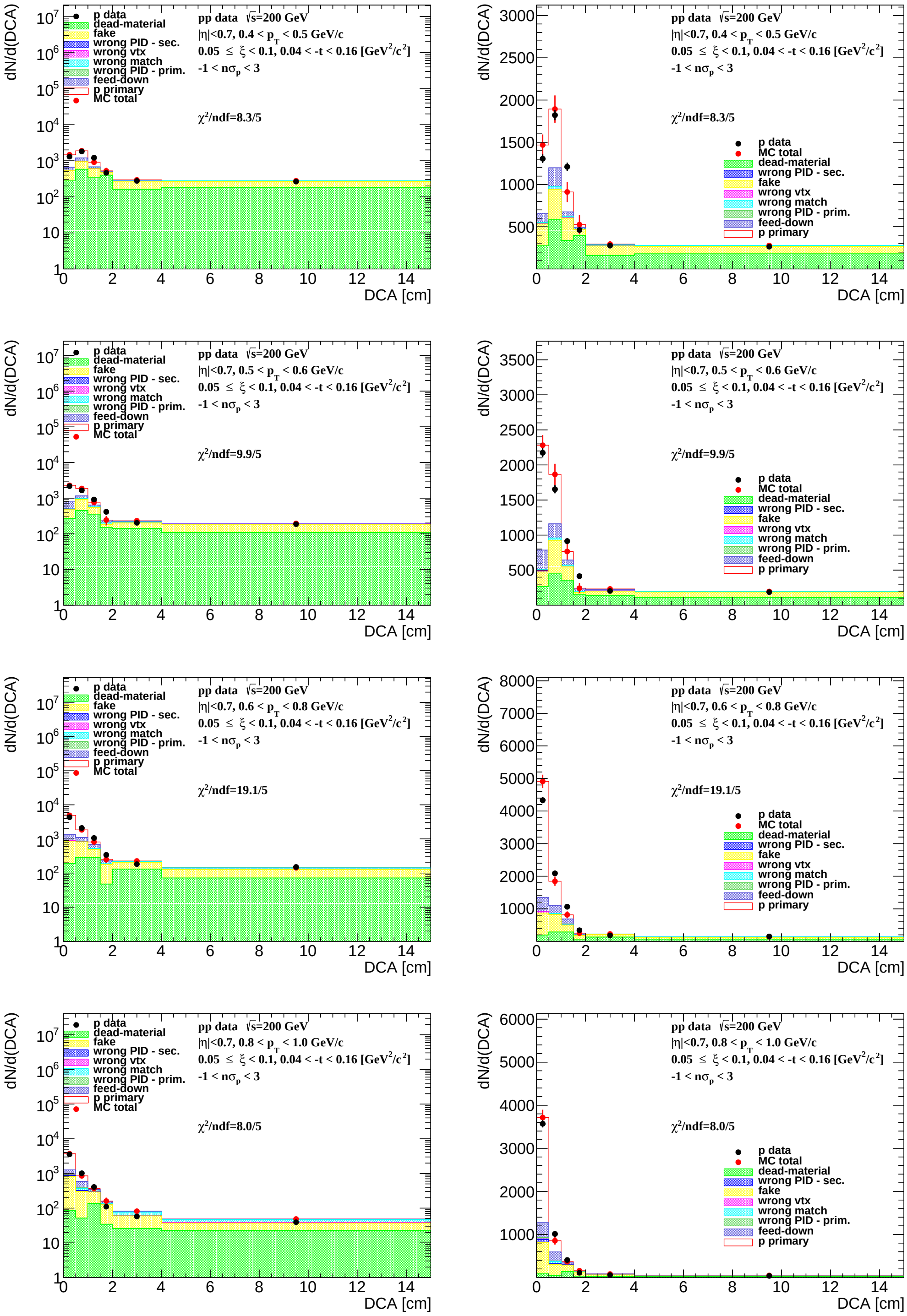

Figure B.3: Distributions of DCA for protons in SD interactions with $0.05 < \xi < 0.1$ and loose selection.

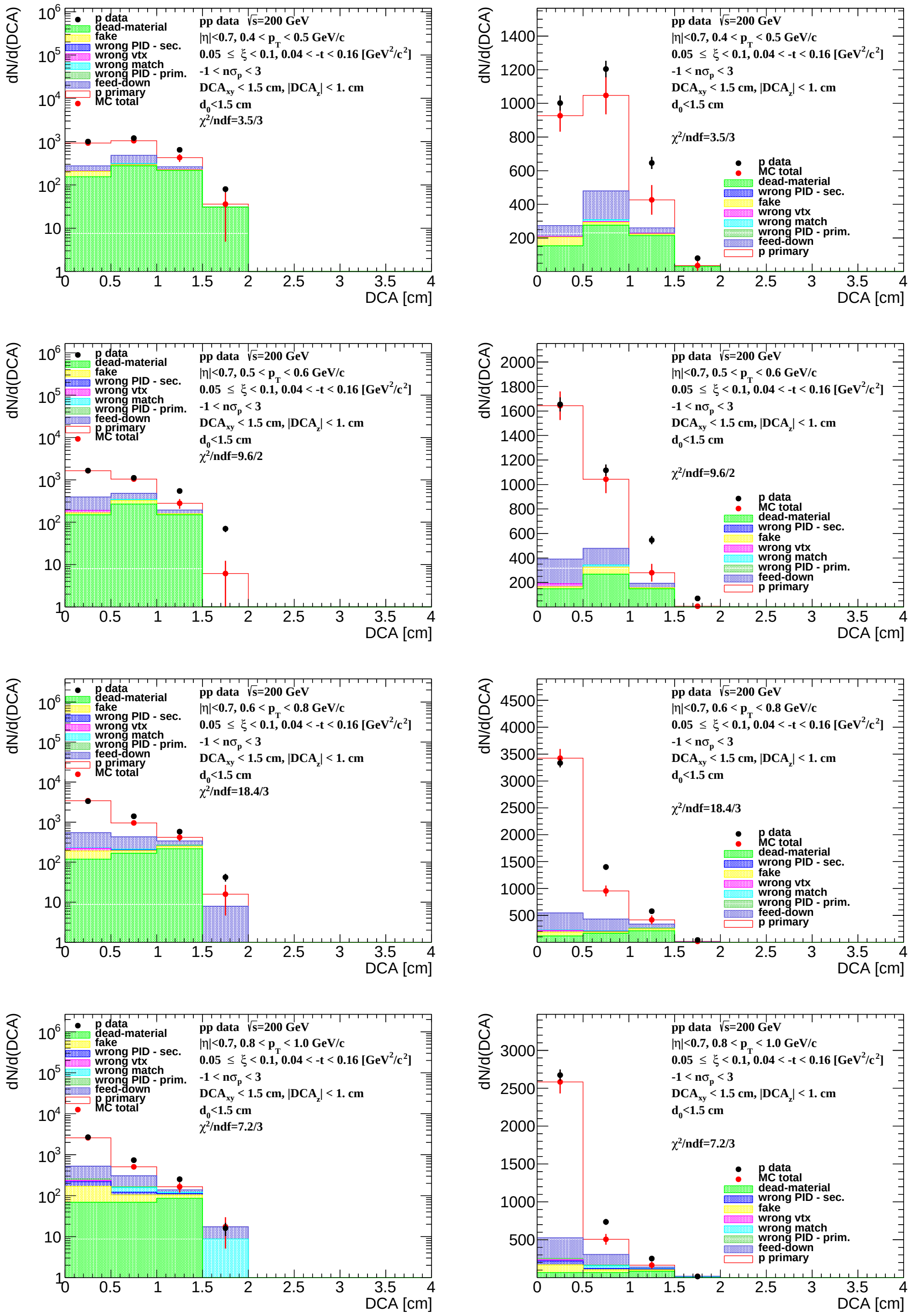

Figure B.4: Distributions of DCA for protons in SD interactions with $0.05 < \xi < 0.1$ and normal selection.

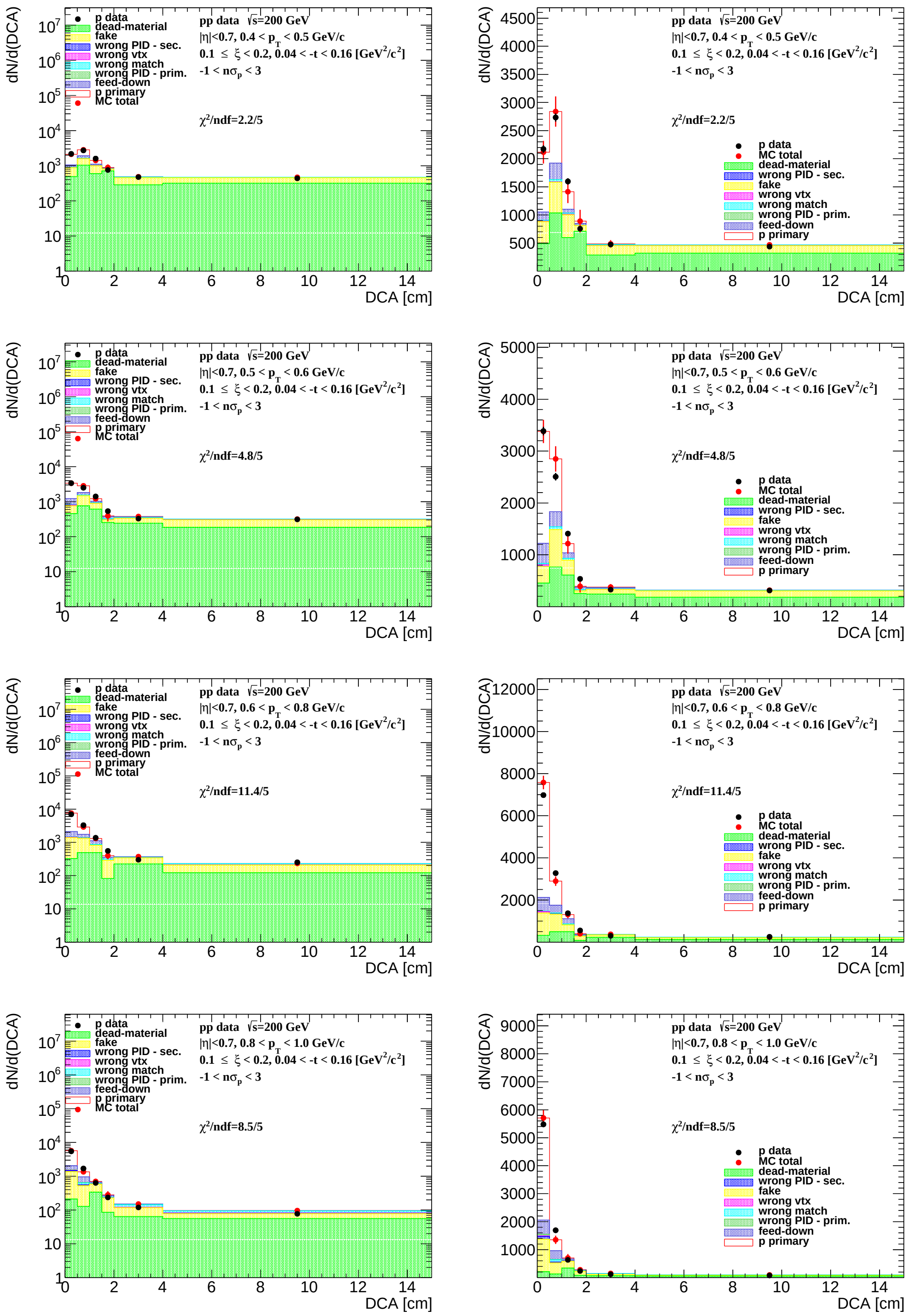

Figure B.5: Distributions of DCA for protons in SD interactions with $0.1 < \xi < 0.2$ and loose selection.

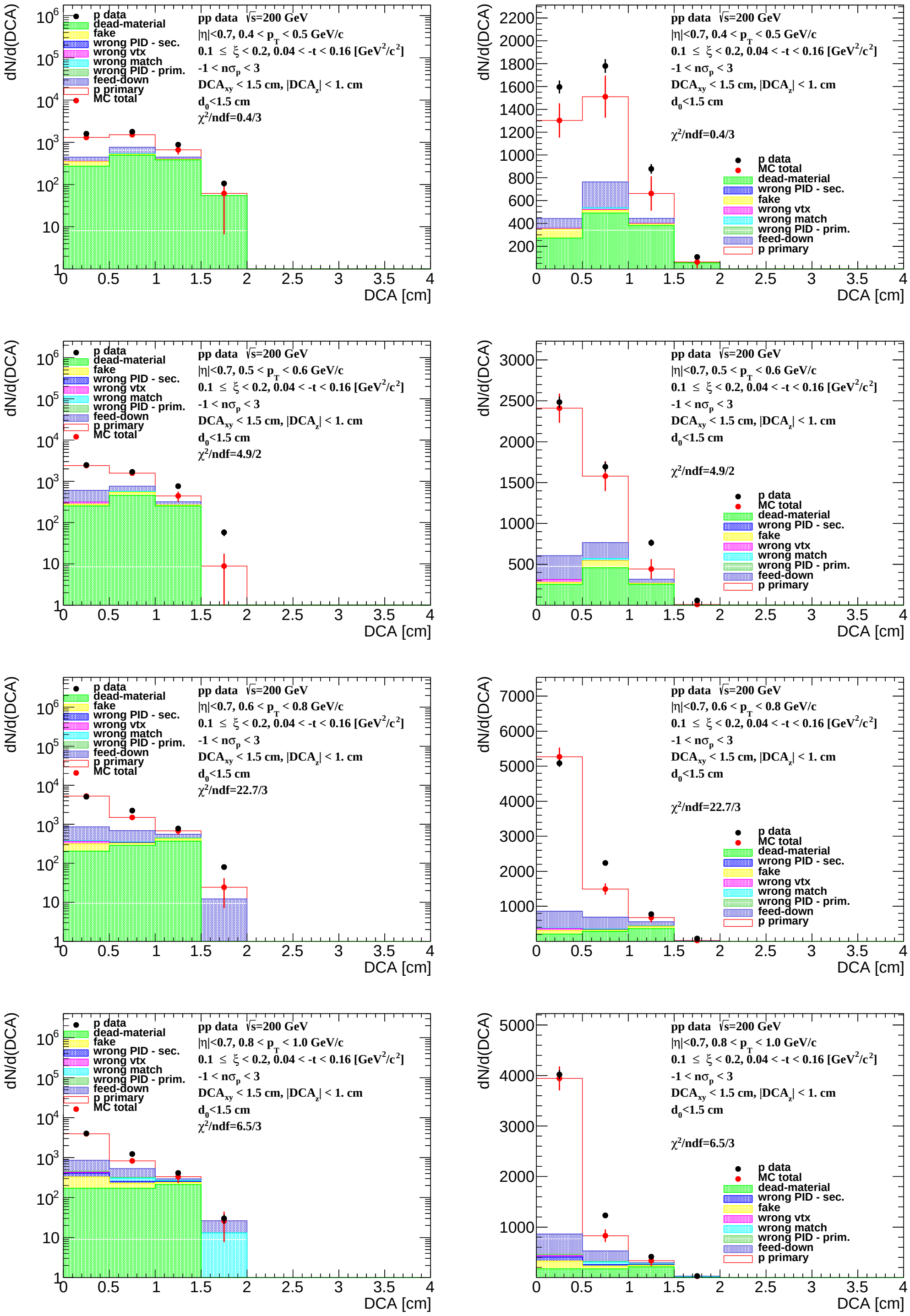

Figure B.6: Distributions of DCA for protons in SD interactions with $0.1 < \xi < 0.2$ and normal selection.

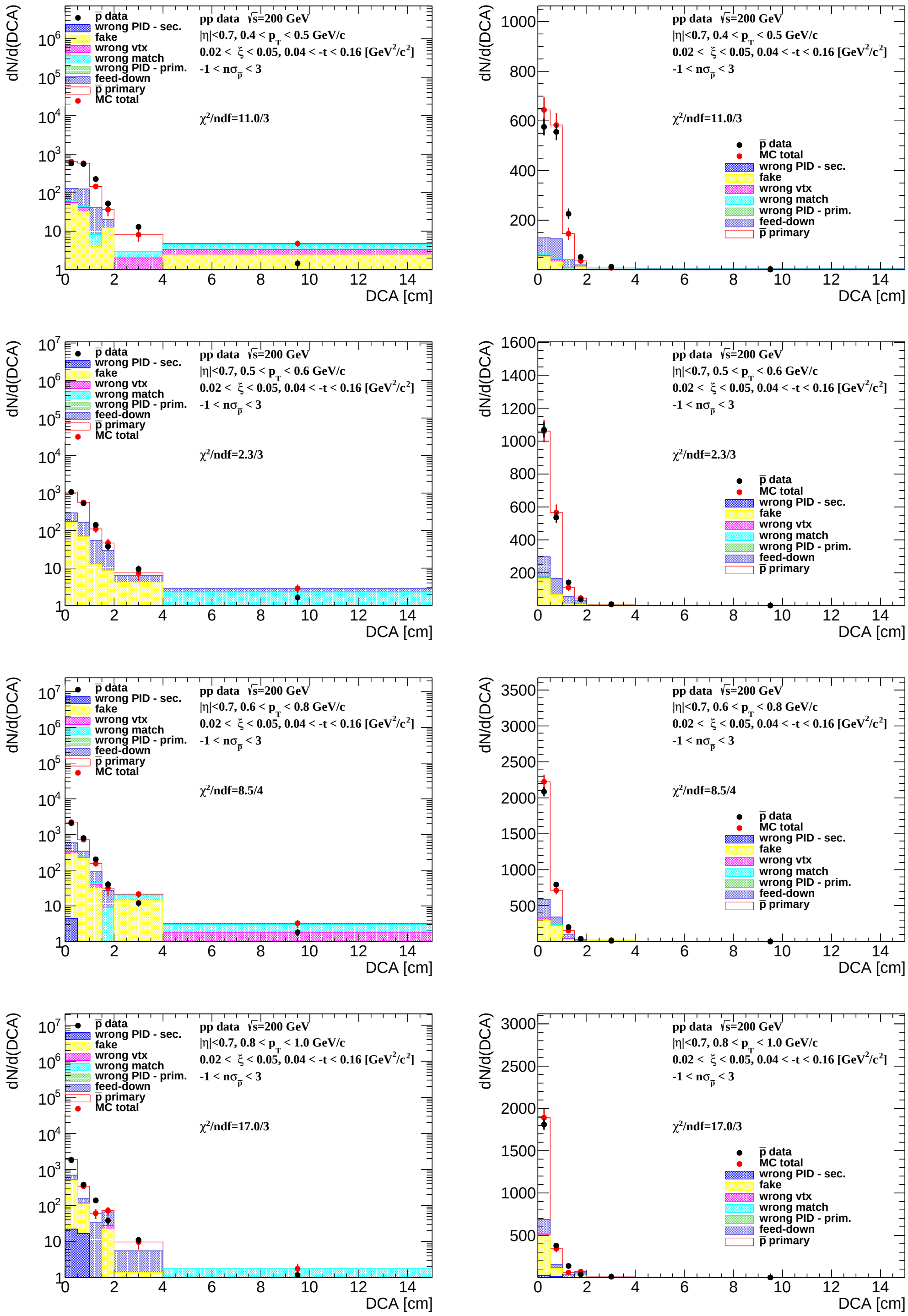

Figure B.7: Distributions of DCA for antiprotons in SD interactions with $0.02 < \xi < 0.05$ and loose selection.

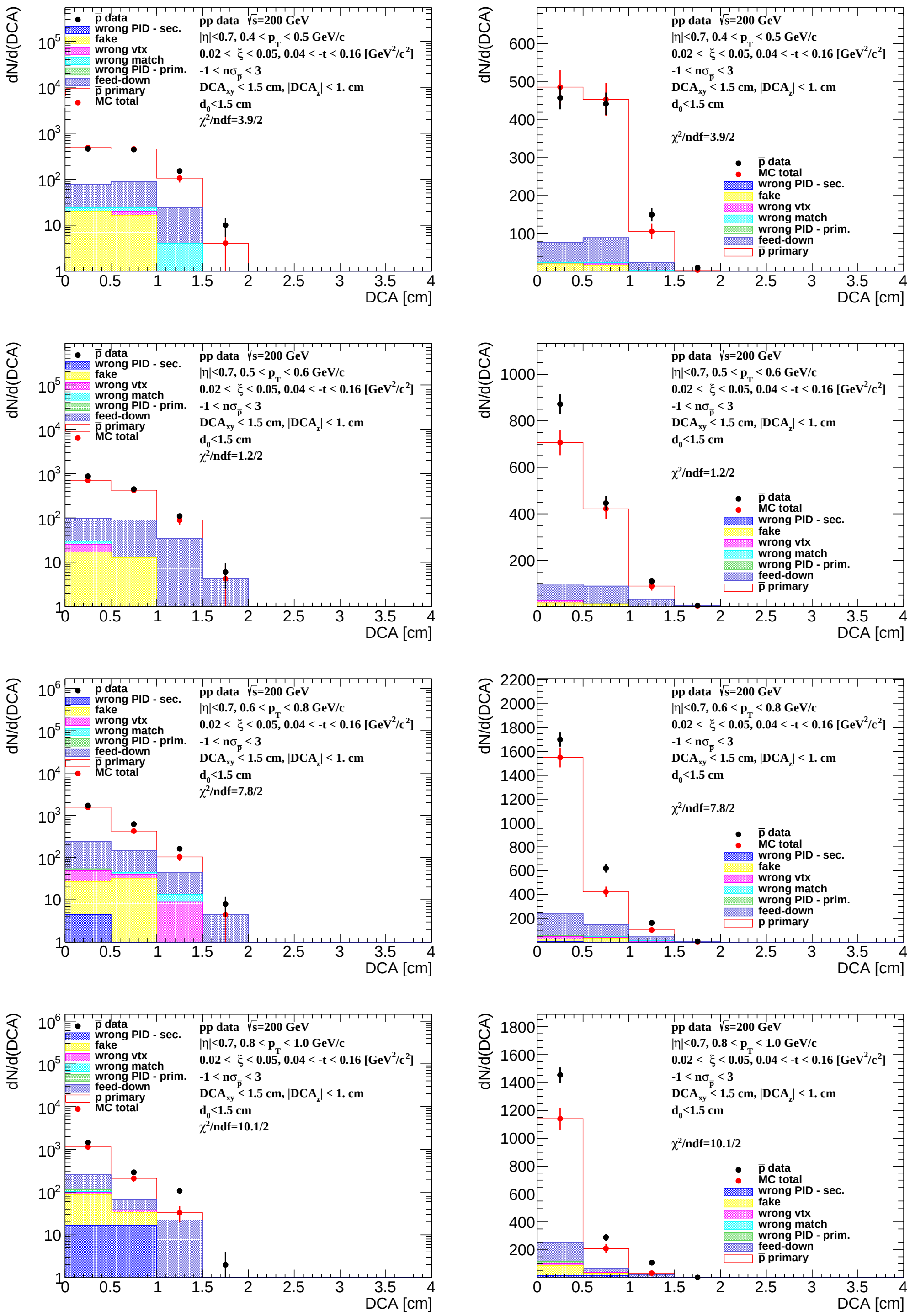

Figure B.8: Distributions of DCA for antiprotons in SD interactions with $0.02 < \xi < 0.05$ and normal selection.

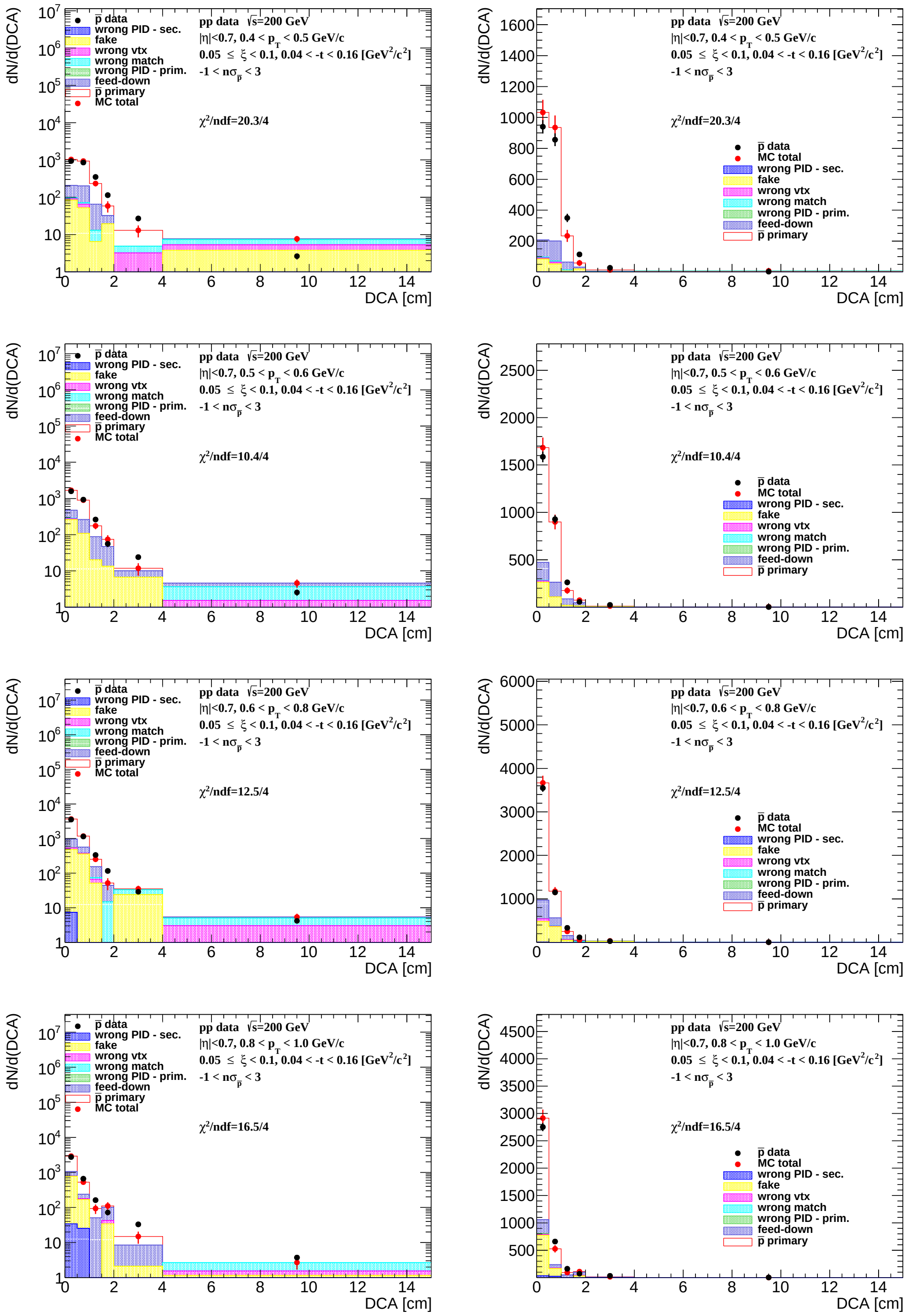

Figure B.9: Distributions of DCA for antiprotons in SD interactions with $0.05 < \xi < 0.1$ and loose selection.

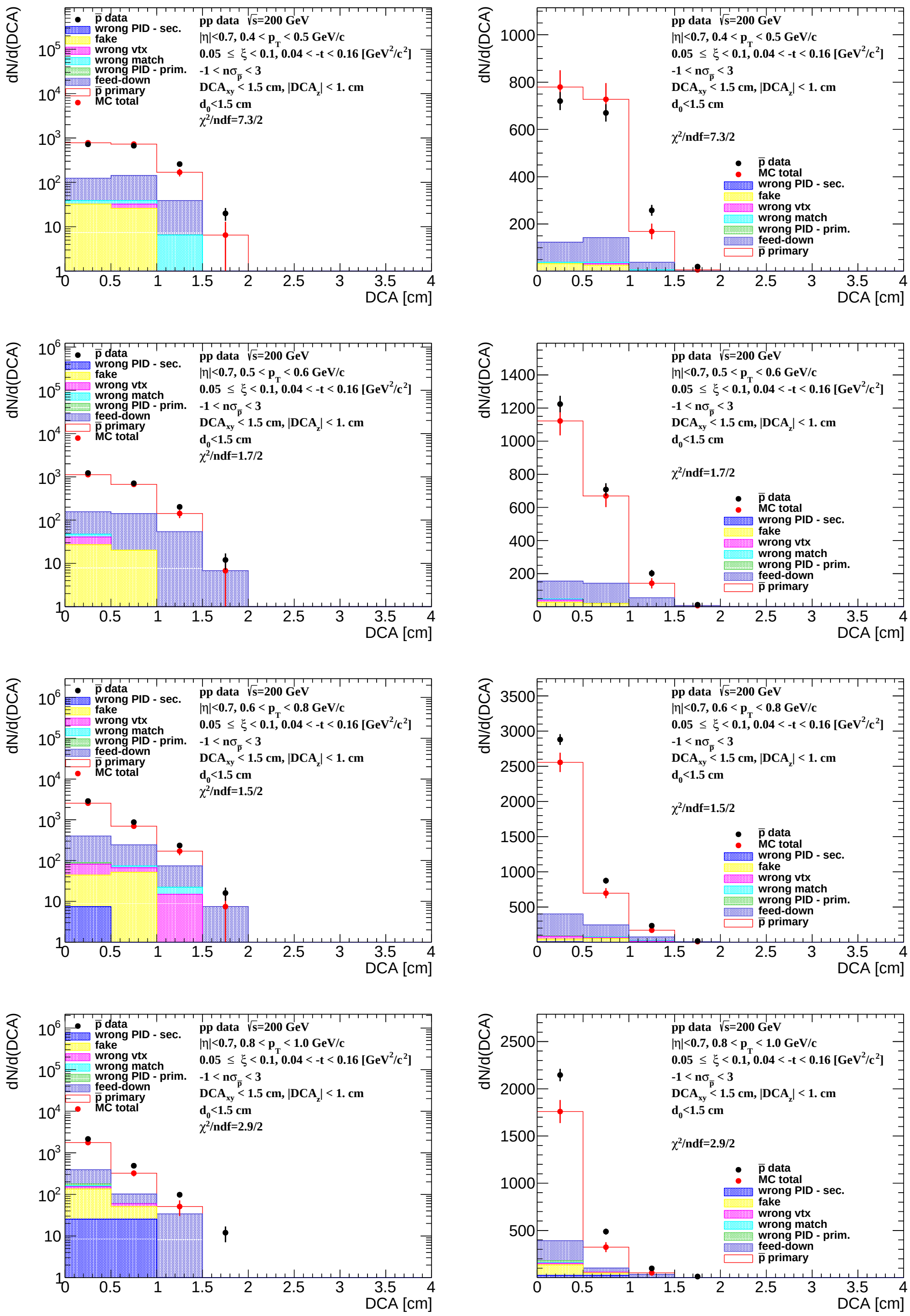

Figure B.10: Distributions of DCA for antiprotons in SD interactions with $0.05 < \xi < 0.1$ and normal selection.

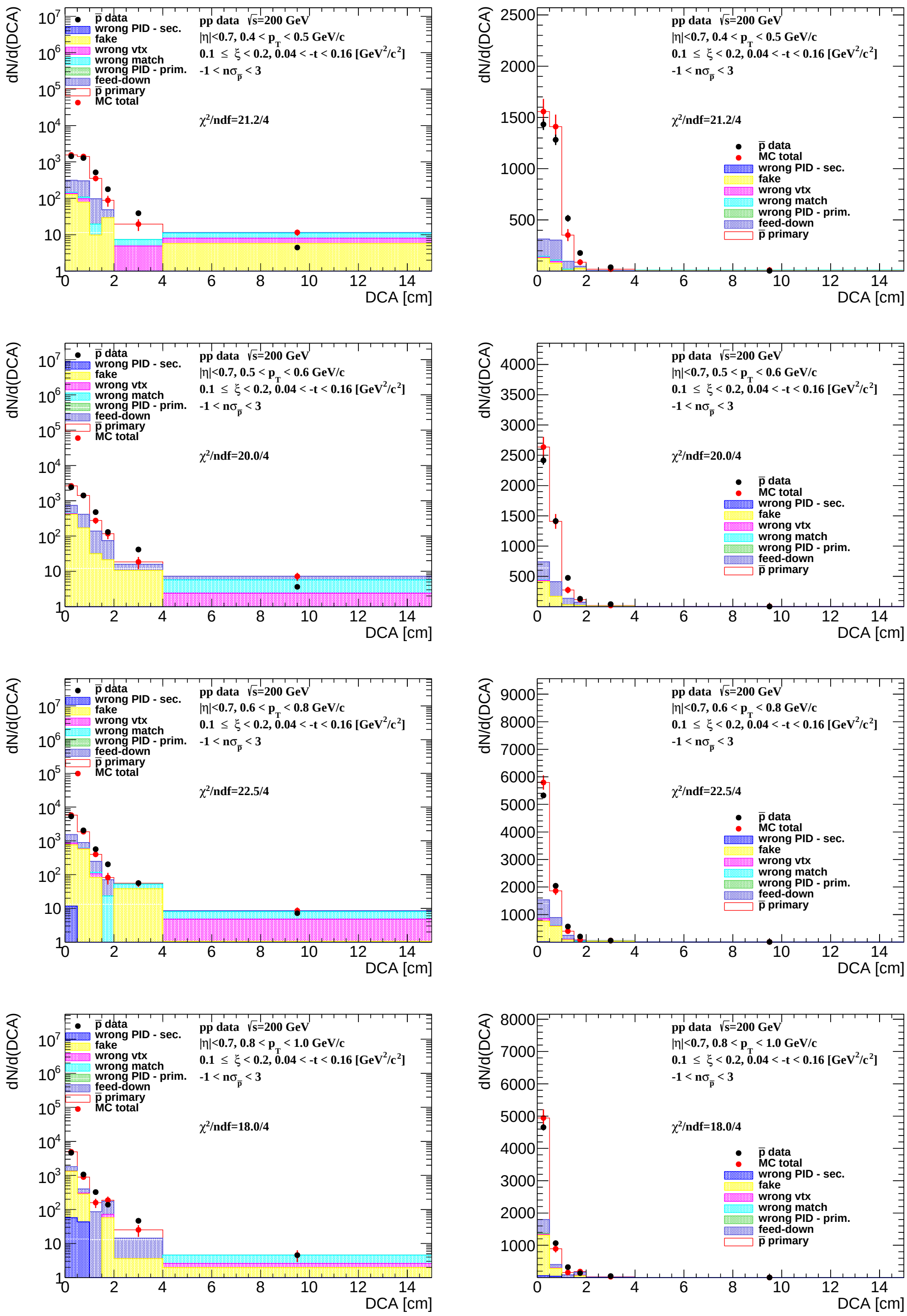

Figure B.11: Distributions of DCA for antiprotons in SD interactions with $0.1 < \xi < 0.2$ and loose selection.

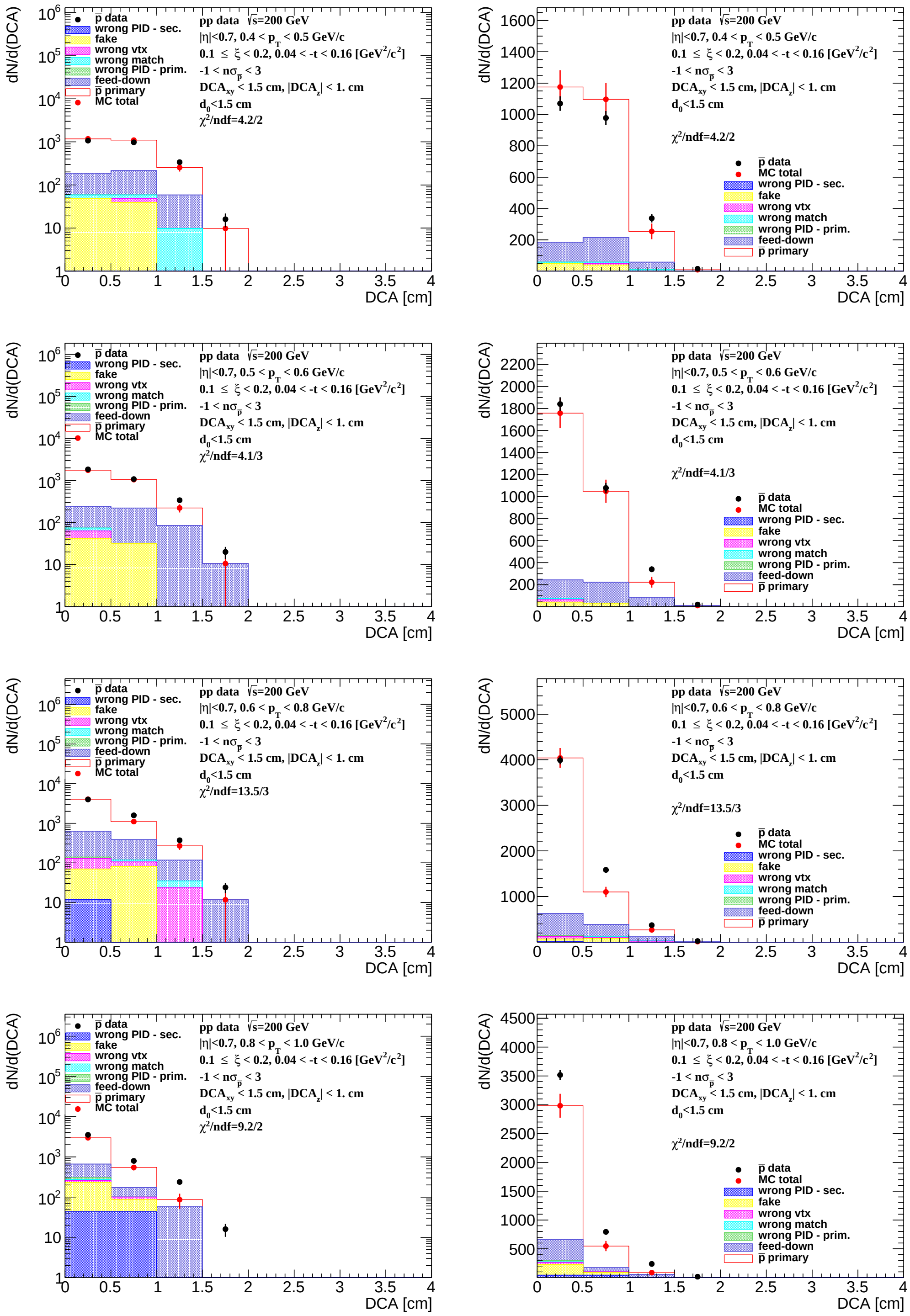

Figure B.12: Distributions of DCA for antiprotons in SD interactions with $0.1 < \xi < 0.2$ and normal selection.

C. Distributions of $n\sigma^{i}_{dE/dx}$ in SD

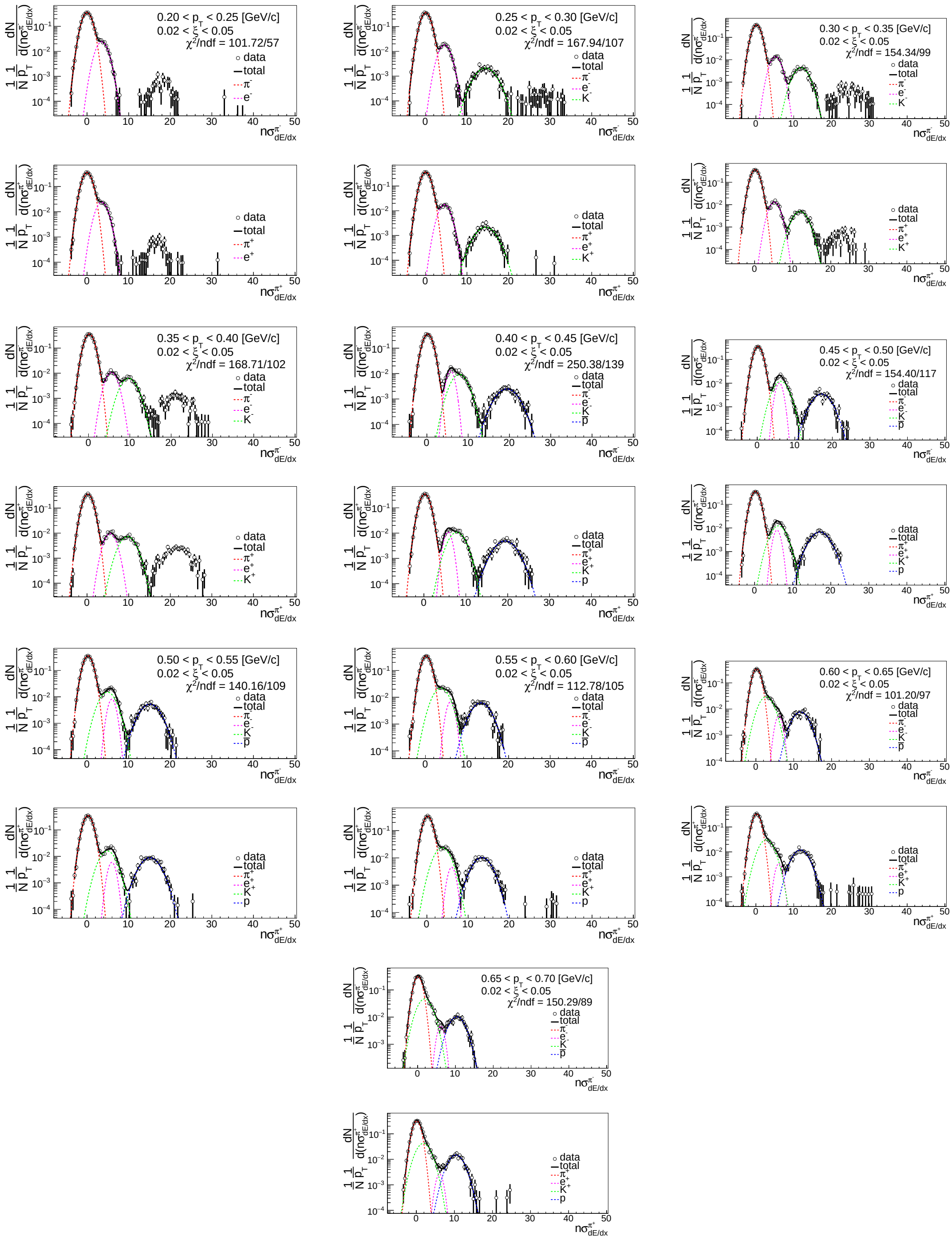

Figure C.1: Distributions of $n\sigma^{\pi^{\pm}}_{dE/dx}$ for $\pi^{\pm}$ in SD interactions with $0.02 < \xi < 0.05$.

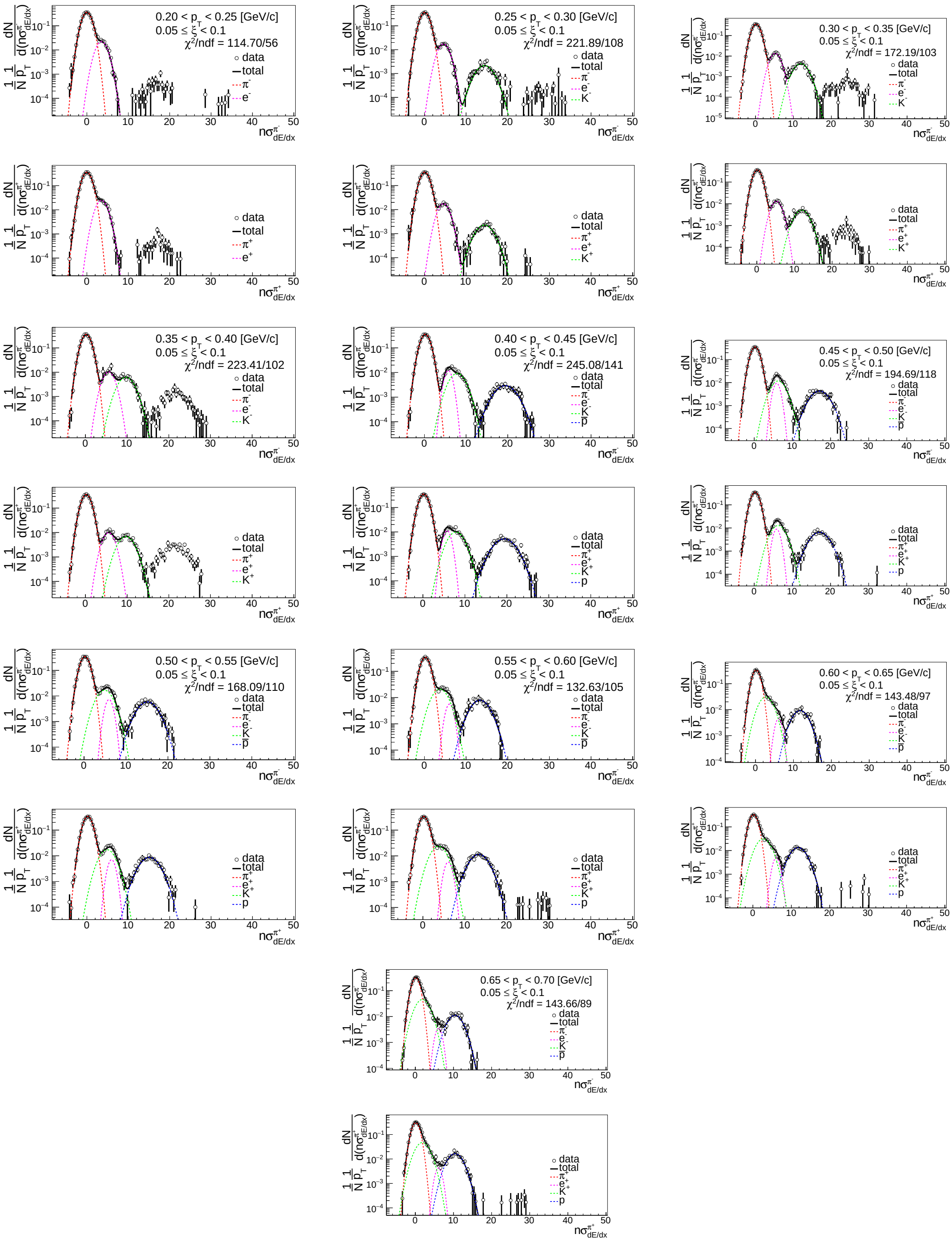

Figure C.2: Distributions of $n\sigma^{\pi^\pm}_{dE/dx}$ for $\pi^\pm$ in SD interactions with $0.05 < \xi < 0.1$.

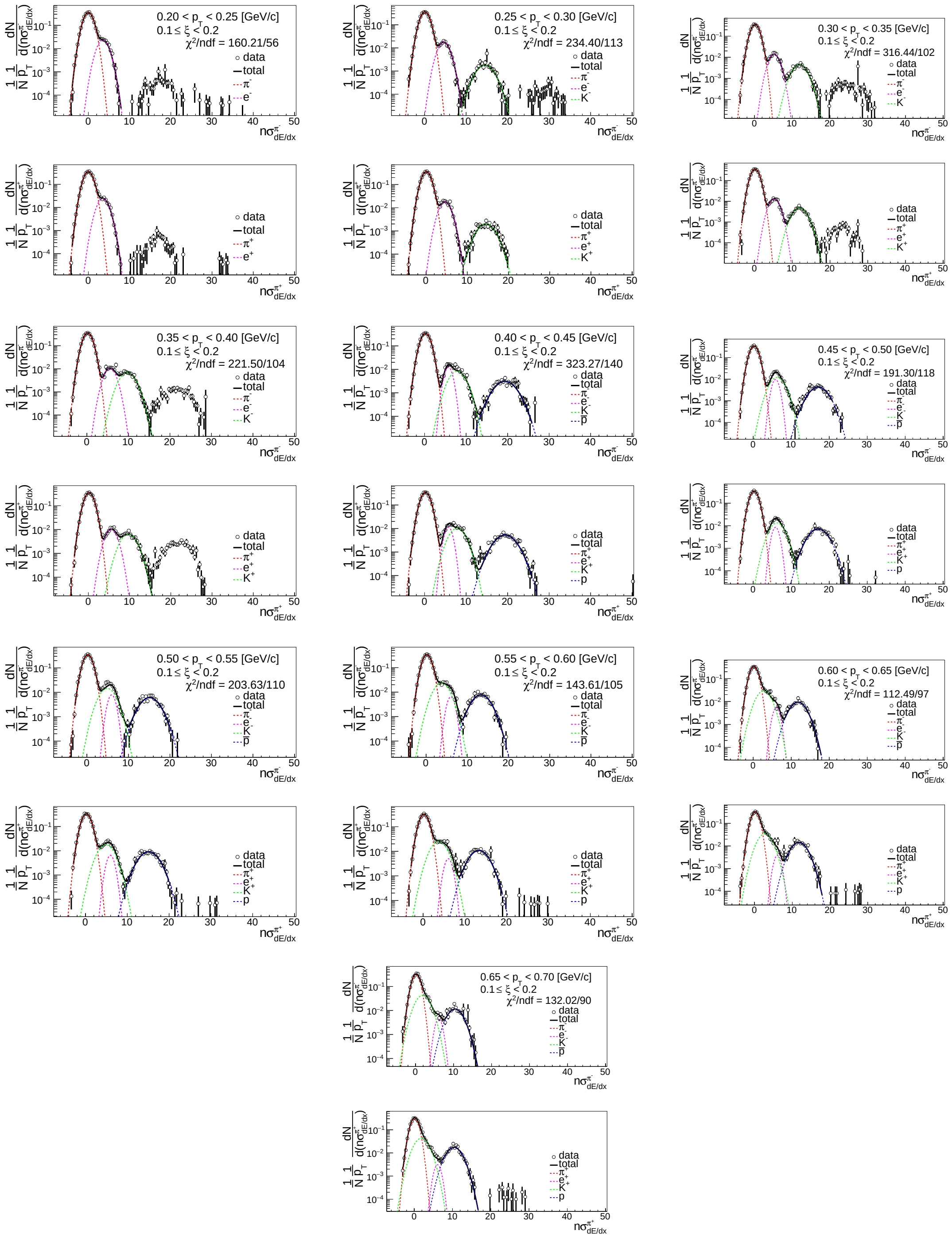

Figure C.3: Distributions of $n\sigma^{\pi^{\pm}}_{dE/dx}$ for $\pi^{\pm}$ in SD interactions with $0.1 < \xi < 0.2$.

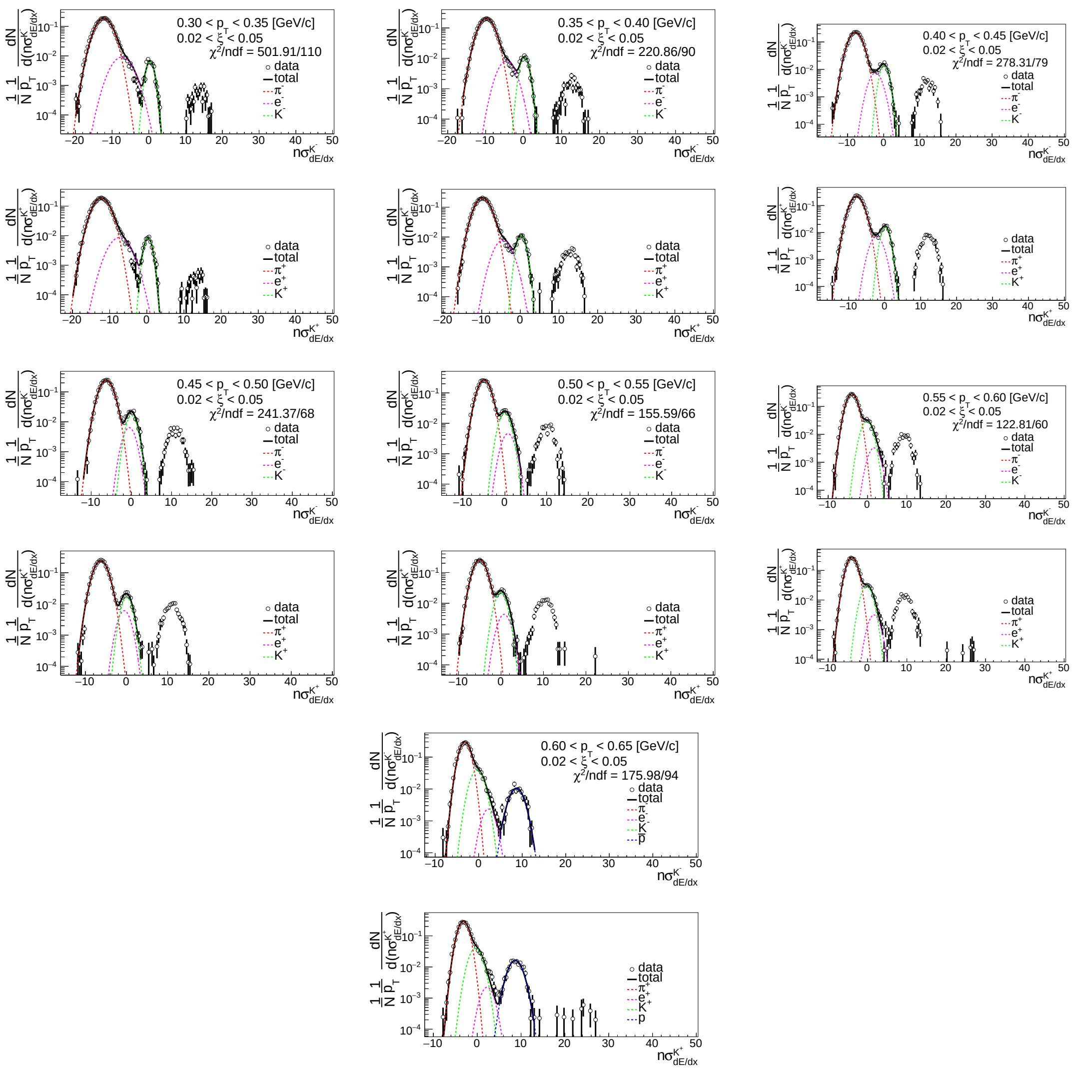

Figure C.4: Distributions of $n\sigma^{K^{\pm}}_{dE/dx}$ for $K^{\pm}$ in SD interactions with $0.02 < \xi < 0.05$.

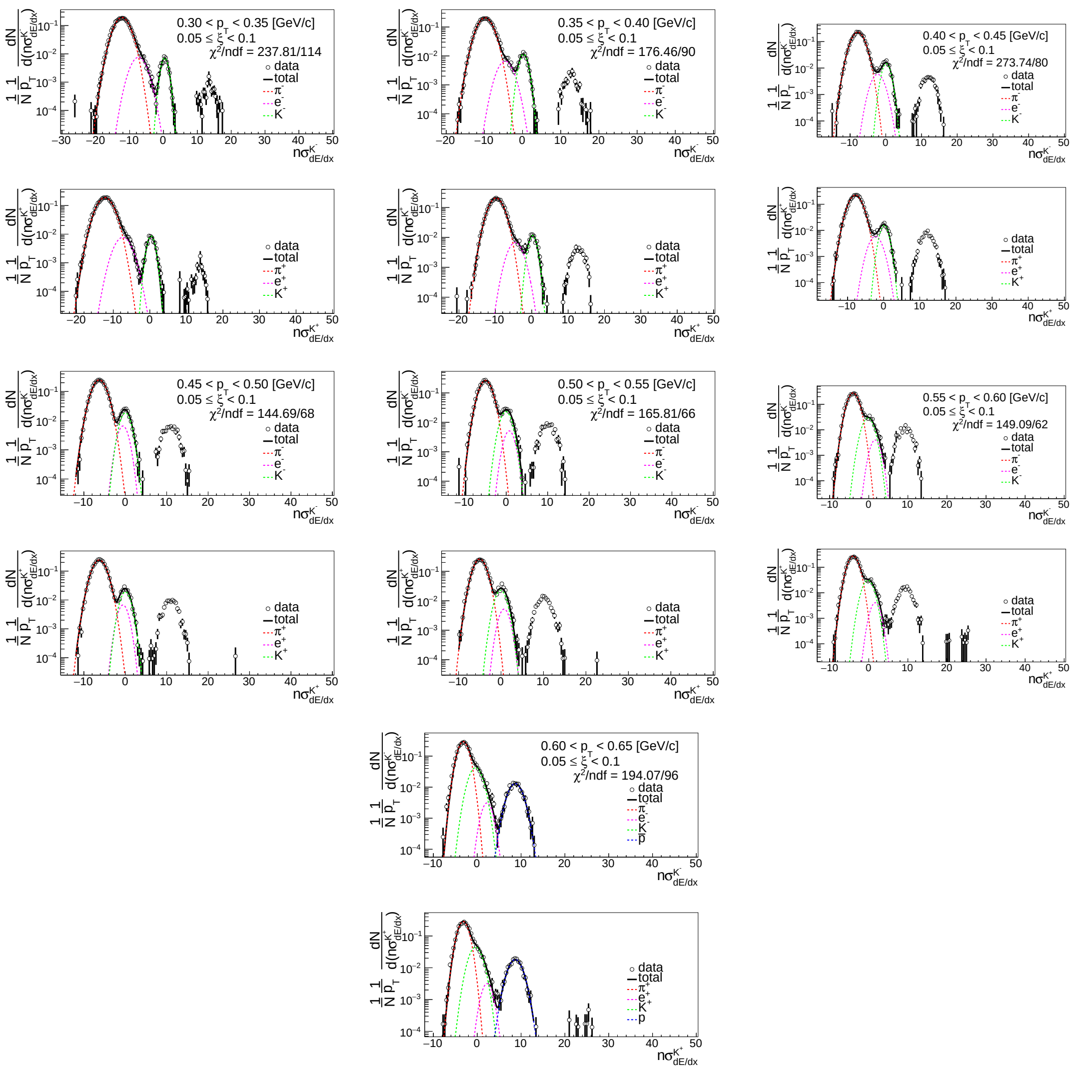

Figure C.5: Distributions of $n\sigma^{K^{\pm}}_{dE/dx}$ for $K^{\pm}$ in SD interactions with $0.05 < \xi < 0.1$.

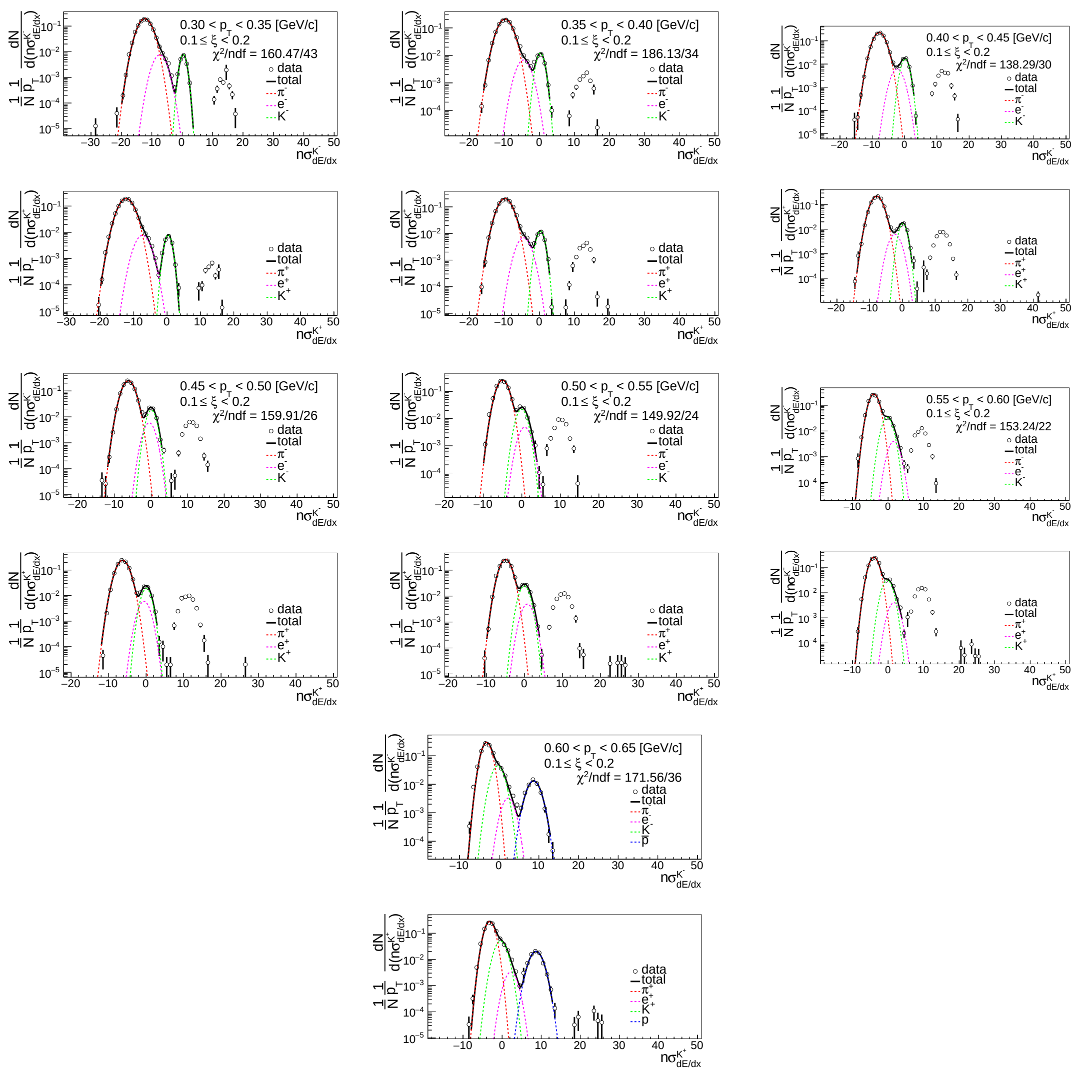

Figure C.6: Distributions of $n\sigma^{K^{\pm}}_{dE/dx}$ for $K^{\pm}$ in SD interactions with $0.1 < \xi < 0.2$.

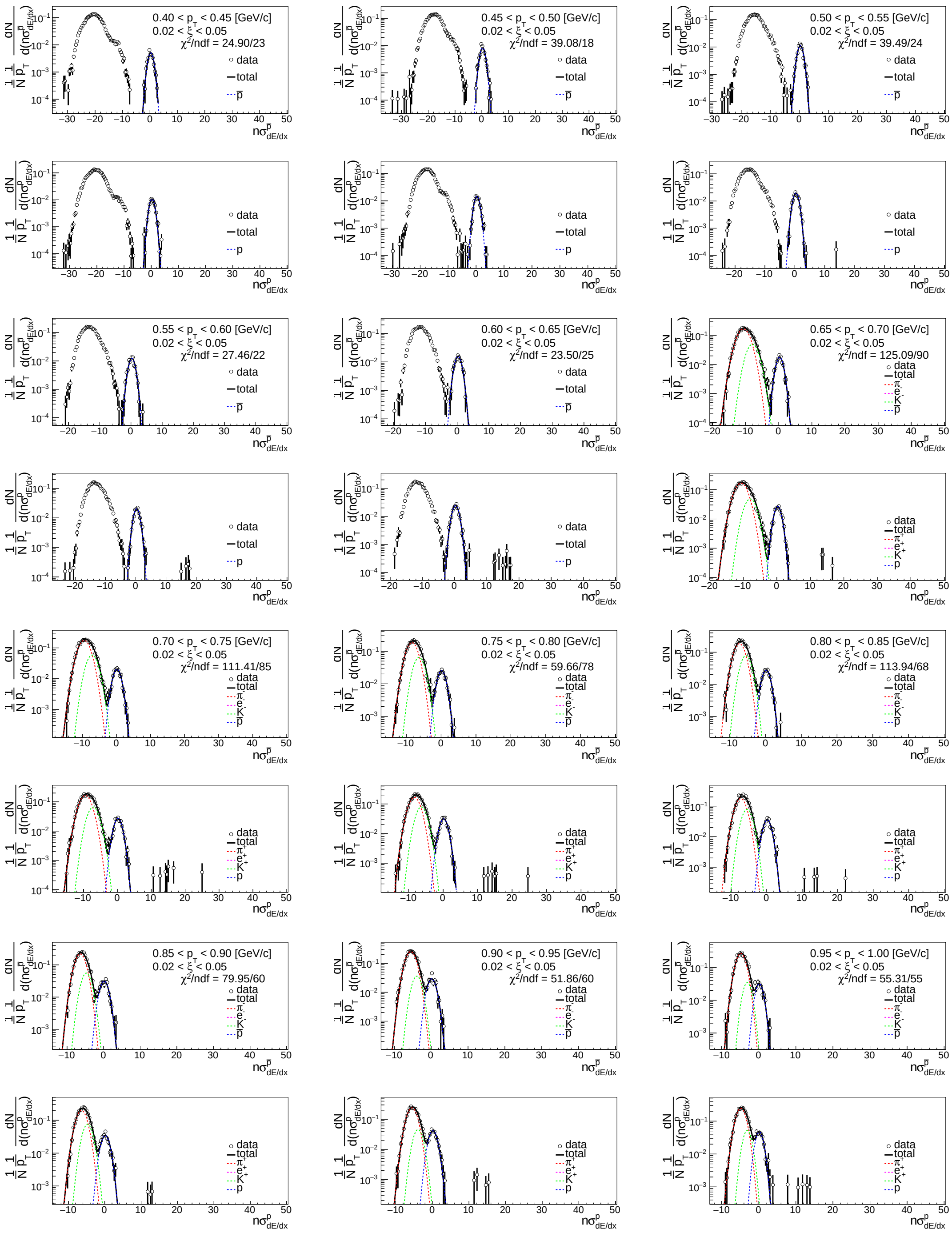

Figure C.7: Distributions of $n\sigma^{\bar{p},p}_{dE/dx}$ for $\bar{p}, p$ in SD interactions with $0.02 < \xi < 0.05$.

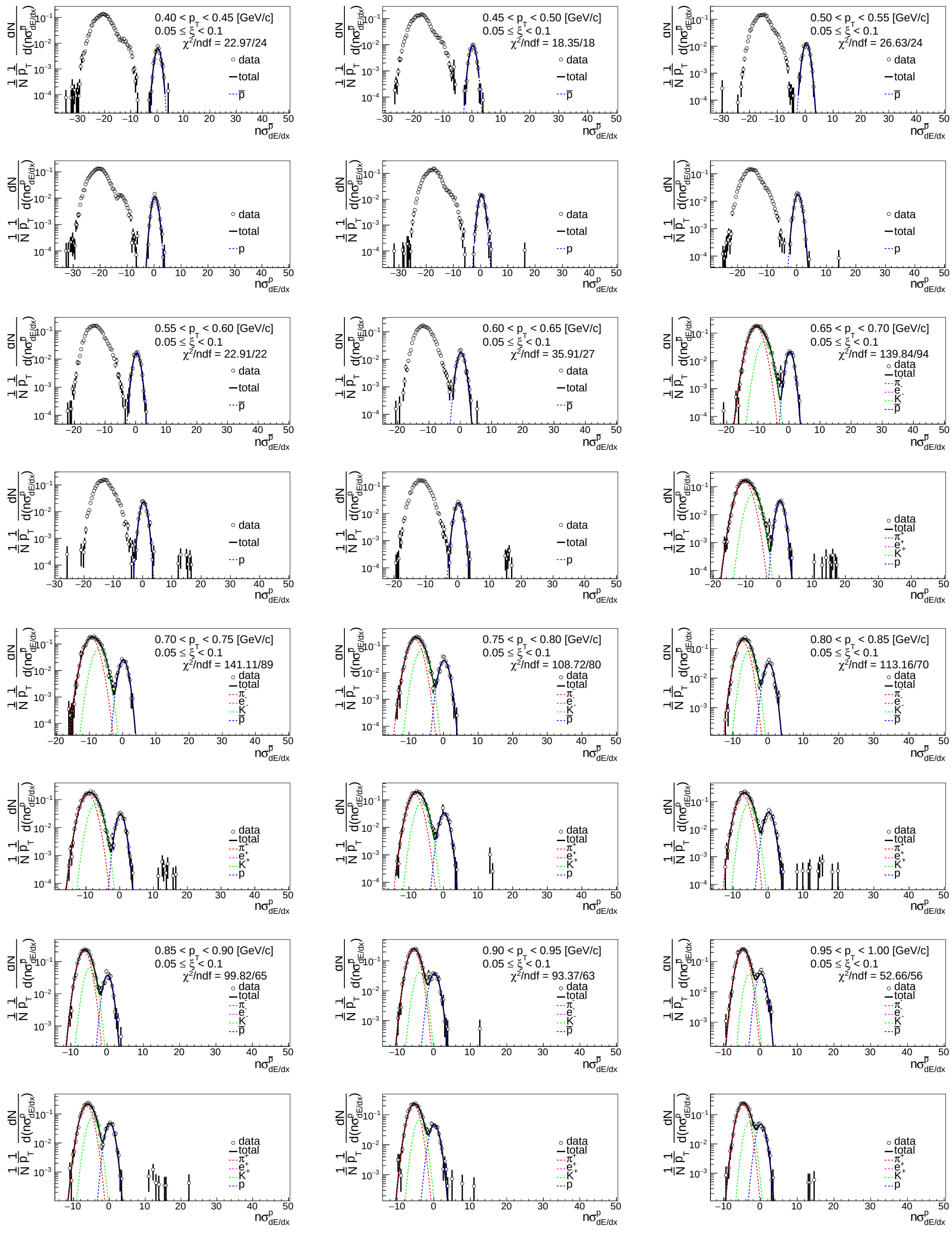

Figure C.8: Distributions of $n\sigma_{dE/dx}^{\bar{p},p}$ for $\bar{p}, p$ in SD interactions with $0.05 < \xi < 0.1$.

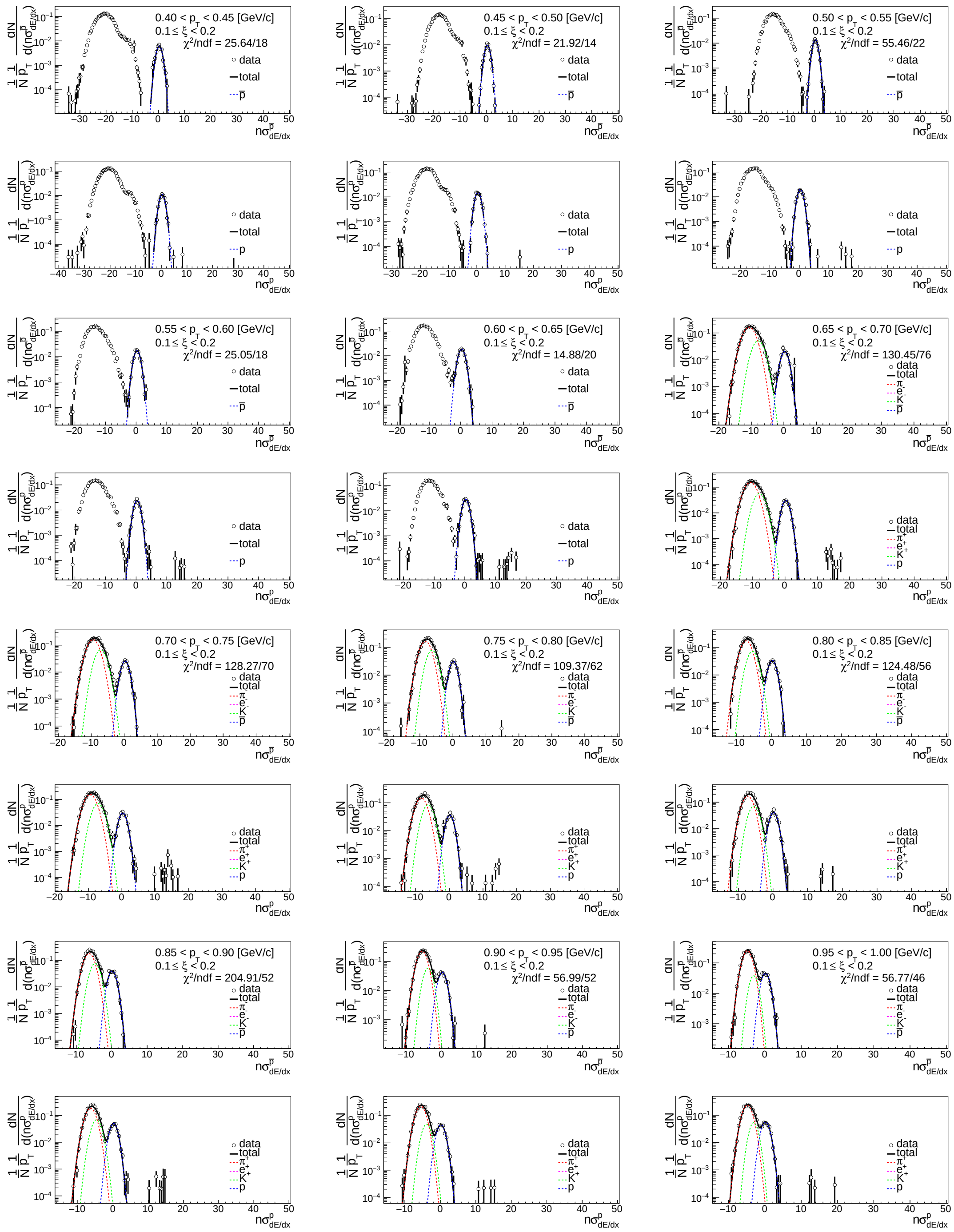

Figure C.9: Distributions of $n\sigma^{\bar{p},p}_{dE/dx}$ for $\bar{p}, p$ in SD interactions with $0.1 < \xi < 0.2$.